LED-stimulated Liquid Crystalline Elastomers (LCEs) as Contractile Units for Assisting Cardiac Contraction

L.F.A. Wymenga

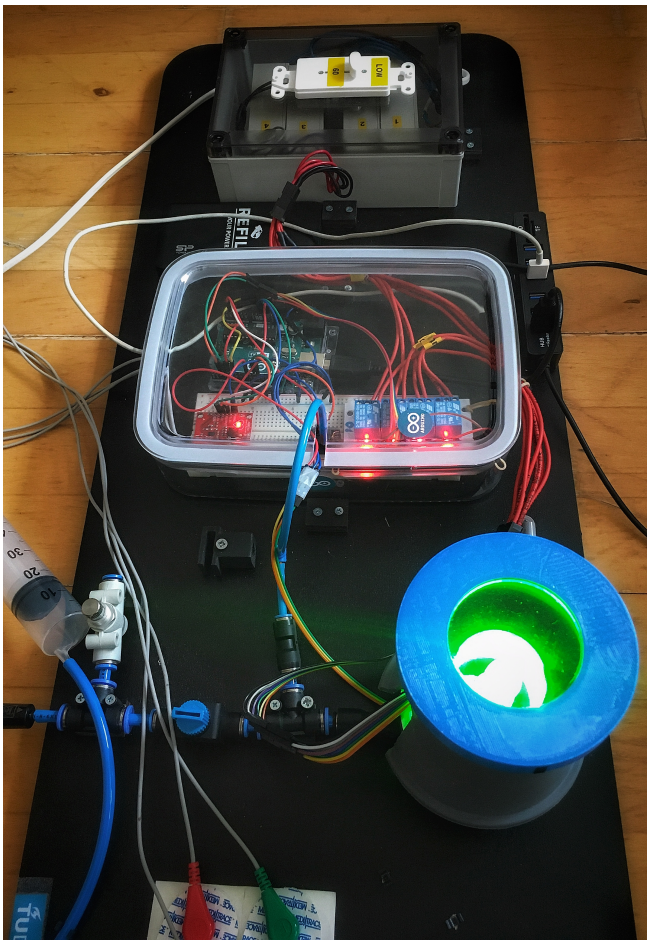

Technical University of Delft

November 2021

LED-stimulated Liquid Crystalline Elastomers (LCEs) as Contractile Units for Assisting Cardiac Contraction

by L.F.A. (Luutzen) Wymenga

to obtain the degree of Master of Science
at the Delft University of Technology,
to be defended publicly on Thursday November 25, 2021 at 11:00 AM.

Student number:	4036611	
Project duration:	September 1, 2020 – November 25, 2021	
Thesis committee:	Prof. dr. ir. G.Q. Zhang,	TU Delft, supervisor
	Prof. dr. ir. W.D. Van Driel,	TU Delft / Signify
	Prof. dr. ir. K.M.B. Jansen,	TU Delft
	Dr. ir. T. Jin,	TU Delft

This thesis is confidential and cannot be made public until December 31, 2021.

An electronic version of this thesis is available at `http://repository.tudelft.nl/`.

Supplementary movies with this thesis can be found at `https://delftao.wixsite.com/lces/`.

Contents

Summary

Heart Failure (HF) is a disease of high mortality and morbidity with huge impact on health care systems worldwide. HF is a result of decreased contraction of the heart muscle. Current treatments focus on symptoms, and only a minor portion of HF patients is eligible for surgery. Assistance devices for cardiac contraction are currently only available as bridging therapy towards heart transplantation. In this thesis, an innovative cardiac assistance device based on light-responsive Liquid Crystalline Elastomers (LCEs) is proposed. This bio-compatible polymer can generate a contractile force in response to a light stimulus. Theoretically, an LCE sheet wrapped around the heart could assist cardiac contraction. Light stimuli could be administered by an implanted LED panel to achieve the first fully implanted cardiac assistance device available. Therefore, parameters regarding light-LCE interaction were investigated. Among *state-of-the art* light sources, the best candidates for an implantable LCE device were selected. The physical mechanisms underlying LCE behaviour were explored, and LCEs in previous research were compared. Lastly, light irradiance patterns were mathematically modelled to find the optimal configuration for LCE stimulation. It was found that LCE *'MM10'* is a good candidate for our device as it is bio-compatible, tweakable in wavelength response, has fast response times and produces a large stress. The most promising light source is μLEDs, as they are small, provide high light intensity at good efficiency, and are relatively biocompatible. Modeling shows that the optimal formation of μLEDs is a hexagonal pattern, which provides the most homogeneous at the highest efficiency at very-nearby irradiance (tens of μms.

After this literature review, experiments were performed. Optical, mechanical and thermal properties of MM10 were tested. The optical experiments proved that MM10 acts as birefringent half-wave plate, meaning it rotates the direction of linearly polarized light. This finding could be used to visually determine the nematic director of MM10, with birefringence the strongest in an angle of 45° with the nematic director. Birefringence is low in the wavelength spectrum of the stimulating light source (400-500nm) and highest in the 700-800nm range. Reflection and transmission of MM10 within the 400-500nm range are resp. 5.5±0.2%and10.6±4.6%. This indicates that most of the LED light is absorbed, and thus can be converted in mechanical energy to produce stress. The order parameter was found to be 0.5. The absorption coefficient was found to be 0.081±0.006.

Mechanical analysis was divided in passive properties (without light stimulus) and active properties (with light stimulus). Young's moduli are heavily influenced by environmental temperature, where MM10 shows a >10x higher Young's modulus in the 0.1-2% strain range and a >4x higher modulus in the 4-6% strain range at $25°C$ compared to $37°C$ (body temperature). A calibrated the main-chain LCE model showed to be a good predictor of this behavior.

Dynamical analysis (DMA) showed that storage modulus decreases and tan δ increases heavily upon light stimulus. This can be explained by stiffening of MM10 upon illumination due to contraction. MM10 stress generation is optimal in the 35-40mW/cm^2 irradiance range, producing a stress of up to 80mN/mm^2 at $25°C$. At higher temperatures, elasticity will rapidly increase, leading to higher irradiance tolerance before break, but lower stress generation at the same irradiance compared to $25°C$. A mathematical model was built and tested on these findings for predicting maximum stress generation when sample thickness, irradiance and environment temperature are known.

Thermal infrared analysis showed that MM10 surface temperature rises upon illumination, as an indirect result of the incorporated azobenzene molecules, which act as *micro-heaters*. Surface temperature reaches the maximum after ±5s of illumination. Stress generation coincides with this temperature rise, until it reaches a plateau. While it is possible to pace MM10 at a rate of 1-3Hz without excessive heat build-up, MM10 has a too slow response to act as an effective contractile unit at these frequencies.

A demonstrator was built for homogeneous illumination of MM10 material wrapped around a balloon. This platform allows live measurement of pressure, temperature, humidity and ECG signals. Also, light stimuli can be triggered by real-time heart beat detection. Concentric pressure measurements showed a 20μm-thick MM10 band could produce up to 170 Pa pressure when wrapped around a balloon and irradiated homogeneously with 60mW/cm^2 green light. As such, the (very thin) MM10 band generates a substantial force of 1.29N.

We conclude that MM10 is a bio-compatible, versatile material able to produce large stresses in response to LED light. Cardiac assistance by MM10 might be too complex because of the relatively slow response time of MM10 compared to the heart rate, the large mechanical forces in the heart and the variability of the heart rate. We see multiple other potential uses for MM10 as an implant as well as outside the (human) body.

1 Literature Review

1.1 Introduction

1.1.1 Normal functioning of the heart

The heart as a pump

The heart is a crucial organ needed for all vertebrate life to pump blood through the venous and arterial system [1]. The human heart is a muscle that consists of two *atria* (smaller cavities) and two *ventricles* (larger cavities) that will be filled with blood during circulation (see fig. 1.1). Blood enters the heart via the atria. The right atrium receives blood from the superior and inferior *vena cava*. This blood circulated through the body tissues and is therefore low in oxygen and high in carbon dioxide. This blood is pumped through the right atria, via the *tricuspid* valve, into the right ventricle. From here, the blood leaves the heart during ventricular contraction (*systole*) to the pulmonary arteries. It is then pumped through the lungs, where gases in the blood are exchanged during respiration. New oxygen is deposited in the blood upon inhalation, while carbon dioxide is removed into the air during exhalation. The freshly oxygenated blood will then permeate the lung tissue into the four pulmonary veins. From here, the blood arrives in the left atrium. It is passed into the left ventricle through the *mitral* valve. This happens passively (by relaxation of the heart muscle) and actively (by contraction of the atria) and this period is called *diastole*. In the left ventricle, upon systole, the oxygenated blood is passed through the main artery of the body, the aorta. This blood cannot flow back into the heart when the aortic valve is closed, and will thus continue through the body, hereby oxygenating the tissues. Eventually, when the blood has passed through all the tissues and even the smallest veins, it is collected again in the superior and inferior vena cava and the cardiac cycle will start over (see fig. 1.2).

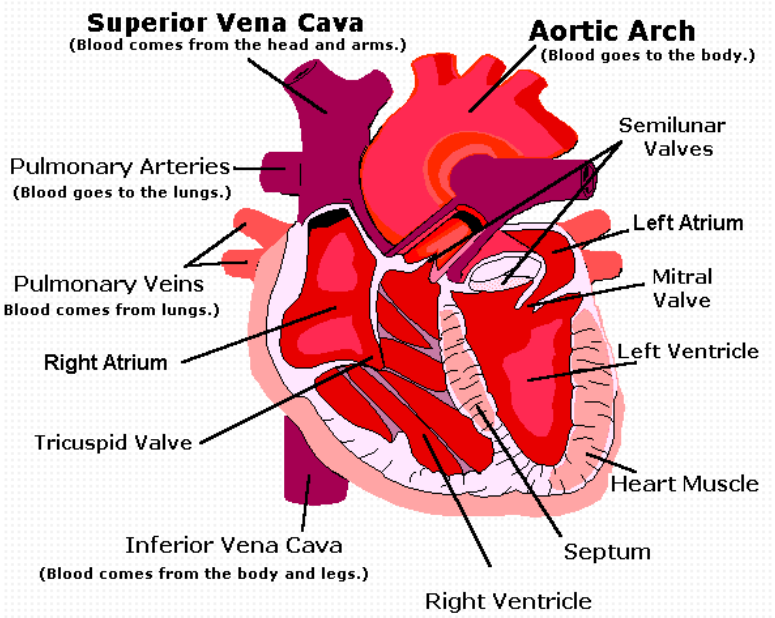

Figure 1.1: Anatomy of the heart [2].

Timing of heart contraction

The contraction and relaxation of the heart muscle is reflected in the heart rate. It is regulated by electrical signalling, originating in the sinusoidal node, located in the right atrium. This node fires electric pulses throughout the myocardium leading to a simultaneous contraction of both the left and right atria. This leads to the diastole (see fig. 1.2, 1.3). The ventricles then contract as the electric pulse (depolarization) spreads through the ventricular myocardium. The ventricles then repolarize, which causes relaxation of the ventricles and allows blood inflow from the atria (whose are also relaxed at that point). The heart rate can be therefore regulated by the nerve system and adapt to an increased demand for oxygen (for example during exercise) or emotions (via the vagal nerve, connecting the heart to the brain). While the heart rate can be adjusted, the magnitude of contraction of the muscle cannot be regulated. The power of contraction depends on the amount of healthy cardiac muscle tissue, or myocardium. The myocardium itself is oxygenated by the blood passing through the

heart. Therefore, an impaired blood flow towards the myocardium can block the contractile power of (parts of the) heart. This is the case with myocardial infarction or bleeding. The thickness of the myocardial tissue varies with factors such as age and gender. Importantly, the thickness can be increased by physical exercise. The thickness (and thus the magnitude of cardiac contraction) can also decrease by age or diseases.

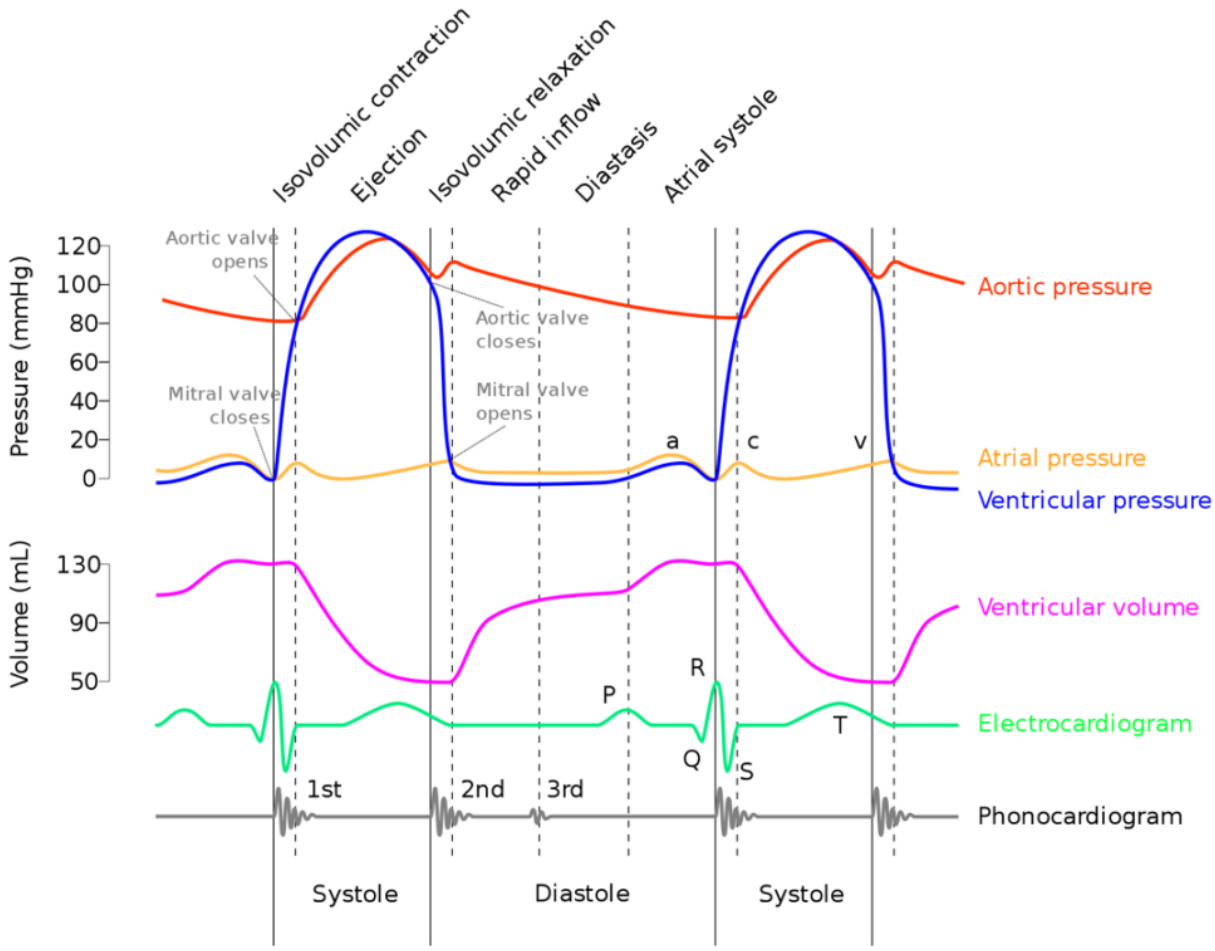

Figure 1.2: The Cardiac cycle: Blood pressure, electrical signalling and murmurs. This figure shows the aortic, atrial and ventricular pressure during two beats of the heart. Pressure is the highest in the ventricles during contraction. This causes the blood from the ventricles to be pumped out of the heart via the aorta (left ventricle) and pulmonary trunk (right ventricle). The aortic valve opens during ventricular contraction and pressure will rise in the aorta simultaneously. Around 70mL of blood will be pumped into the aorta from the left ventricle, where the pressure rises up to 120mmHg. Blood flow from the ventricles back into the atria is prevented during ventricular contraction by the closing of the atrioventricular valves (A-V valves, consisting of the mitral and the tricuspid valve). After ventricular contraction, the ventricles relax, allowing new inflow of blood from the atria trough both a passive pressure difference as well as active atrial contraction. An electrocardiogram corresponding to the different phases of the cardiac cycle is shown, where the P-top corresponds to atrial contraction, the QRS-complex to ventricular contraction (while atrial relaxation is happening in the background), and the T-wave to ventricular relaxation. Heart murmurs that can be heard with a stethoscope are shown correspondingly [3].

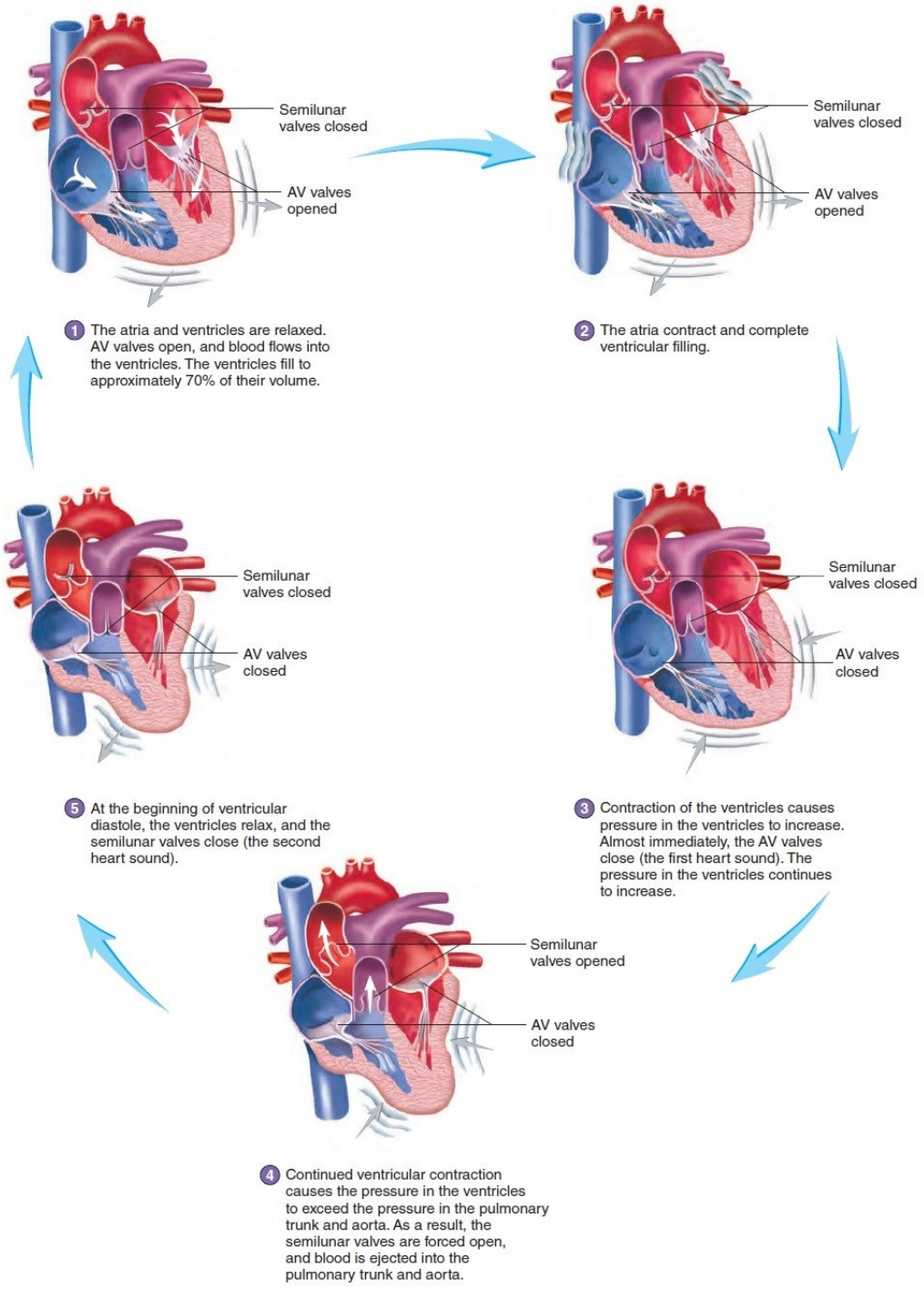

Figure 1.3: Cardiac cycle [4].

1.1.2 Heart failure (HF)

A decrease in contractile fuction

Heart Failure (HF) is characterized by a decreased contractile function of the hearts ventricles (see fig. 1.5). This can occur from 1. Small muscle thickness or 2. Decreased blood flow to the myocardium. Well-known risk factors are hypertension, diabetes mellitus (DM), coronary heart failure (CHF) and obesity (see table 1.1). A decreased contractile function of the atria is seen in atrial fibrillation (AF), but AF can lead to a loss of ventricular contractile function over time.

Risk factors for heart failure	
Diabetes mellitus (DM)	Obesity
Genetic heart diseases	Atrial fibrillation (AF)
Coronary heart disease (CHD)	Heart valve disease (aorta/pulmonal)
Alcoholism (DM)	Hypertension
Myocardial infarction (MI)	Old age
A-V valve disease (mitral/tricuspid)	Smoking
Myocardial bleeding	

Table 1.1: Risk factors associated with heart failure [5]

Symptoms of heart failure

Symptoms of HF are shortness of breath, tiredness, coughing, pulmonary oedema (*'fluid in the lungs'*), oedema in the abdomen and swelling of the ankles and feet. HF is a chronic disease that requires frequent hospital visits, not only for underlying conditions and regular symptoms, but also for frequent exacerbations or decompensation, defined as *"a gradual or rapid change in heart failure signs and symptoms resulting in a need for urgent therapy"*[5].

Epidemiology

Every year, more than 23 million people worldwide get the diagnosis HF. Although the incidence did not increase in the past two decades, survival has improved. The chronic conditions of HF with exacerbations lead to frequent hospitalisation. This means HF patients lift a high toll on healthcare systems. HF Exacerbations are the single most cause of hospitalisation for persons aged $\geq$65 years [5]. HF patients have a survival estimate of 50% at 5 years and 10% at 10 years. Also, left ventricular dysfunction is associated with an increase in the risk of sudden death [5]. Heart failure can be divided in location (right or left ventricle), heart phase (systolic or diastolic function) and percentage of preserved ejection fraction. The left ventricular ejection fraction (LVEF) is the percentage of blood leaving the ventricle into the aorta with every beat. A percentage lower than 40-55% is considered as reduced LVEF.

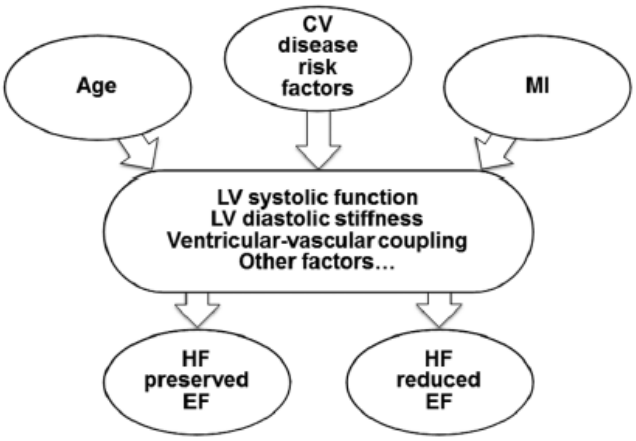

Figure 1.4: Risk factors such as age, cardiovascular disease (CV, hypertension, diabetes), and myocardial infarctions (MI) lead to decrease of ventricular performance in the heart. This leads to the diagnosis HF with or without an preserved ejection fraction (EF). Adopted from [5].

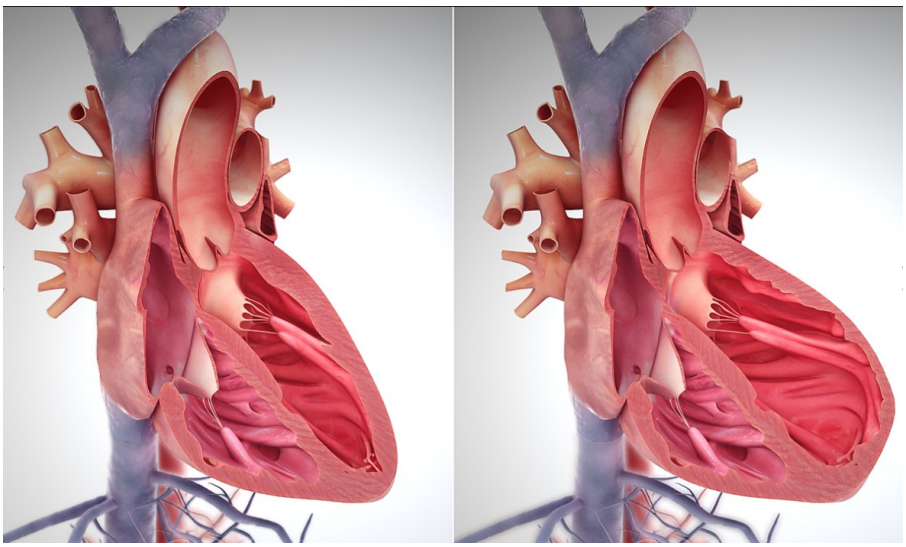

Figure 1.5: Heart failure. Left: A healthy heart muscle. Right: Left Ventricular Heart Failure (LVHF). A dilation (enlargement) of the left ventricular volume can be seen, while the muscular tissue is much thinner. This leads to an impaired ejection fraction of the left ventricular, causing an inadequate pump function of the heart [6].

1.1.3 Current treatment procedures

Lifestyle changes

Important risk factors for the development of HF are: obesity, DM, CHD and hypertension. HF patients often have multiple of these underlying conditions [5]. Lifestyle changes that can decrease the symptoms or development of HF are a healthy diet, exercise and quitting smoking. By losing weight, less tissue oxygenation is needed, and the heart has to pump less hard to meet demand. Therefore losing weight can also decrease symptoms. A healthy diet and quitting smoking both slow the progression of obesity, DM, CHD and hypertension.

Drug therapy

Drug therapies are aimed decreasing symptoms and increasing contractile function of the heart. While drugs can relieve symptoms resulting directly from HF, drugs are also given to treat the underlying risk factors such as DM, AF and hypertension. Fluid retention (the cause for shortness of breath, coughing and oedema) is treated with diuretics (increasing urine production). β-blockers lower the blood pressure and the heart rate, preventing overloading of the heart. However, this medication has the side effect of increasing shortness of breath during exercise. Inotropic drugs such as digoxin can artificially increase the contraction power of the heart. Also, cardiomyocyte specific drugs have been proposed and tested by encapsulating drugs into viral vectors that target cardiomyocytes and replicate drug particles within the cell [7]. This is still a very experimental line of research.

Surgical treatment

Surgical procedures are performed to treat specific underlying causes of HF, such as arrhythmias. Examples are cardiac re-synchronisation therapy and cardiac contractility modulation (CCM). Cardiac re-synchronisation therapy can be used to restore contractile function when there is an asynchronous contraction of the left and right ventricle. The main cause for this is a left bundle branch block (LBBB). Cardiac contractility modulation is used to allow the natural heart rate to restore, by blocking the impulses for (unwanted) contractions during the relaxation period (asystole) of the heart by injecting electric impulses. This procedure is currently recommended only for patients with a prolonged QRS complex (>120ms), which is only approximately 30% of total HF patients. The use of pacemakers is only useful for patients with arrhythmias, such as AF or atrial flutter. A heart transplantation is the intervention of last resort. This risky and costly procedure can however be of large benefit.

Left-ventricular assistance devices (LVADs)

Left ventricular assistance devices (LVADs) can actively assist the ventricles to contract. These electromechanical devices are used up to several months, as a bridge towards heart transplantation. There are two types:

pulsatile pumps and continuous flow pumps. Pulsatile pumps work with compressed air. With compressing and decompressing the air, pressure is built up to push the ventricle. Continuous flow devices use a rotor that accelerates blood towards the aorta. Continuous flow devices are smaller than pulsatile pump devices. LVADs need external power and control (see fig. 1.6). LVAD implantation has a high risk of bleeding after implantation, and thus re-operation. Also, blood clotting can occur because there is a blood flow over exogenous materials within the human body. Therefore, a permanent anticoagulant drug regiment is needed.

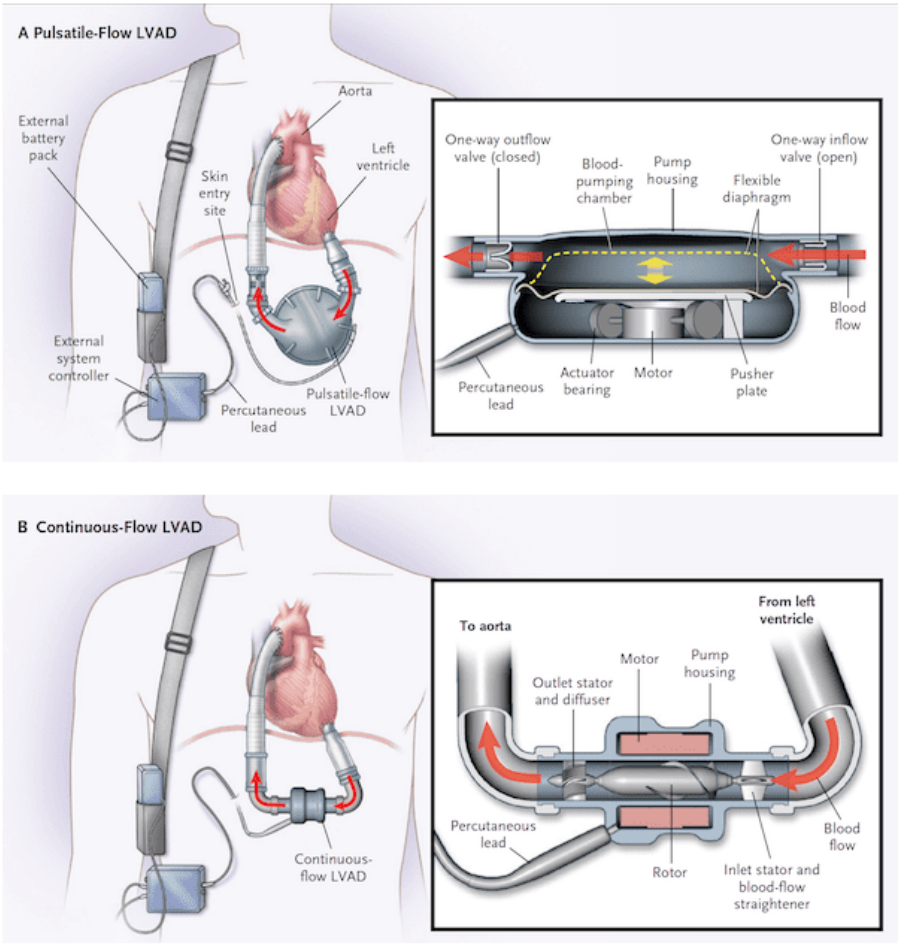

Figure 1.6: Left Ventricular Assistance Devices pumping blood from the left ventricle into the aorta. Upper image: a pulsatile-flow LVAD. Bottom image: a continuous-flow LVAD. There is external control and a battery pack attached. [8].

Genetic therapy

Recent research described the restoration of atrial rhythm in atrial fibrillation by genetically engineered atrial tissue in response to a light stimulus [7]. While this is a promising line of research, there are major ethical issues concerned with genome editing in human (cardiac) tissue. This technique might prove to improve HF symptoms that resulted from underlying atrial fibrillation.

Limitations of current therapies

Lifestyle changes do not prevent deterioration of the myocardium but only slow down the decline in cardiac function. Lifestyle changes are always beneficial as a supplementary therapy, but cannot provide a full-scale therapy for many HF patients. Drug therapies are associated with a wide range of side effects. Drug regimens are largely based on the combating of symptoms (such as oedema) instead of assisting or repairing the heart's contractile function. Surgical procedures can play a role only in specific diseases such as LBBB or AF and will thus not be sufficient for the large heart failure population with other causes for HF. Heart transplantation is a major surgery involved with a lot of risks, costs and a shortage of donor hearts. Not all patients are fit enough for such a major procedure. LVADs are associated with blood clotting risks in the case of continuous flow devices. In the case of pulsating pump devices, an external opening through the skin is needed for regulating air pressure. Perforations of the skin pose a risk of infection. A large segment of LVADs is only sufficient for bridging therapy towards heart transplantation.

1.1.4 Proposed solution: A light-stimulated contractile unit

The REPAIR project

This thesis will aim to achieve parts of the goals described in the international *Heart REPAIR* project [9]. This European project is a collaboration between multiple industrial companies, medical companies and universities to achieve the following goals:

Objective 1: Develop a mechanical performing and energetically efficient LCE material that, integrated with light sources (μLED array), will result in fundamental **biomimetic contractile units** to be structured in a suturable, remote controlled contractile tissue.
Objective 2: Use the LCEs-μLED contractile tissue to develop a new generation of **contraction assistance devices** (e.g. patches for ventriculoplasty, aortic rings for counterpulsation and epicardial bundles fibrillating atria) and test the effects of their acute implantation in large mammals (open-chest sacrifice experiments) and explanted hearts.

The project will aim for a new solution for treatment of heart failure. It consists of a **bio-compatible implantable patch that actively assists** the mechanical contraction of the left ventricle. The patch will consist of a 'smart' material known as Liquid Crystalline Elastomer (LCE) (1.1.4). The patch will actively contract, synchronously with the heart rate. A contraction of the LCE patch will be induced by a light stimulus. The stimulus circuit consisting of microscale Light Emitting Diodes (μLEDS) and wiring will be integrated into the patch. An implanted battery similar to a pacemaker battery will provide power. A wireless system must grant access to edit the settings of the patch by the treating doctor or patient himself. This thesis will mostly be based around objective 1, though some investigations around objective 2 are done.

Thesis objective

This MSc Thesis aims at three subgoals of the REPAIR project (as officialy described in the project outline):

1. **Mechanical and optical characterization** of specific LCEs suitable for the project

2. **Mathematical modeling** of the LCE behaviour based on this characterization

3. **Building a demonstrator model**. This model must be able to demonstrate that ECG signals can be used to trigger light, which then causes a measurable LCE contraction.

1.2 Measuring light (stimuli)

1.2.1 Radiometric parameters

Radiometric quantities describe the energy emitted from a light source, independent of the sensitivity of the human eye. Therefore, 'invisible' radiation such as infrared or UV is also taken into account. Now follows a quick overview of the radiometric parameters their importance. The most important radiometric parameters are radiant power (also known as radiant flux), irradiance, radiant intensity, radiance and radiant excitance [10].

Irradiance describes the amount of power received by a flat surface per unit area. Radiant excitance can be seen as the opposite of irradiance: whereas irradiance is a receiving unit, excitance is an emitting unit. The radiant emittance is equal to irradiance when an illuminated surface is reflecting 100% of the light it receives (reflection coefficient ρ=1). The radiant intensity describes the radiant power (W) in a certain direction in space, received per unit visual field (solid angle sr). The radiance describes the spatial emission characteristics of a source. This means that the radiance describes the amount of radiant power in a certain direction per unit of area of a surface near to the light source. A more detailed (mathematical) description is given below.

Radiant power (*radiant flux*) $\Phi_e(mW)$

Radiant power describes the total amount of energy (mW) emitted by a light source. All other parameters are based on the radiant power.

Irradiance $E_e(mW/mm^2)$

Irradiance describes the amount of power received by a flat surface per unit area (mW/mm^2) [10]. This surface can be oriented in any angle towards the direction of the light. Irradiance is maximized when the surface element is perpendicular to the beam (see fig. 1.7). If:

$$d\Phi_e = E_e dA$$

Then on a surface perpendicular to the light beam direction:

$$d\Phi_e = E_e \perp dA_\perp$$

The size of the area perpendicular to the light beam when the area makes an angle to the light beam direction (see image) can be calculated:

$$dA_\perp = cos(\theta)dA$$

Where θ is the angle in degrees between the incoming light beams and the illuminated surface.
And thus:

$$E_e = E_e \perp cos(\theta)$$

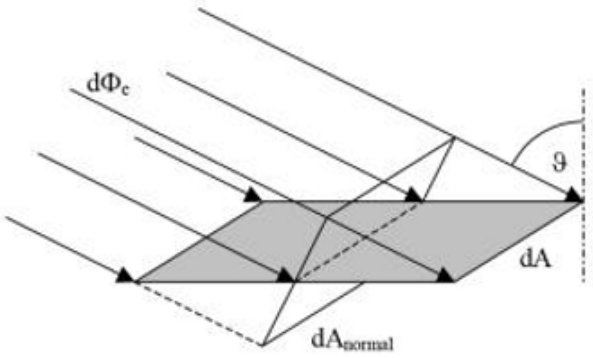

Figure 1.7: If a light beam shines on a surface, the angle θ between the light beam and the surface A influences the amount of radiant power (W) that is received per unit area.

Solid angle $\Omega(sr)$

A solid angle quantifies a part of an observer's visual field. If the visual field of an observer is described as a sphere, the actual visual field can be described as a circular area on this sphere's surface (see fig. 1.8).

$$\Omega = A/r^2(sr)$$

Where Ω is the solid angle in steradians (sr), A is circular surface on a sphere with radius r. A represents the actual visual field of an observer located in the center of the sphere. If the observer would observe everything around him, then:

$$A = 4\pi r^2$$

and so

$$\Omega = 4\pi \approx 12.57sr$$

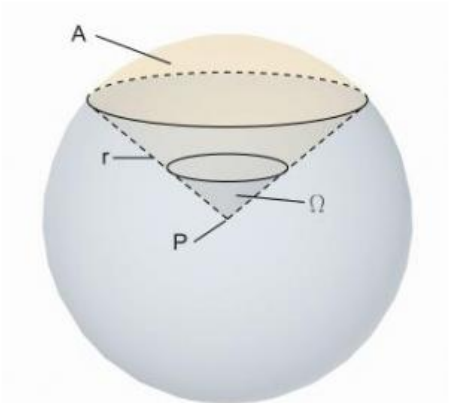

Figure 1.8: The solid angle quantifies a part of the (spherical) visual field of an observer located at point P.

Radiance ($L_e, mW/mm^2sr$) and radiant intensity ($I_e, mW/sr$) are both dependent on the solid angle. For this thesis, these parameters were not further needed.

1.2.2 Photometric quantities

Measuring the color of light

Electromagnetic (EM) waves have wavelengths varying from $1 \cdot 10^{-12}$ to $1 \cdot 10^{5}$m. Of this immense spectrum, only the wavelengths between $400-750 \cdot 10^{-9}$m (nanometer) are visible to the human eye (see fig. 1.9, 1.10).The simplest system for measuring colour of light is the nanometer wavelength color representation (among other more elaborate systems such as the tri-stimulus system) [11].

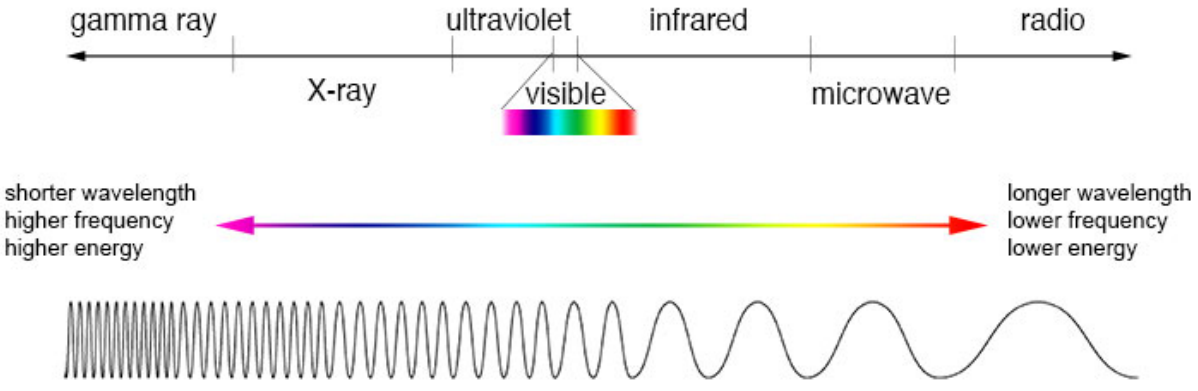

Figure 1.9: Range of EM waves. Visible light consists of only a minuscule range of the EM spectrum (400-750nm) [12].

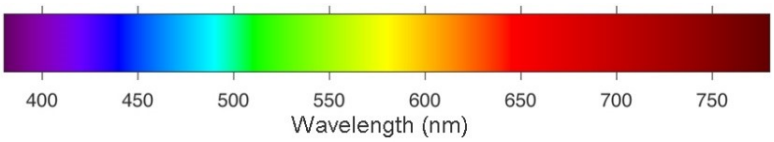

Figure 1.10: Wavelengths (nm) corresponding to colour as visible by the human eye.

A light source (with the exception of some lasers) always emits a spectrum of different wavelengths. Such a color spectrum is characterized by the peak wavelength (λ_p), the FWHM ($\Delta\lambda_{0.5}$) and the centroid wavelength (λ_c), which are all noted in nm (see fig. 1.11).

The peak wavelength is the wavelength with the highest intensity in the emitted spectrum, and the amount of spread around this peak (both in lower and in higher wavelengths) is described by the spectral bandwidth at half intensity (FWHM=full width at half maximum).

$$\Delta\lambda_{0.5} = \lambda''_{0.5} - \lambda'_{0.5}$$

The centroid wavelength divides the integral of a spectrum into two equal parts and is ideal for characterizing radiometric properties of LEDs.

$$\lambda_c = \int_{\lambda 1}^{\lambda 2} \lambda \cdot S(\lambda)\, d\lambda / \int_{\lambda 1}^{\lambda 2} S(\lambda)\, d\lambda$$

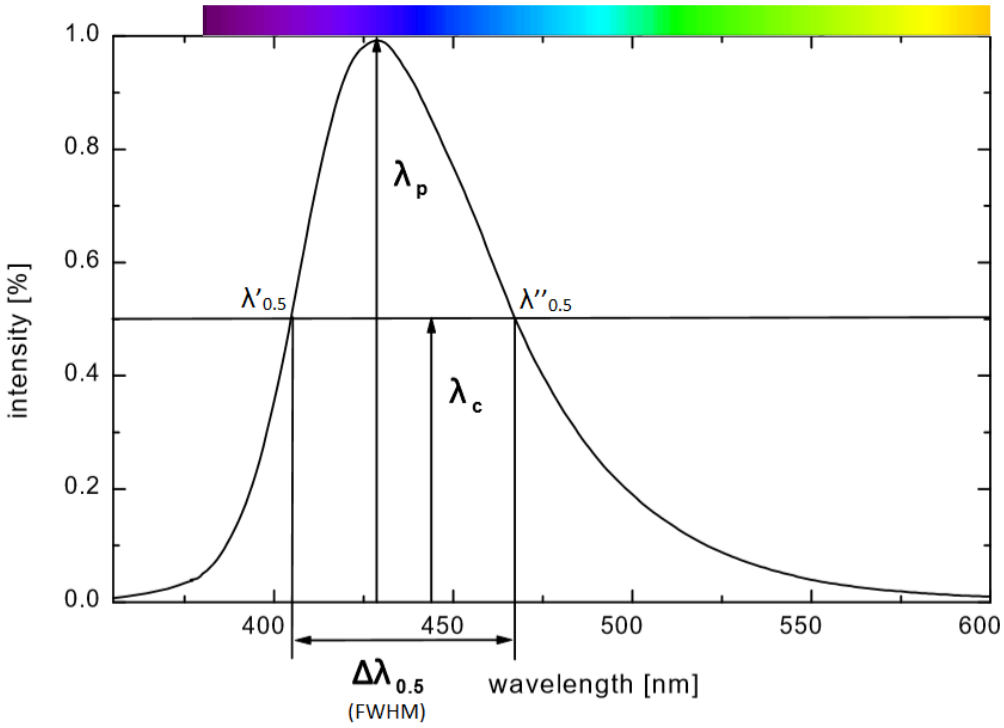

Figure 1.11: The full width at half maximum (FWHM, $\Delta\lambda_{0.5}$) describes the interval of wavelengths (nm) where the intensity of the light is minimal 50% from the peak intensity (λ_p).

1.2.3 Conversion between radiometric and photometric quantities

Optical measurements are often related to the perception of the human eye. Radiometric quantities represent the sum of radiant power (Φ_e) at an interval of wavelengths (λ). Photometric quantities are a translation of the radiometric quantities, corrected for the human eye's sensitivity to light. Therefore a a weighing factor $V(\lambda)$, known as the photopic or scotopic spectral luminous efficiency function, is introduced. Photometric quantities describe the 'brightness' of light as seen be the human eye. Normally, this conversion is done assuming daylight conditions for the human eye (photopic). Scotopic conversion is done if nighttime conditions are assumed. All radiometric quantities have an equivalent photometric quantity, for example radiant power Φ_e can be translated in to luminous flux (Φ_v, where v stands for 'visual'). Conversion is different for monochrome light (one particular wavelength with a small spread around it) or polychrome light (a broad wavelength distribution spectrum). Both photometric and radiometric quantities are used in state-of-the-art LED and lightning research. It is

thus necessary for this thesis to give a quick overview of the used quantities and their conversion. For the development of light-responsive LCE materials, photometric quantities are of less importance. The interaction of light-sensitive molecules in LCE and light does not depend on the human eye's observation of light, but on the radiometric quantities only.

Monochrome conversion luminous flux and radiant power

$$\Phi_v = \Phi_e \cdot V(\lambda) \cdot Km$$

Where Φ_v is the luminous flux (lumen), Φ_e is the radiant power (W), λ is the monochrome peak wavelength (nm), $V(\lambda)$ is the spectral luminous efficiency (dimensionless), and $Km = 683\text{lm/W}$ (constant at photopic conditions, see fig.1.12).

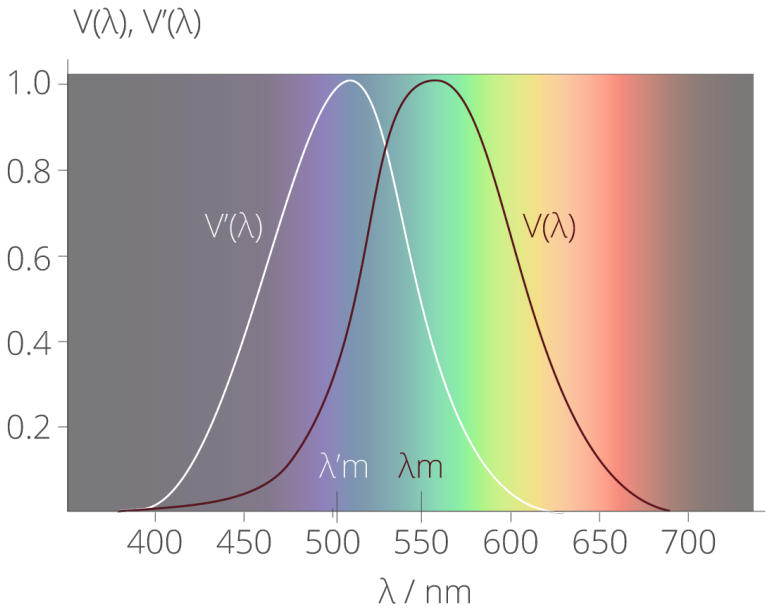

Figure 1.12: Spectral efficiency curves for photopic (daytime, $V(\lambda)$) and scotopic (nighttime, $V'(\lambda)$) vision. Peak wavelenghts per curve are displayed as λm (photopic) and $\lambda' m$ (scotopic) [10].

Polychrome conversion luminous flux and radiant power

$$\Phi_v = Km \int_{\lambda min}^{\lambda max} \Phi_e(\lambda) \cdot V(\lambda)\, d\lambda$$

Where Φ_v is the luminous flux (lumen), $\Phi_e(\lambda)$ is the function describing the relative intensity of the radiant power per wavelength over the spectrum of the light source, $V(\lambda)$ is the spectral luminous efficiency (dimensionless), and $Km = 683\text{lm/W}$ (constant at photopic conditions).

In general this formula can be used:

$$X_v = Km \int_{\lambda min}^{\lambda max} X_e(\lambda) \cdot V(\lambda)\, d\lambda$$

Where X_v and X_e can be chosen to represent corresponding photopic and radiometric quantities:
Φ_v (luminous flux, lm) $\iff$ Φ_e (radiant power, W)
I_v (luminous intensity, cd) $\iff$ I_e (radiant intensity, W/sr)
L_v (luminance, cd/m^2) $\iff$ L_e (radiance, $W/sr \cdot m^2$)
E_v (illuminance, lx) $\iff$ E_e (irradiance, W/m^2)
M_v (luminous excitance, lm/m^2) $\iff$ M_e (radiant excitance, W/m^2)

The spectral luminous efficiency curve $V(\lambda)$is a predefined curve and can be found in multiple sources (i.e. [13] or [14]). $Km = 683$ at daylight conditions but can be exchanged with $K'm = 1700$ at nighttime conditions.

Frequently used units	
Lumen (lm)	$cd \cdot sr$
Sterradian (sr)	$Area/r^2$
Watt (W)	J/s
Candela (cd)	lm/sr
Lux (lx)	lm/m^2

Table 1.2: Frequently used units and their conversion

1.3 LEDs as LCE stimuli, and use in flexible layers

In this part, an overview of currently available light sources will be given. Their properties are compared to investigate which sources are best for achieving the goals of the *REPAIR* project as stated earlier. A short note on flexible layers is given, as this is vital for the *REPAIR* project, but out of scope for this thesis.

1.3.1 The case for flexible LED layers

Flexible LED layers are an area of large scientific interest because of it's uses in display and wearables [15], [16], [17]. While current research focuses mainly on the use of LED light for displaying data, a flexible LED layer could also be used to stimulate LCE layers. LED layers could theoretically be wrapped around LCE structures, or some sort of pancake structure could be imagined, with layers of LCE and LEDs alternating. An example can be seen in fig. 1.13. For achieving a high intensity LED layer, rigid LED devices were incorporated in a flexible and stretchable network of serpentine shaped interconnects (see fig. 1.13). In this thesis, we firstly and mainly study the interaction of LED light with LCEs, and so the incorporation of LEDs into flexible layers are of later consideration.

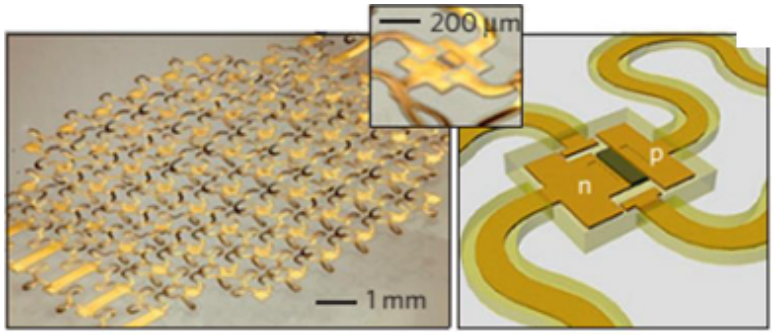

Figure 1.13: A structure of rigid inorganic μLEDs and flexible metal interconnects in a serpentine shape, increasing stretchability. The structure is placed in a somewhat buckled shape on a flexible substrate of PDMS. [16]

1.3.2 Comparison of currently available LEDs for flexible layers

OLEDs and ILEDs

Different types of LEDs are currently under investigation. LEDs are broadly divided in organic LEDs (OLEDs) and inorganic LEDs (ILEDs). Organic molecules and polymers are currently used for the fabrication OLEDs. ILEDs are fabricated on (mainly silicon) semiconductor wafers. Highly advanced silicon semiconductor technology leads to very beneficial lightning properties of ILEDs. However, this also means that ILEDs are rigid. To develop a flexible layer of ILEDs, the other structures supporting the ILEDs (such as interconnects and/or substrate) must be flexible. OLEDs, in contrary, can be made from flexible polymers. Thus, OLEDs can be made flexible. Flexible OLED sheets often consist of a layer like structure, where one full layer consists of flexible OLED material. OLEDs have shown to be tuneable in emission spectrum and easy to produce. The main concern however is decrease of performance over time. This can be solved with elaborate encapsulation schemes, to prevent the OLEDs from humidity. Even the most advanced OLEDs however have shortcomings in durability and lifetime [18]. ILEDs seem to perform better than OLEDs, showing a higher reliability and more constant performance when used in a flexible layer. Also, brightness and performance is higher than in OLEDs [18],[16].

Overview of currently available LEDs for flexible layers

A literature analysis was done on currently available types of LEDs used for the creation of flexible light-emitting layers. First, a short description of these types of LEDs is given. Then, an overview of the useful parameters for describing the quality of lightning is given. The parameters per type of LED are then represented in a table.

Micro-LEDs (μLEDs) Rigid semiconductor III-IV LEDs. These LEDs are based on a silicon or gallium arsenide (GaAs) semiconductor material, forming a p-n junction. The rigid µLEDs can then be placed on a flexible substrate like polyurethane [18].

Quantum Dot LEDs (QLEDs): colloidal double heterojunction nanorods (DHNRs). These are composed of two wide bandgap semiconductors (CdS and ZnSe, see fig. 1.14) with type II band offset surrounding and in contact with a narrow bandgap emitting centre of CdSe. These QLEDs can then be transfer printed on a flexible layer of for example polyethylene naphthalate (PEN) [18].

Perovskite LEDs (PeLEDs): Metal-halide perovskite are based on lead halides can be mounted on a flexible polyethylene layer terephthalate (PET). In 1.14 we see a PeLED of MAPbBr3 nanograins (26.7nm layer thickness) with an anode of graphene and a buffer hole-injection layer (Buf-HIL) [18].

2D-LEDs: 2D-LEDs are practically 3D objects, but are called 2D because of their tiny thickness of a few atoms thick. Layers can be stacked by just using *Van der Waals* forces. These LEDs are intrinsically flexible because of their small thickness. 2D-LEDs are direct bandgap semiconductors [18].

Polymeric OLEDs (PLEDs): Polymeric OLEDs are organic and consist of three layers: a conducting polymer, a semiconducting polymer and a metal layer. These can be mounted on a flexible layer such as polyethylene terephthalate (PET). [19]

HBLEDs: These are commercially available LEDs on millimetre scale with the property of a high brightness (such as the Philips LumiLEDs). It is defined as a LED that produces a luminous flux of more than 50 lumen [20]. HBLEDs are based on an increased heat sink capacity due to circuit board integration of the LED and addition of a thermal heat slug. Therefore, more power can be run through the LED without breaking, producing more lumens.

Light emitting chemical cells (PLEC/LEEC): Light emitting chemical cells were produced first by doping conjugated polymers with electrochemical reactions, forming p-i-n junctions in the emissive layers. LEECs only consist of a single emissive layer, contrary to LEDs [16].

Alternating current electroluminescence (ACEL): ACEL devices are based on different material layers where an electric field will induce excitation of light emission. Charge carriers are injected in one layer, accelerated under a high electric field and impacted on another layer, producing light in the luminescent centres of this layer. Often used are ZnCu powders. These can be placed in between flexible layers such as polydimethylsiloxane (PDMS) [16].

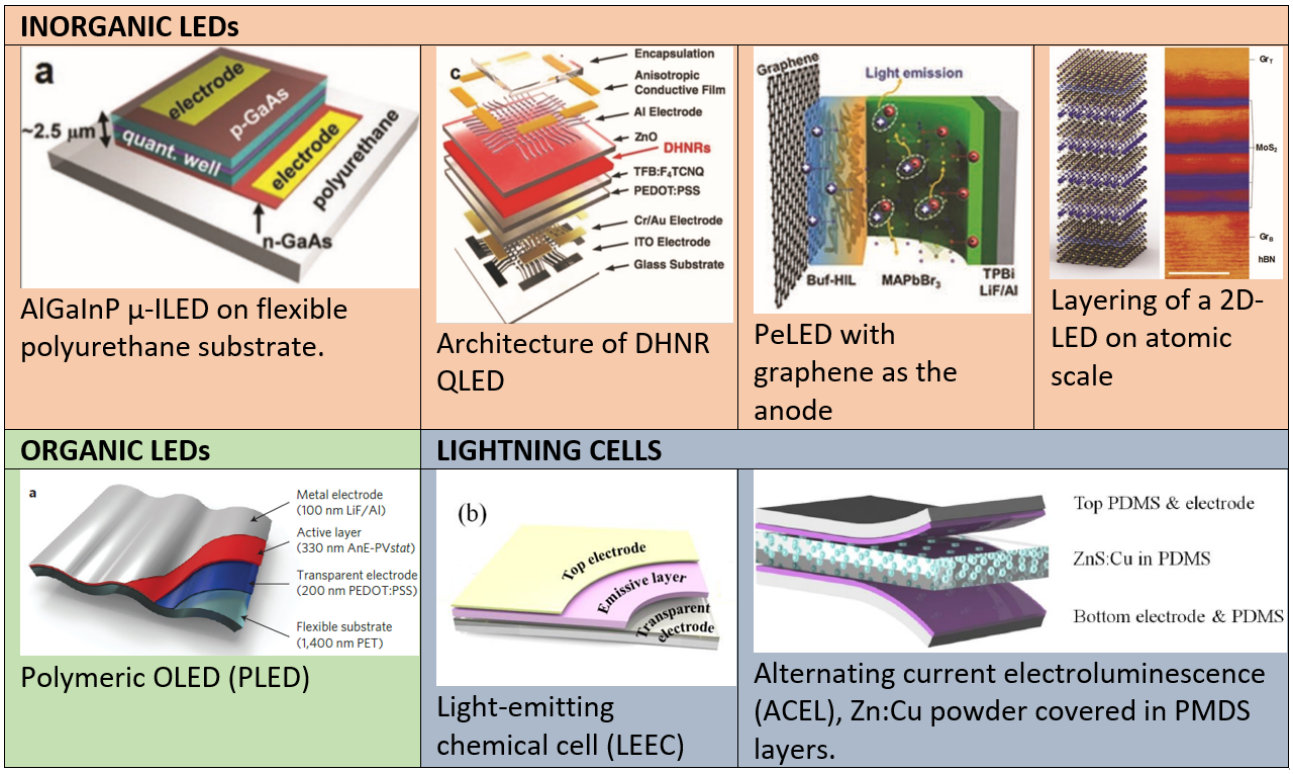

Figure 1.14: Design of several LEDs (μLEDs, QLEDs, PeLEDs, 2D-LEDs, PLEDs) and lightning cells (LEEC, ACEL) for integration in flexible, light-emitting layers. Images copied from [18],[16],[19].

Useful parameters for describing LED quality

External Quantum Efficiency (EQE): the ratio of the number of photons extracted from the device to the number of injected e-h pairs [21].

Internal Quantum Efficiency (IQE): the ratio of the number of photons emitted inside the active layer to the number of injected e-h pairs [21].

Efficiency (cd/A): Efficiency is often used in current research and describes the luminous flux (lm) per unit solid angle (sr), per Ampere (Coulomb/s) consumed by the LED. It translates (a part of) the power consumption in to efficiency of emitted light observable by the human eye, per viewing direction. Note that efficiency is expressed in candela ($1cd = 1lm/sr$).

Brightness/luminance (cd/m^2): Brightness or luminance is defined as the amount of luminous flux (lm) emitted per unit area of light-emitting layer, per unit solid angle. Note that efficiency is expressed in candela.

Luminous efficiency (lm/W): The luminous flux states the amount of lumen emitted by a light source. This is based on the amount of radiant power (W), corrected for the colour sensitivity of the human eye. Luminous flux is thus almost always lower than the radiant power, because LEDs often emit some wavelengths which cannot be observed by the human eye (spectral sensitivity = 0). The luminous efficiency can then be derived as a ratio between the luminous flux (lm) and the power consumption of the LED (W).

Strain ($\epsilon = \Delta L/L_0$): The most crucial parameter for determining flexibility of light-emitting layers. This parameter describes the %age of increase in length of a light-emitting layer by stretching, without significant decrease in lightning parameters such as brightness. Note that this strain describes light-emitting layers produced in recent research, and not the strain of the incorporated LED units themselves.

Furthermore, **thickness** of the LEDs is important. For our project, there is a need for as thin and as bright as possible flexible light-emitting layers. This asks for very small scale LEDs, likely to be in the range of micrometres. **Biocompatibility** is also important, because LEDs containing toxic particles for the human body cannot be incorporated in our design. Also, materials that can cause allergy or an immune response of the host must be excluded. **Lifetime** (hours) of LEDs is essential because an implanted device must remain in the body as long as possible, and frequent re-surgery or re-implantation must be prevented for the health of the patient. The typical industry standard is 10.000 hours of operation for LEDs [21]. At low temperatures, LEDs can even function longer, for up to 50.000-10.000 hours.

Spectral tune-ability are parameters describing the colour of light emitted by the LEDs. The goal of lightning in this project is to activate the light-responsive molecules within the LCE as efficient as possible. These molecules are responsive to only certain parts of the colour spectrum, thus developing a LED approaching this spectrum of light emission as close as possible results in more efficiency of the whole device. More information on these parameters can be found in section [22]. Most LEDs can be made in a variety of colours. However, some techniques allow a very precise tuning of the colour spectrum (high spectral tune-ability).

Comparison of types of lightning as described in up-to-date papers

Analysis of light use for cardiac assistance device

In table 1.3, one can see that there are a lot of different parameters which have to be decided on to choose a type of lightning for a flexible light-emitting layer. Therefore, we first set criteria for our device, and secondly match the properties of each light type to the criteria. The main goal of the light stimuli is to contract a LCE. Therefore, light must have a high irradiance (around $1mW/mm^2$ on the LCE surface [1]), and the right wavelength. The responsivity to different colours of light can of course be regulated by incorporating different light-responsive molecules in the LCE. Light filtering could be used but would decrease efficiency of the system not only by loss of ineffective wavelengths emitted by the light, but also by weight increase of the system. The scale of the lightning units must be as small as possible, because then the light-emitting layer is as thin and as flexible as possible. Flexibility decreases linearly with layer thickness decrease [25]. From a biological perspective, our lightning source must be biocompatible to a high degree, especially because our final device will be implanted within the human body. This implicates also that there must be as less re-implantation and re-surgery as possible. Therefore, a light source with a high lifetime is necessary. A light source such as halide

	µLEDs	QLEDs	PeLEDs	2DLEDs	Bulb [23]	(P)OLEDs	HBLED	PLEC[16]	ACEL [16]
scale	µm	nm	nm	nm	cm	µm	mm	μm	μm
EQE (%)	>60	15.6(Fl,G)	8.5(G)	8.4		20 [21]		27	
IQE (%)	>70					25 [21]			
Efficiency		65.3(G)	42.9(G)	0.65				99 [24]	
Brightness		218800(G)	13000(G)	1000	2.8e-4	113 [19]		1910 [16]	200e-4
		7600(B)	20000(Gl)						
		Fl.:20000	Fl.:1000						
Lifetime	>50000	>10000			<15000	10000 [17]	>10000		
Lum. eff.	>200				90		>300		5
Thickness	<2.5µm	<2.5µm	200µm	10 atoms		<2.5µm [19]	5mm		40µm
Strain	100%	20%	2%			200% [19]		120%	80%
Sp. tuneab.		++	+++			+			
FWHM		30nm	20nm			40-60nm			
Biocomp.	++	+	-	++	-	-			

Table 1.3: Characteristics of currently available lightning techniques for integration in flexible light-emitting layers. Description of parameters and types of lightning can be found in text. As a referential point, some characteristics of a standard fluorescent light bulb lamp are also included.[18], [20]. * PLEC is also known as LEEC. Fl: flexible, R/G/B: Red, green, blue light. Gl: On glass plate

metal PeLEDs are toxic to the body when leaking. These are thus not biocompatible. A Pugh matrix was produced to evaluate all types of lightning on these criteria (table 1.15).

Criterium	µLEDs	QLEDs	PeLEDs	2D LEDs	HBLED	(P)OLEDs	LEEC	ACEL
Thickness	++	+++	+++	+++	+	++	++	++
Lum. Eff.	+++	++	+	+	+++	-	+	-
Lifetime	++	+++	?	?	+++	+++	-	-
Biocomp.	+	+	-	+	+	+	-	-
Strain	+++	+	+	+++	?	+++	+++	+++
Colour	+	+	+	+	+	+	+	+

Figure 1.15: Pugh Matrix: Comparison of all available light sources for LCE stimulation from usability in a cardiac assistance device, based on literature.

We see that three sources of lightning are not biocompatible (PeLEDs, LEECs and ACELs) because of the potential leakage of toxic metals they are composed of (table 1.15). These are thus excluded for our device. Regarding thickness, the remaining sources are all within micrometre-nanometre range of thickness, which is allowable. The most efficient of these sources are the µLED and the HBLED. We prefer these sources above QLEDs , 2D-LEDs and P(O)LEDs because the brightness of these sources is far below the desired irradiance of $\pm 1 mW/mm^2$. It is known that μLEDs can be incorporated in a flexible layer and perform very constant, even after thousands of stretches. This is not the case for organic LEDs such as polymeric (O)LEDs. HBLEDs produce a very high brightness, but are generally too large (a few millimetres) and heavy to be effectively incorporated in a flexible LCE device [20]. **Therefore, the only reasonable choice for this project seems to be μLEDs.**

1.3.3 Useful LED parameters

Near zone / far zone lightning When light is irradiated on a flat surface, the irradiance (E_e) of that surface (in mW/mm^2) follows the inverse square law [11]. This means that the irradiance decreases with a factor d^2 as the distance d between the surface and the light increases. This law holds if we consider the light to be a point source: that is, if the length and width of the source are far smaller than the distance between the light and the illuminated surface:

$$l_{source}, w_{source} \ll d_{source-surface}$$

This is also called far zone illumination. In contrast, near zone illumination can be defined as:

$$l_{source}, w_{source} \approx d_{source-surface}$$

and **near zone illumination does not follow the inverse square law** [26]. It can be seen that in the near zone, the irradiance decreases less per unit distance between LEDs than in the far zone (fig. 1.16).

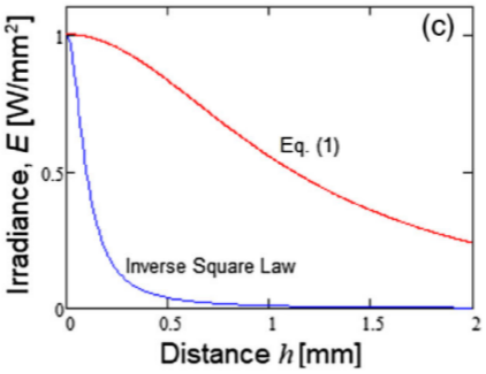

Figure 1.16: The difference in irradiance of a surface on distance h of the light source between far field illumination (blue inverse square law), and near field illumination (red), copied from [26].

In this thesis, our main interest is the lightning pattern at short distances, where even a distance of zero between the LED surface and the illuminated surface should be considered. Thus, the model for near zone LED irradiance will be used here.

Homogeneity of irradiance When a flat surface is interacting with light, it must be determined if the surface is Lambertian or non-Lambertian. Lambertian means that the surface reflects or emits light in a homogeneous pattern similar to a hemisphere. Non-Lambertian is any other reflecting or emitting pattern than this hemispherical homogeneous pattern (see fig. 1.17) [27]. A Lambertian emitter has a constant radiance L_e ($mW/mm^2 \cdot sr$) and an half-intensity angle of $\Theta_{0.5} = 60°$. A non-Lambertian emitter has a radiance dependent on the viewing angle θ_s, the angle between the light source and the observer. The light directionality m can be determined by the half-intensity angle $\Theta_{0.5}$. Then, the radiance of the source L_0 can be determined by using the radiant exitance M_e. Then, the radiance dependent on the viewing angle can be determined:

$$m = -ln(2)/ln \cdot cos(\Theta_{0.5})$$
$$L_0 = M_e(m+1)/2\pi$$
$$L_e = L_0 \cdot cos(\theta_s)^{m-1}$$

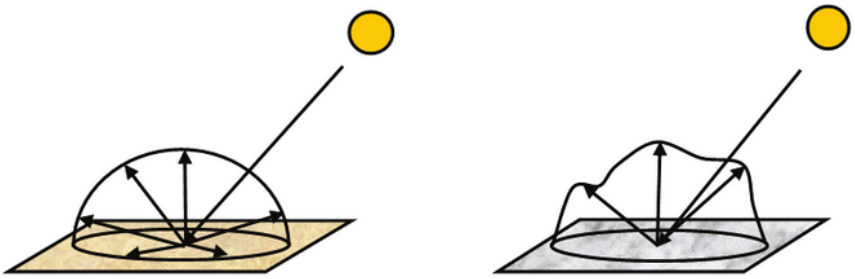

Figure 1.17: Lambertian reflecting surface (left) and non-Lambertian reflecting surface (right) [28].

1.4 Workings of LCEs

1.4.1 LCEs

Liquid-crystalline elastomers (LCEs) are well known for their ability to perform a reversible shape-change in response to an external stimulus, such as light, heat or pH [29], [30]. LCEs were already described as *'artificial muscle'* in 1997 [31]. LCEs could be considered 'smart' materials as they can be designed to react to predetermined stimuli only, while not reacting to other stimuli. For example, an LCE miniature grabber was developed that closes only in reaction to a certain intensity of light, while staying open when different intensities of light (or other possible stimuli such as heat) are present [32]. Two main benefits of LCEs compared to other deforming materials are the complete reversibility of the shape transformation and the possibility to apply different predefined movements such as bending and rotation [33]. Furthermore, LCEs have proven biocompatible properties, and thus could be a candidate for use in implants [34].

1.4.2 LCE structure

LCEs are composed of polymer networks with liquid crystals incorporated. These liquid crystals are also called mesogens, and can be attached in the polymer chain itself or onto the sides of the chain (*main-chain* or *side-chain*). A liquid crystal can be described as a somewhat melted crystal, displaying both properties of the original crystal matrix, as well as isotropic (fully liquid) properties. Liquid crystals (the **LC state**) exist at a specific temperature range, where cooling leads to the original rigid solid state of the crystal (**Cr state**), and heating leads to a liquid or isotropic state of the crystal (**Iso state**). As such, a liquid crystal has different properties at differing temperatures. Within the LC state, there exists the **nematic** state (the most fluid), the **columnar** state (most rigid) and the **smectic** state (in between) (see figs. 1.18, 1.20).

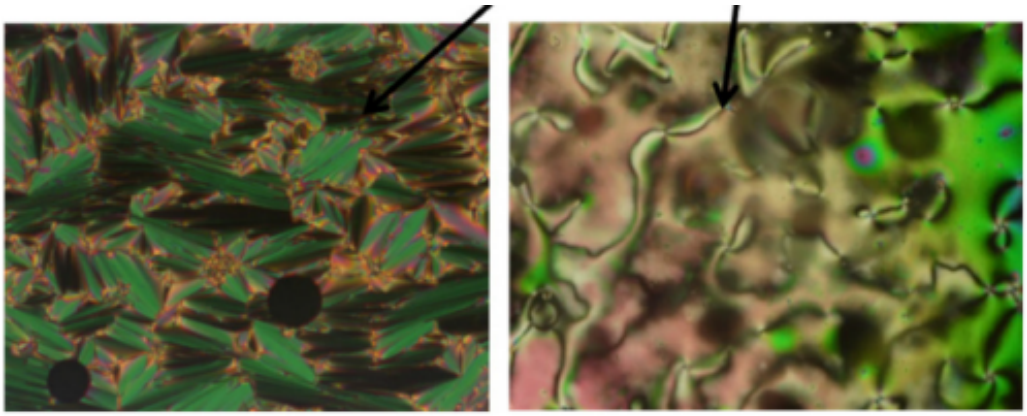

Figure 1.18: A liquid crystal in smectic (left) to nematic phase (right). The more solid smectic phase is characterized by organized layers of molecules. The nematic state is a more fluid state than the smectic phase, with free-flowing molecules that are oriented however in a particular direction as a thread. This phase can be reached from the smectic state by heating the liquid crystal (adopted from [35]).

The shape change of LCEs depends on the local alignment of the liquid-crystal director field within the polymer network [32]. The alignment of the liquid crystal molecules is programmable during LCE production. Thus, predetermined movements can be made possible [36]. The liquid crystals in LCE force the polymers to stretch in one direction, parallel to the crystal orientation of the more rigid parts of the liquid crystal. But when a LCE is heated, the rigid parts of the liquid crystal become more liquid, removing the force of the liquid crystal on the polymer chains. As a result, these polymers will deform from the original stretched directional conformation into a more randomly oriented coil formation (the relaxed state of polymers). This leads to a macroscopic deformation of the LCE shape. If a block of LCE has the polymers oriented parallel to its longest side, this side will shorten upon heating. Sides perpendicular to the polymer orientation will elongate, so that an isovolumetric contraction occurs. In fig. 1.19 it can be seen that such a block will thus become squarer in response to heating.

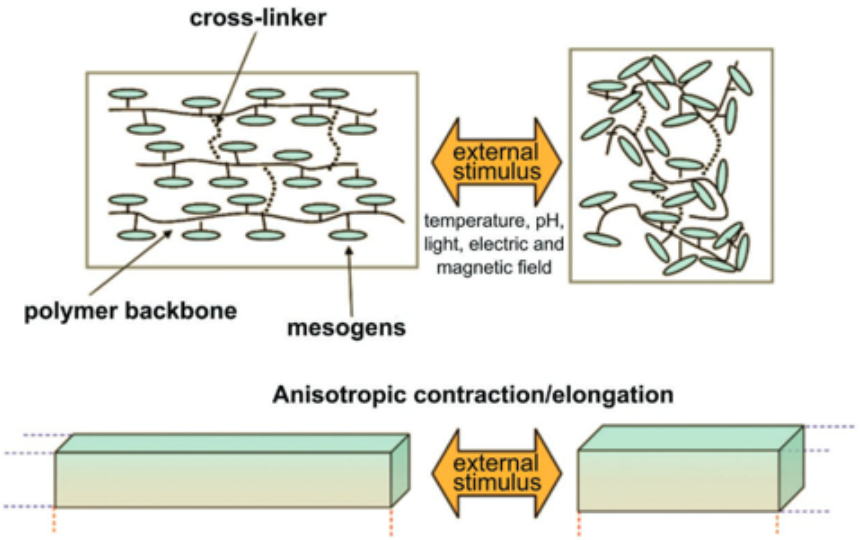

Figure 1.19: Adapted from [33]. Anisotropic contraction and elongation of an LCE block as a result of an external stimulus on micro- and macroscopic scale. This stimulus causes the liquid crystals (mesogens) to become more fluid, thereby releasing pressure from the stretched polymer backbones. As a result, the polymers will wrap in to a more randomly oriented coil formation (upper image). On macroscopic scale, this results in the contraction of a stretched piece of LCE into a squarer piece (lower image).

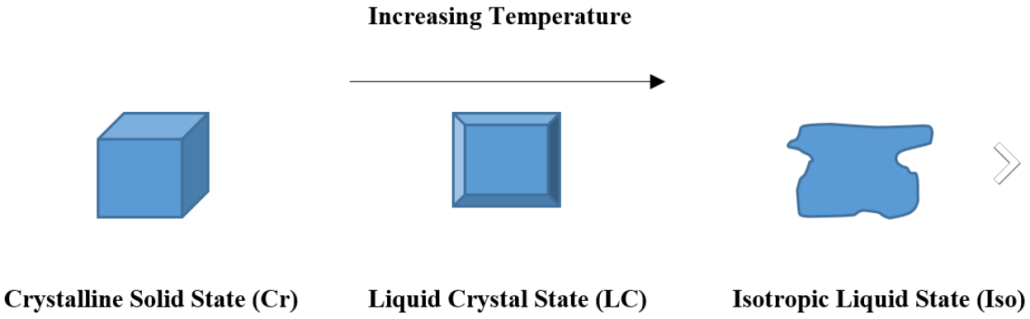

Figure 1.20: A liquid crystal is a crystal formation in between the crystalline solid state and the isotropic liquid state. In the liquid crystal state, a crystal consists in a varying degree of crystal matix and liquid crystals. An increasing temperature (or other stimuli) can shift a solid state crystal in to a liquid or liquid crystal state (*source:Wikipedia*).

1.4.3 Light-stimulated LCEs

When temperature of an LCE is kept constant, LCEs may transform due to other pre-programmed stimuli. Light is often used and has been described in micro motors, micro mills and grippers [32]. Main advantages for the use of light as stimulus are: wireless transmission, use of very specific colour, intensity and polarization, easy steering of the light source, and fast response in time [33]. To produce a light-sensitive LCE, a photosensitive molecule must be incorporated into the liquid crystal mesogen. **Azobenzene molecules** ($C_6H_{10}N_2$) are often used for this purpose, in so called monomer azo-dyes within the LCE [33]. Azobenzene molecules react to UV-light by trans-to-cis isomerization (fig.1.21). Azobenzene can perform **trans-to-cis isomerization** via an inversion-assisted torsional pathway [37], [38].

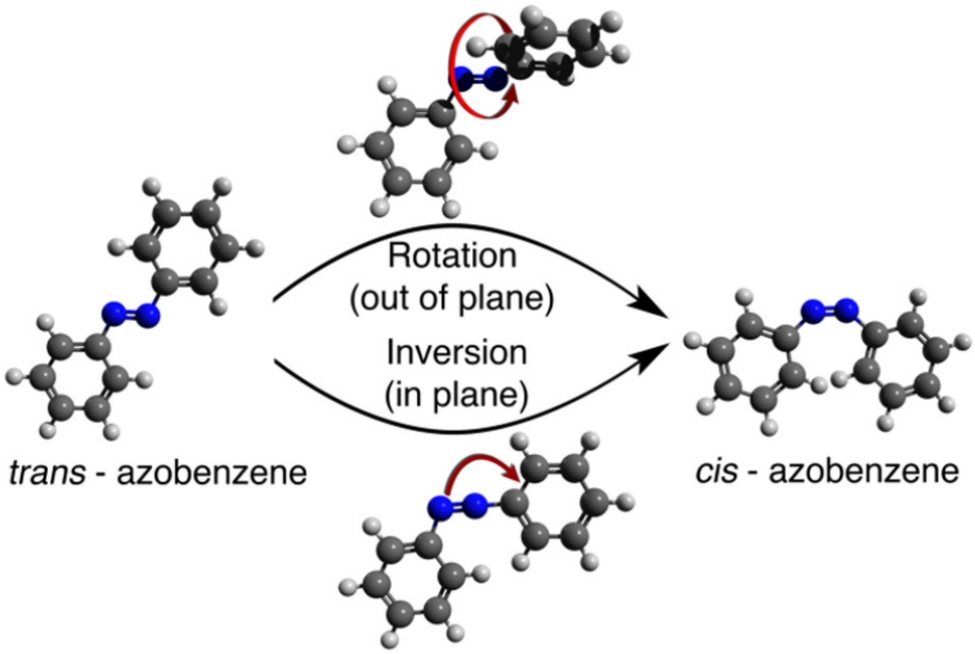

Figure 1.21: Azobenzene molecule trans-to-cis isomerization occurs with light absorption and is performed through out-of-plane torsion (rotation) of the N-N bonds, assisted by a degree of in-plane inversion (bending) of one of the C-N bonds. Copied from [37].

Under conditions of no light stimulus, azobenzene molecules in the LCE are predominantly in trans-isomer shape, which have a greater volume than in cis-isomer form [39]. Absorbed light energy loosens the $N-N$ bond in a azobenzene molecule to the point where the end groups may start to rotate, causing a shift from a majority of trans-isomers to a majority of cis-isomers [39]. If light radiation is sufficient, the azobenzene trans-to-cis isomerization will cause the whole LCE to transform. Thus, the shape-shift in the azobenzene molecules will be propagated through the entire material via the liquid crystals phase transition [40]. The azobenzenes act as a **push-pull system** within the LCE. A transformation is then thus reached in an environment with a constant temperature. When irradiation is turned off, azobenzene molecules return to cis-configuration, raising the phase transition temperature of the mesogens in the LCE above the surrounding temperature, causing the LCE to transform back to its original shape. A fully reversible transformation can be reached with movements of up to 50% of the LCE samples length [41]. At room temperature, >90% of azobenzene molecules is in the thermodynamically stable trans-isomer shape, providing a large reservoir to undergo trans-to-cis isomerisation upon irradiation [42]. Interestingly, a very accurate alignment of polymers can even enable transformation of LCEs in reaction to specific polarization of light [35]. Furthermore, azo-dyes could be chemically edited to change the spectrum to which the azobenzenes are reactive. Azobenzenes reactive to green light (530nm) but non-reactive to UV-light were created [43].

Thermo- and photomechanical reactions

Azobenzene can react to light via two mechanisms: through a thermo-mechanical reaction or a photo-mechanical reaction. Previous research showed that a laser with an intensity of $25mW/mm^2$ can raise temperature locally in the LCE material around azobenzene molecules up to 100°C [1]. However, this method of stimulation has limitations because of dye bleaching. Azobenzenes will therefore absorb less light and both heat production and trans-to-cis isomerization will decrease. The mechanical reaction of the LCE will decay over time and thus higher intensity light is needed to provoke the same movement in the LCE [1]. LCEs exposed to high temperatures can result in a permanent droop due to material softening [44]. This problem can be solved by low intensity irradiation of LED light in a water bath. This chemical induced reaction acts only on the trans-to-cis isomerisation of azobenzenes. Neglible heat (<1°) is produced near the azobenzene molecules, because of a lower intensity of light and a better cooling of the material in water when light is turned off. No dye bleaching is observed. Furthermore, no decline LCE movement is seen over time. Fast reaction times (20-30ms) can be reached in LCE movement, similar to atrial muscular tissue and twice as fast as ventricular muscular tissue [1]. Low intensity LED irradiation would therefore be preferred to use in implants in the human body over high intensity laser irradiation.

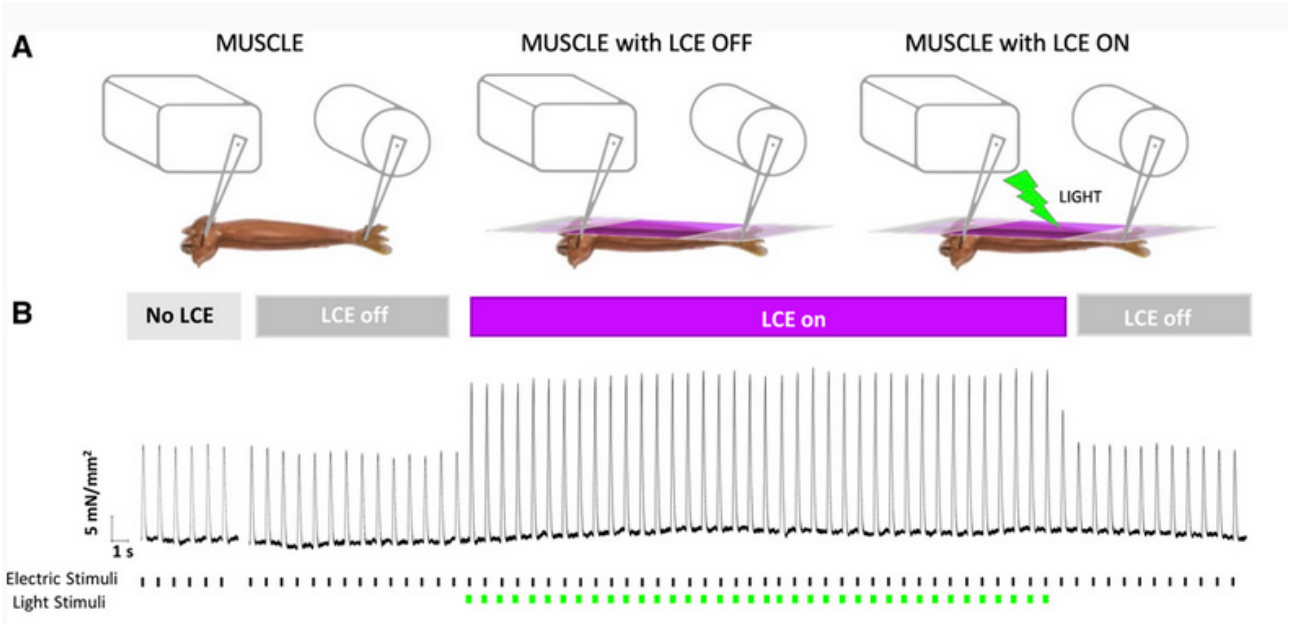

(a)

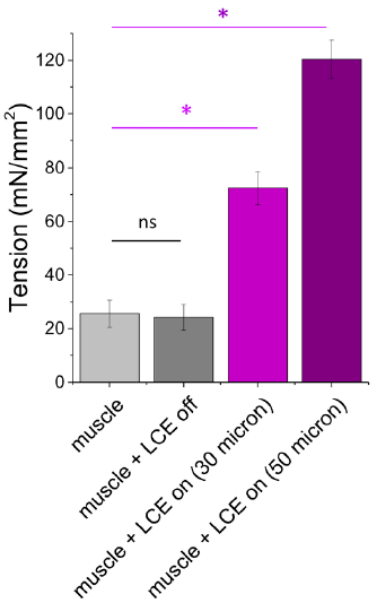

(b)

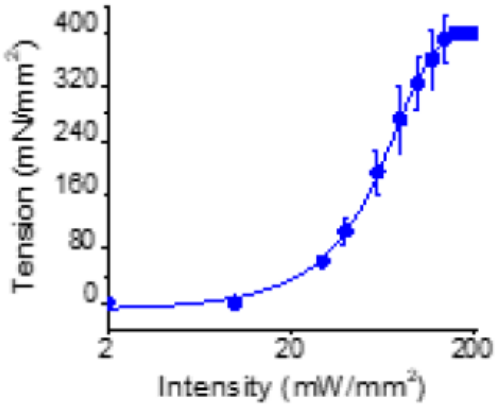

(c)

Figure 1.22: Adopted from [1]. A healthy mouse right ventricular trabecular muscle is shown pinned between a force transducer and a motor and stimulated (electric stimulus, 60 bpm). Then, a 20μm strip of LCE is added between the holders parallel to the muscle and electric simulation is given again. Finally, electric stimulation is simultaneously given with a green (525nm wavelength) LED stimulation (of 1.5 mW/mm^2). A force-time diagram in part B shows a higher contractile strength of the stimulated muscle combined with a stimulated LCE compared to a stimulated muscle without a (stimulated) LCE strip. The passive tension is not influenced. Thus, LCE strips enhance active tension of a muscle when simultaneously stimulated, while no effect on passive tension is observed. Quantitative effects are shown right. It can be seen that an LCE significantly enhances contraction, almost tripling the amount of tension of an unassisted muscle. When LCE strip thickness is increased from 30 to 50μm, the tension is enhanced six times compared to an unassisted muscle! Copied from [1]. A relation between the irradiation of a LCE strip and the tension when contraction occurs. The intensity of irradiance varies from 2-200 mW/mm^2. The tension is measured with a force transducer and corrected for thickness of the sample as mN generated per mm^2 cross-sectional area. Other factors influencing the tension are light-responsive dye type and concentration and overall recipe and production method of LCEs.

Molecular effects during thermo- and photomechanical reactions

The photo-mechanical and thermo-mechanical effect of light stimulus both work in the same direction, causing LCE contraction by phase transition from ordered to disordered alignment (see fig. 1.23). The mode of operation however is contrary. The photo-mechanical effect works by lowering the phase transition temperature (T_{phase}) below the LCE temperature (T_{LCE}). The thermo-mechanical effect works by raising the environmental temperature above the phase transition temperature. The photo-mechanical appears to be the main driver, as similar contraction is achieved with and without the appliance of a heat sink, thereby preventing heat build-up [45]. However, it was showed that there are large local temperature increases (30-40°C) possible within LCEs as reaction to light stimulus [46]. Thus, a local thermo-mechanical effect on molecular scale cannot be ruled out as a main driver for the LCE contraction. Furthermore, LCEs were prepared with light-responsive molecules other than azobenzenes (such as *Disperse Blue 14*) [46]. These molecules do not possess trans-to-cis isomerization properties in reaction to light, however the LCEs in which these molecules were incorporated reacted in a similar fashion to a light-stimulus as did the azobenzene-based LCEs (at 0.7 mW/mm^2 irradiance). This would suggest that heat generation on a molecular scale near these dyes in LCE is mainly responsible for the contraction instead of isomerization, which seems to be the main driving force in azobenzene dyes [46], [45].

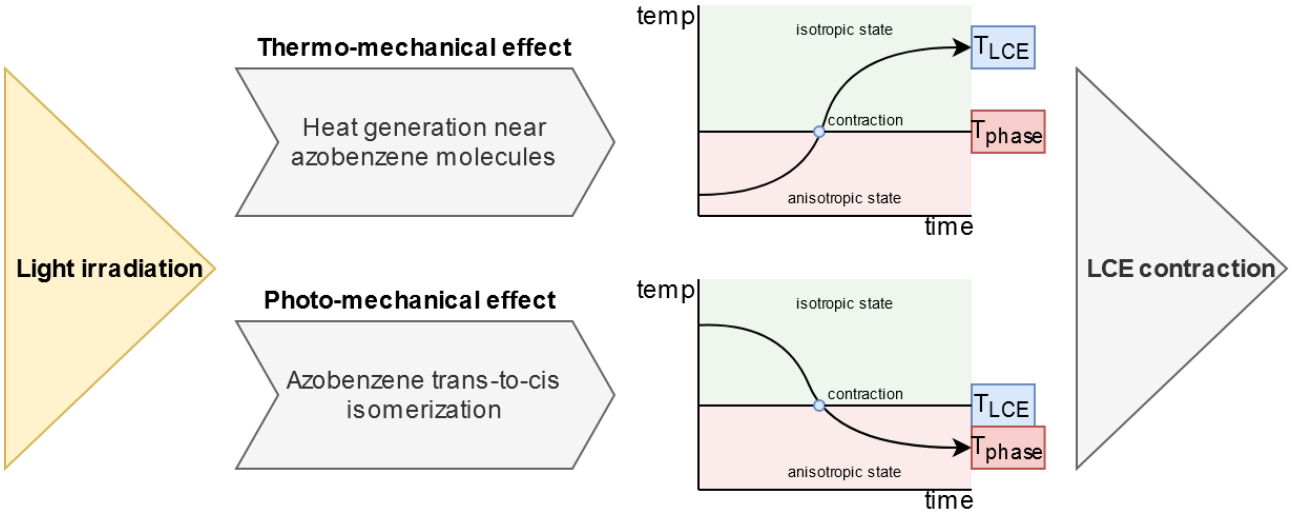

Figure 1.23: The different routes of operation between the photo-mechanical and the thermo-mechanical effect are shown when an azobenzene-dyed LCE is irradiated. Both effects result in LCE contraction but in opposite fashion. The thermo-mechanical effect raises the LCE inner temperature above the phase transition temperature, inducing a phase transition from anisotropic (elongated) state to isotropic state (contracted). The photo-mechanical effect lowers the phase transition temperature below the inner LCE temperature through azobenzene isomerization, resulting in a similar phase transition.

Relaxation time

Verpaalen et al. showed that a 4μm thick azobenzene-dyed LCE layer deposited on a 12μm thick polyethylene substrate could bend the substrate easily, with bending speeds up to those of a single 20μm LCE layer [47]! This was reached by stimulating the LCE with 1.7mW/mm^2 UV irradiation. However, the relaxation time (when the UV-light stimulus was turned off) was quite long, in the order of hours. In similar fashion, *Pang et al.* tested LCEs with an extremely large (up to 80% of original length) and powerful contraction (fig. 1.24, [48]). Unfortunately, these LCEs do not relax at all and will stay in contracted formation after stimulus. These fibers could only be brought back to the original length by reheating. The LCE properties are determined by its recipe. It is possible to produce LCEs with a fast contraction and relaxation time (in the order of ms) as *Ferrantini et al.* showed (fig. 1.22). This short relaxation time is needed when a material must follow heart contraction. Based on above research, there appears to be a trade-off between contraction force and relaxation time. It is our belief that an optimal balance between contraction force and relaxation time of LCEs can be found. Though contraction time depends on light intensity and temperature, these factors appear to be of minor importance compared to the illumination time t_{on} [1], which is a derivative of the responsivity to light of the LCE as determined by the ingredients and production process. For example, the degree of sensitization to light highly depends on the dye concentration, but not in a linear fashion. A higher concentration of dye increases the sensitivity to light, but decreases the penetration depth of light into the LCE [46].

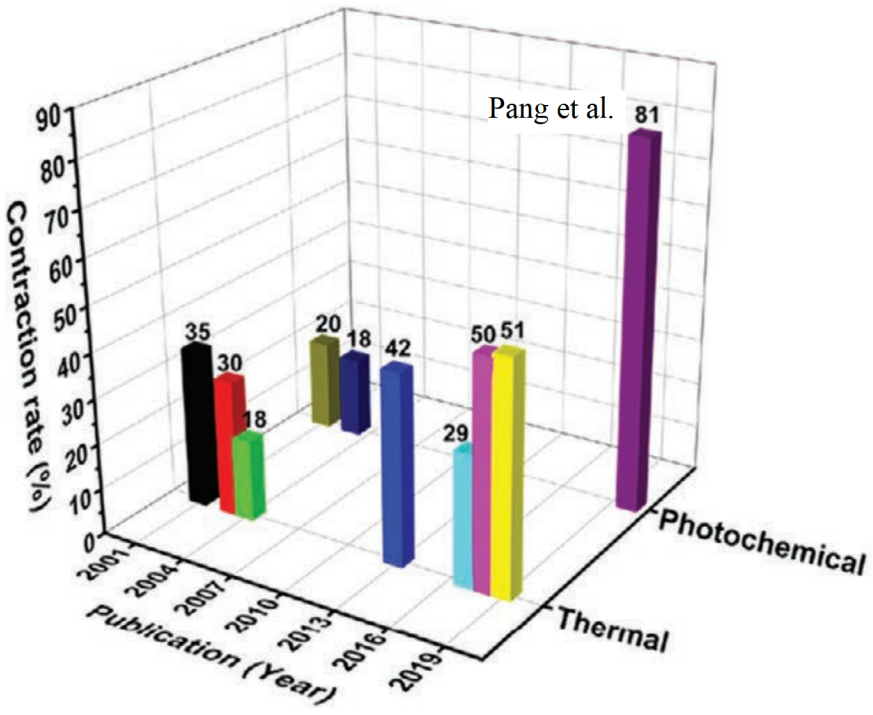

Figure 1.24: Image from [41]. Contraction rate (%age shrinking of original length) of LCE samples responsive to heat (thermal) or light (photochemical) as reported in various papers from 2001-2020. It can be seen that the largest contraction till date was reported by *Pang et al.* through a light stimulus [48]. This is however a non-reversible contraction.

Photobleaching

Photobleaching is the effect of a decreased azobenzene responsivity to light after long periods of exposition to high intensity light. Ferrantini et al. observed a photobleaching effect after constant irradiation of 24 days with a $200mW/mm^2$ laser in air. Contraction force decreased with 68% because of this effect. The effect could be fully resolved by changing the position of the light source 2mm in the horizontal plane regarding the LCE sheet. When a wide illumination in water was applied by a LED strip ($1.5mW/mm^2$) there was no photobleaching observed, not even after 2 million bending cycles [1]! This would equal to 23 days of constant cardiac assistance at a heart rate of 60 bpm.

Weigert effect, order parameter

When azobenzene molecules are illuminated with a wavelength to which they are responsive, not only reversible *trans-to-cis* isomerization occurs. There will also be a reorientation of the molecules. The long axis of the molecules will turn parallel towards the light source when these molecules can freely move. This is called the **Weigert effect**. Previous research showed a LCE tube of which the diameter increased upon irradiation. The initial portion of azobenzene molecules that was not parallel aligned to the light source rotates more towards parallel alignment [49].

Trans-isomers prevail in most LCEs over cis-isomers because of their greater volume and the thermodynamically stable nature of trans-isomers (as opposed to cis-isomers) [50], [39], [42]. Upon low irradiance, *trans-to-cis* isomerization will not yet occur. However, this irradiance can cause azobenzene molecules to rotate in their LCE matrix:

"During irradiation by linearly polarized light, a molecule enters into a photochemical reaction and changes orientation until the orientation of its absorbing oscillator becomes nearly orthogonal to the polarization of the incident radiation" [39].

Azobenzene molecules whose oscillation axes are the most parallel aligned with the light direction (and are thus most orthogonal to the polarization direction), will show the strongest response (rotation and/or trans-cis isomerization with high enough irradiance).

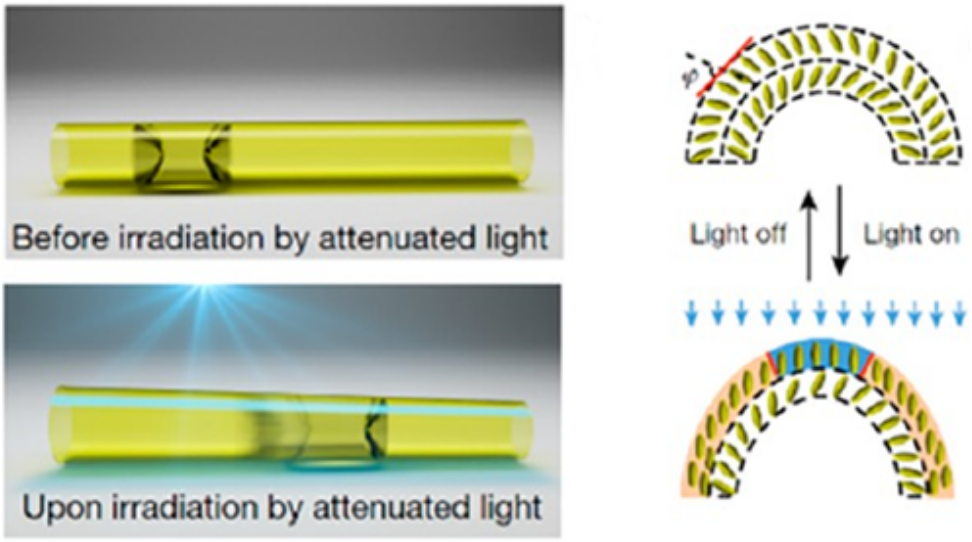

Figure 1.25: **Left:** The Weigert effect causes reorientation of the azobenzene mesogens along the direction of the incident light. As a result, the tube wall thickness decreased, while its diameter widens. **Right:** Reorientation of the azobenzene mesogens in the LCE upon blue unpolarized irradiation (copied from [49]).

The order parameter is a measure of the alignment of mesogens on the polymer backbone of the LCE. Because azobenzene molecules are a part of these mesogens, together with the liquid crystals, **azobenzene alignment is a proxy for order parameter**. A maximum order parameter of 1 means perfect parallel alignment of the mesogens with the nematic director (angle between nematic director and oscillating axis of mesogens molecule =0°). The MM10 used in this thesis has an estimated order parameter of 0.48 [51]. The order parameter can increase through more alignment, for example by straining the LCE in the nematic director direction. The LCE polymer matrix allows rotation of the mesogens only to a certain degree. When linearly polarized light is shone upon this LCE, the azobenzene molecules will rotate with the oscillating axis orthogonal to the direction of polarization as much as possible. The molecules that are best aligned, will take part in photochemical reactions and thus absorb light. This means that when there is a limitation in rotation by the LCE matrix, absorption of azobenzene molecules will be more or less effective depending on polarization direction [39]. This explains why the absorption of linearly polarized light will depend on the polarization direction to the nematic director. Absorption is not easy to measure, but instead transmittance can be measured easily. It is evident that if the absorption by the LCE increases, the transmittance will decrease and *vice versa. Thus, measuring transmittance of linearly polarized light through LCE sheets can be used as an approximation for the order parameter.* It was shown that light-responsive polymers with azobenzenes incorporated show the largest contraction when the polarization of light is parallel to the contraction direction (nematic director in LCE) [47]. The order parameter of the LCE used in this thesis will be measured in using the method described here.

Penetration depth of light in LCEs

Light might only penetrate to a certain depth into the LCE sheet. From this standpoint, a thin as possible LCE sheet is beneficial, because light penetration decreases exponentially with thickness of material [46]:

$$\delta_p = 1/\epsilon \cdot c$$

Where δ_p is the penetration depth of light in material (cm), ϵ is the molar extinction coefficient ($1/(mol{\cdot}cm)$), and c is the molar concentration of the dye in the film (mol/dm^3).

A typical polymer density is $d = 1.2g/cm^3$. It was shown in previous research that light does not penetrate far into an LCE film. Two types of LCE were tested, namely with a red (*Disperse Red 1*) and blue (*Disperse Blue 14*D) light responsive dye incorporated. Light penetration into the LCE material varied between 8-131μm. From this standpoint, it would thus be wise to keep the LCE material thickness below 80μm to achieve homogeneous illumination of the material and thus prevent inactive parts of the LCE due to light shortage.

Measured penetration depth of light in LCE			
Sample	$\epsilon(1/(M \cdot cm)$	$c(Mol/dm^3)$	δ_p (μm)
0.1% DR1 (Red)	33000	$3.8e^{-3}$	79.7
1% DR1 (Red)	33000	$3.8e^{-3}$	8.0
0.1% DB14 (Blue)	17000	$4.5e^{-3}$	130.7
0.1% DB14 (Blue)	17000	$4.5e^{-3}$	13.1

Table 1.4: Table of two types of light-responsive LCE materials with either red light responsive or blue light responsive dye molecules incorporated. The penetration depth of light into the material is calculated based on the recipes of the materials. Adapted from: [46]

The actuation response does not linearly follow the dye concentration because at higher concentrations only a thin layer of the film is actually exposed to light [46]. There are however other factors which must be taken care of to decide an optimal thickness of LCE sheet (such as LED sheet weight and irradiance).

Production of Light-responsive LCEs

The ingredients of an LCE consist of a mixture of acrylate-based monomers (that have biocompatible properties), cross-linkers, azo-dyes for light response, and a photoinitiator [40]. All these ingredients are biocompatible, and even appear to have enhancing properties for cell growth and tissue alignment [34]. It is essential that the monomers are stretched in the same direction before crosslinking and forming polymers. A standard procedure involves infiltration of a nematic mixture in a LC cell for proper alignment, and polymerization by UV irradiation [44].

Photopolymerisation

A mixture is aligned in the nematic (thread-like) phase and then UV irradiated [40]. The alignment is done by infiltration of the mixture in monodirectional aligned cells. A photoinitiator (Igracure 369) starts the photopolymerization process upon illumination, leading to formation of large polymer networks. These polymers consist of a central chain 'backbone' with liquid crystals added as sidechains (mesogens) [52]. The mesogens can be added end-on or side-on in the sidechain. The polymers are linked through the cross-linkers, forming a liquid crystalline network (LCN). Variations in ingredients can produce LCEs with differing properties. Such variations are percentage of cross-linkers in the mixture, type of monomer, and type of cross-linker [53]. LCEs can be made by hand. However, it is thought that a lot of the benefits of these materials will take place in small scale devices [32]. Therefore, experimenting is done with mechanical and computer-assisted production of LCEs to produce with a precision on small scale (currently in the range of micrometers). Photopolymerization is widely used in several photolithographic processes to produce liquid crystalline networks using moulds, masks or techniques such as Direct Laser Writing [54]. When azobenzenes are incorporated, these have to be made unresponsive to the UV-spectrum of light (390nm). A procedure produce azobenzenes sensitive to green light (530 nm) but not to UV-light (390nm) was described in [54].

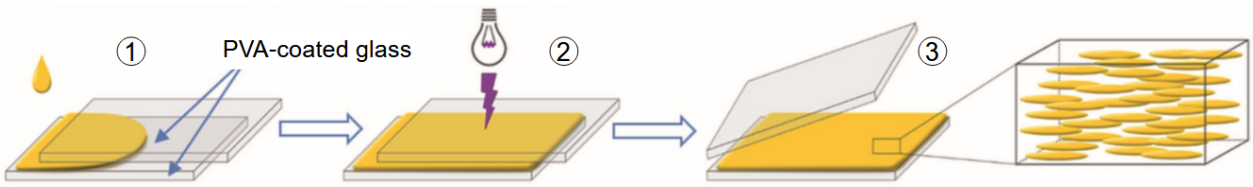

Figure 1.26: 1: Mixture infiltration at 60°C, 2: Photopolymerisation at 45 and 60°C, 3:Film removal from cell. From [34]

High-resolution 3D Direct Laser Writing (DLW)

Direct Laser Writing allows the 3D printing of an LCE mixture (containing monomers, crosslinkers, photodyes and a photoinitiator) onto a substrate. A resolution of up to 300nm for free standing structures could be produced with this technique, however some swelling in the structures was observed after printing [54].

1.4.4 MM10

Liquid crystalline elastomer *MM10* was prepared according to [40]. This LCE consists of three monomers (**1,2** (*Synthon Chemical*) and **3** (prepared as in [54])). Mesogenic monomer 1 contains a metal molecule (**Me** in fig. 1.27) which acts as a liquid crystal. Mesogenic monomer 2 contains two acrylate groups and acts as a cross-linker. Monomer 3 has light-responsive azobenzene molecules incorporated and is alternatively called *azobenzene dye* or *azo-dye*. An additional agent (Irgacure 369, *Sigma Aldrich*) was used to form the crosslinks between the monomers during UV-photopolymerisation. Hereby, the mixture of the three separate monomers is formed into a final polymer (the LCE) by the use of UV irradiation. Molecular structures of each monomer can be seen in 1.27. The composure of ingredients of MM10 can be viewed in table 1.5. MM10 contains 10mol% of the crosslinking monomer 2. This relatively low amount cross linker showed higher contraction length (19%) and faster contraction speed compared to LCEs with a higher mol% of crosslinking monomer 2 [martella reciprocal]. The azobenzene dye (monomer 3) has been tuned by changing the substituents on the the aromatic rings [54]. Hereby the absorption spectrum changed to a spectrum between 390-700nm. The absorption spectrum of azobenzene can be seen in fig. 1.27 and azobenzene is shown to be most responsive to green light (535nm), and not responsive to UV-light (thereby not interfering with the photopolymerisation process).

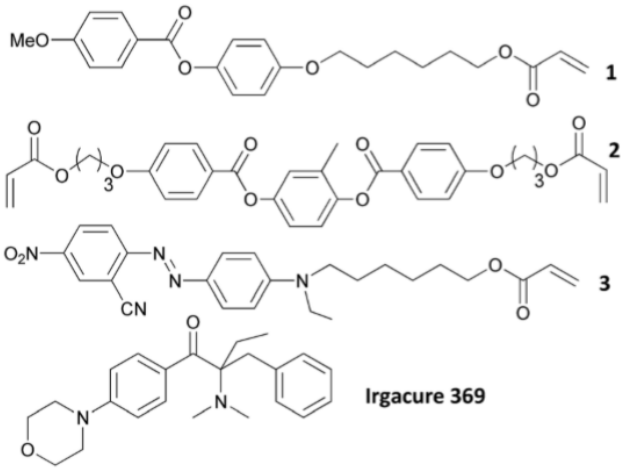

Figure 1.27: Used ingredients for the production of LCE MM10. **1:** Mesogenic monomer with an added **metal** atom (liquid crystal) **2:** Mesogenic monomer with two acrylate groups (crosslinker) **3:** Azobenzene containing monomer (azo-dye) **Irgacure 369:** curing agent for photopolymerisation process [40].

MM10 Ingredients	
MM10	**Mol%**
Monomer 1	88%
Monomer 2 (crosslinker)	10%
Monomer 3 (cont. azobenzene)	1%
Igracure 369 (photopolymerisation)	1%

Table 1.5: Ingredients and composition of the light-responsive LCE used for this thesis called MM10

Current MM10 developments for cardiac assistance

MM10 fibres were been developed with a thickness of 20μm (similar to cardiac myocytes), a length of 4mm and a width of 400μm. These fibres were irradiated with a green LED of 5 cm wide and an intensity of $1.5mW/mm^2$. It was seen that these fibres could support mouse myocardium and produce a tension of around $90mN/mm^2$ during 20 days of continuous contraction and relaxation with a frequency of 1Hz (60 bpm), without impairing the relaxation (see fig. 1.22, [1]). This experimental form of systolic support was shown to produce 40 times more tension per area than a healthy mouse myocardium (see fig. 1.28b). A concentric shape of these fibres was then produced to model an assisting device for systolic contraction of the heart. It was shown that such a concentric patch of LCE is able to generate a high amount of concentric pressure compared to human myocardium, normalized for tissue thickness [55].

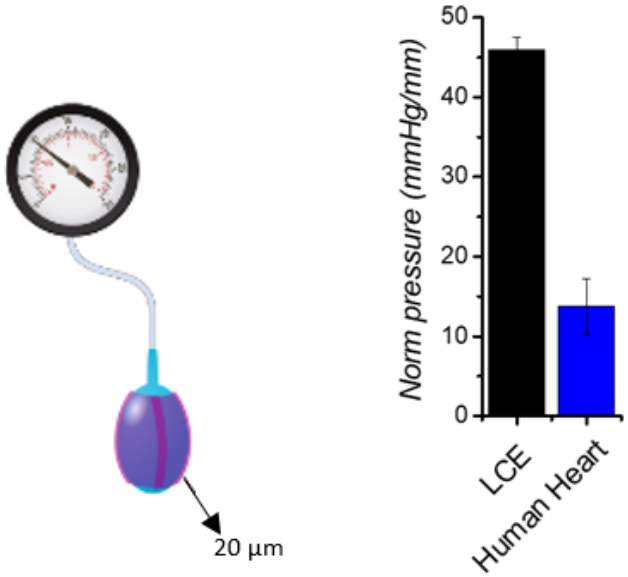

(a) (b)

Figure 1.28: Experimental setup of a concentric, 20μm thick LCE wrap surrounding a balloon with air. Stimulation of the LCE wrap results in a concentric contraction, increasing the pressure inside the balloon, which is displayed on the pressure gauge. This experiment was done to simulate LCE influence on ventricular pressure when used as cardiac assist device. The LCE wrap was able to generate a high normalized pressure compared human cardiomyocytes for the same layer thickness (pressure shown for 1mm thickness). A light stimulus of $50mW/mm^2$ with activation pattern (t_{on}/t_{off}) of 200/800 ms was used (60bpm) [55].

1.5 μLED modeling

1.5.1 μLED irradiance pattern modeling

Model overview

Normally, the irradiance produced by an non-homogeneous emitting source on a surface is obtained by integrating the source radiance $L_S(W/(m^2sr))$ over the source area A_s. Then, θ_s is the angle between the normal to the source surface element and the line between a source point and an illuminated point. Likewise, θ_d is the angle between the normal of the illuminated surface and the line between a source point. In a flat emitting surface such as μLEDs illuminating a flat surface parallel to the LED, $cos\theta_s = cos\theta_d$ and therefore the radiance L_S will be constant (which makes calculations easier). A recent study used this radiance to propose a mathematical model for LED irradiance patterns at a short distance [26]:

$$E_{x,y,h} = \frac{\phi_s K_0(h)}{A_s} \cdot \frac{(1+e^{K_x(h)(x-0.5Sx)})^{-1}}{1+e^{-K_x(h)(x+0.5Sx)}} \cdot \frac{(1+e^{K_y(h)(y-0.5Sy)})^{-1}}{1+e^{-K_y(h)(y+0.5Sy)}}$$

Where $E_{x,y,h}(mW/mm^2)$ is the irradiance on any point (x, y) on a flat surface in front of the LED at distance $h(mm)$, whereas the LED is rectangular-shaped and has constand radiance L_S (see fig. 1.30). Furthermore: ϕ_S is the radiant flux of the source (mW), A_S is the LED emitting area (mm^2) which is equal to $Sx \cdot Sy$ (LED length (Sx, mm) times width (Sy, mm)). x and y are the distances from the midpoint (0,0) of the illuminated surface (mm) in resp. the length and width direction of the LED. And:

$$K_0(h) = 1.171 \cdot e^{-0.01068(h+3.614)^2}$$

$$K_x(h) = 5.037 \cdot h^{-0.06201}$$

$$K_y(h) = 4.372 \cdot h^{-0.51}$$

This model is based on logistic functions to approximate the (very large) exact integral equation of the theory of radiation transfer [26]. Function $K_0(h)$ adjusts the height of the curve with respect to the irradiance variation within distance h, while coefficients $K_x(h)$ and $K_y(h)$ adjust the slope of the logistic functions.

This model very accurately predicts irradiance of small LED chips (with direct light emittance from the surface) on a flat surface parallel to the LED surface at short distance (see fig. 1.29). As noted before, the inverse square law does not hold here. Irradiance appears to act differently at very small distances from the LED surface (where distance d between the LED and the surface is smaller than the length or width of the LED emitting surface). This model seems to hold very well for Lambertian emitters and non-Lambertian emitters (such as an rectangular surface in μLEDs, see fig.1.29).

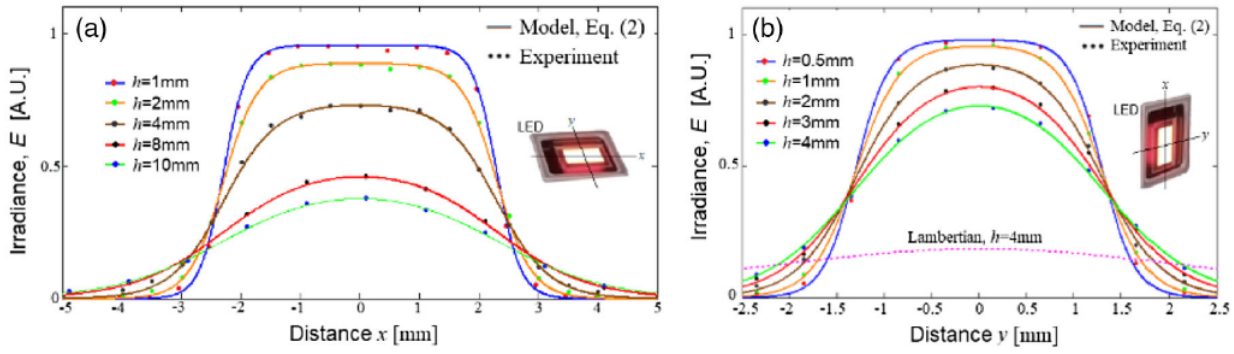

Figure 1.29: A comparison between the calculated irradiance and the measured irradiance for a non-Lambertian rectangular LED. The mathematical model as described above is used (lines, for different heights). The dots represent measurements at the corresponding heights with a radiometer. Measurements were done in x-direction (long side) and y-direction (short side) of the LED. Adapted from [26]

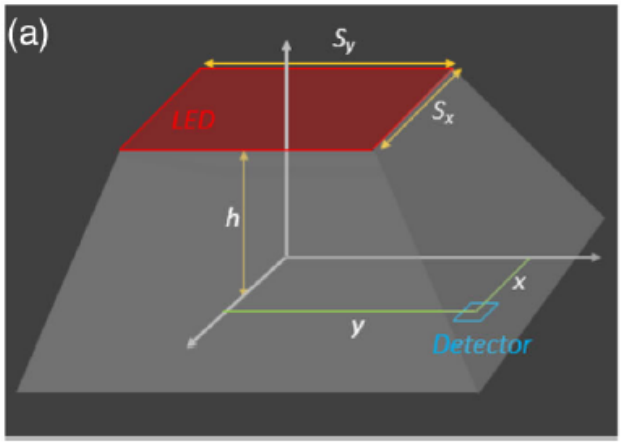

Figure 1.30: Irradiance (mW/mm^2) can be calculated on any point (x,y) on a detector (illuminated surface) parallel to the emitting LED surface. The midpoint (0,0) of the detector is equal to the midpoint of the LED surface.

Setup of parameters

We used this model to test different formations of LEDs on a surface [26]. First, the different formations are mathematically defined (fig. 1.31). Then, the model is applied to graphically show the irradiance pattern in 3D. After that, a detailed modelling is done of the irradiance pattern of multiple LEDs on a surface respectively 1mm and 0.2mm above the LED surface. A rectangular non-Lambertian μLED is tested. A 2D analysis is done to model the differences of irradiance between the x-direction (length of LED) and the y-direction (width of LED). An range of the optimal ratio of the distance d between the LED midpoints and the height h between the LED surface and the illuminated surface. Finally, a 3D simulation was done to model the irradiance pattern within this optimal $d : h$ ratio to decide which LED formation is the most effective in reaching homogenous irradiance of a flat surface. All modelling was done in Python using the mathematical model described above and the LED parameters used below (tab.1.6).

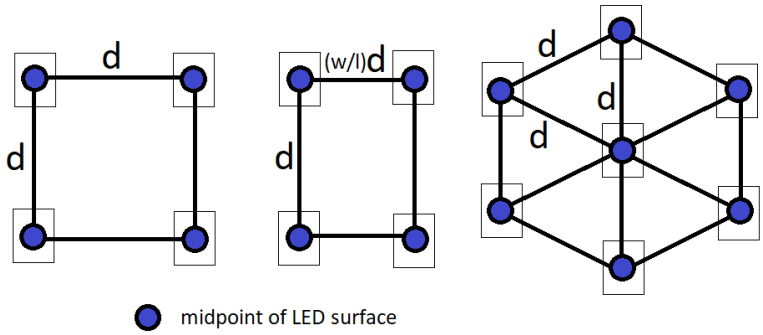

Figure 1.31: Square (left), rectangular (middle) and hexagonal (right) formation of LEDs on a unit area. d is the distance between two LED midpoints (mm). (w/l) is the ratio between the width (mm) and the length (mm) of the LED chip surface.

Length	l	$145\mu m$
Width	w	$107\mu m$
Heigth	h	$20, 200, 1000\mu m$
Radiant flux	ϕ_S	$1000mW$
Distance	d	$\geq 147\mu m$
Emitting area	A_S	$15515\mu m^2$

Table 1.6: Parameters used during modelling of LED irradiance patterns.

Irradiance pattern at $h = 1mm$ for different distances d between LED midpoints

The LEDs were modelled irradiating a surface 1mm above the LEDs. All three configurations were tested with a distance varying between $0.1 \cdot h - 1 \cdot h$ (see fig. A.1. No summation of irradiance between overlapping patterns was done. This model was done to obtain a basic feeling of the correlation between d and h.

If the sizes of the LEDs are $145x107\mu m$, the shortest distance possible between two LEDs is 145μm. The figures show at $h = 1mm$ a distance varying from $1mm$ to $0.1mm = 100\mu m$, where $d = 100\mu m$ is only a theoretical model as this distance is smaller than the physical LED dimensions.

Irradiance pattern at $h = 200\mu m$ for different distances d between LED midpoints

If we take $h = 200\mu m$ we can zoom in on the results on an even smaller scale (see fig. A.2. Note that the shortest distance between LEDs is still 145μm ($d = 0.73h$) and so we are observing here a distance ranging $145 - 200\mu m$ between the LEDs.

2D analysis of irradiance pattern for multiple LEDs

If we want to calculate the homogeneity of the irradiance at the surface at distance d from the source, we can sum up the irradiance of two intersecting LED irradiance patterns. If we do this for the configurations above, and use $h = 200\mu m$, there is overlapping irradiance between neighbouring LEDs (see fig. A.3 and A.4. Because of the non-Lambertian emission properties of our LED, we have to separately study the irradiance pattern in both x (parallel to the longest side of the LED) and y direction (parallel to the shortest side).

As shown, there is a trade-off between width of the surface illuminated area and the homogeneity. A optimum trade-off seems to be somewhere around d=0.9h and d=0.8h when measured for x-direction. Similar modelling was done in the y-direction (short side of LED surface).

3D modeling in square, rectangular and hexagonal formation

Measured in the y-direction, the optimum trade-off seems to be around between $h \leq d \leq 1.1h$. To find the optimal distance we combine the optima in x and y direction. An array of 8x8 LEDs was modeled where $0.8h \leq d \leq 1.1h$, and $h = 200\mu m$ and check the homogeneity of the irradiance at the illuminated surface. Modeling of square (fig. A.5), rectangular (fig. A.6) and hexagonal (fig. A.7) LED patterns was subsequently performed.

It can be seen that a hexagonal formation of μLEDs produces the most homogeneous irradiance of the surface compared to the square and rectangular formations. This means that the μLEDs can be placed further away from each other compared to the square or rectangular formation, and still reach a homogenous irradiance of the surface. Of course this is also beneficial regarding power consumption, as the same homogenous illumination can be reached with fewer μLEDs per unit area compared to square or rectangular formation. Most important, less (inorganic) LEDs per unit area mean less rigid parts and thus more possibilities for flexibility of the material. Also, when the interconnects weigh less per area than the LED units, an overall weight reduction will be realized in the flexible LED sheet compared to such a sheet with square/rectangular formations. All these details are very beneficial when a flexible LED sheet must be integrated and carried by a contracting LCE material.

Modelling at very close distance (LCE sheet touching the flexible LED sheet)

Theoretically, the flexible LED layer could lay adjacent to the LCE layer. In this case, the height between the μLEDs and the LCE layer is very small ($h \approx 0$). Therefore, additional simulations are done at a distance of $h = 20\mu m$. This means that a particular area of LCE will be illuminated by the light of one individual μLED only, because the emitting area of the μLED is far larger than 20μm, namely 147x107μm. Distance d between the μLEDs must thus be at least 147μm, so $d \geq \frac{145}{20}h \Rightarrow d \geq 7.25h$. We model only the hexagonal formation here with $7.25h \leq d \leq 15h$, because it was shown that this is the optimal formation to achieve irradiance homogeneity.

It can be observed that when a surface is placed 20μm above the LED panel, the irradiance becomes more homogeneous if the LEDs are placed closer together. However, this distance is limited to 145μm by the dimensions of the μLEDs. At this distance, we still observe a non-homogeneous emission pattern, with a wave like structure (see fig. A.8). 'Ridges' and 'trenches' are running parallel to the x-direction (the long side of the μLED). In the y-direction, homogeneous irradiance is then seen.

1.6 Conclusions of literature review

LCE *'MM10'* is a good candidate for our device as it is biocompatible, has fast response times, produces a large stress, and is tweakable to respond to certain wavelenghts of light. The most promising light source are μLEDs, as they are small, provide high light intensity at good efficiency, and are relatively biocompatible. Our modeling shows that the optimal formation of μLEDs is a hexagonal pattern, which provides the most homogeneous at the highest efficiency at very-nearby irradiance. A flexible μLED panel could be fabricated using flexible and stretchable interconnects, as described in a serpentine pattern. Homogeneous irradiance is important because it increases LCE efficiency of contraction. Furthermore, unwanted effects such as photobleaching are limited. Because of low penetration depth of light, multiple thin layers of LCE with layers of flexible μLEDs in between might be needed to achieve optimal performance (*'pancake structure'*).

2 Optical & Mechanical Characterization of MM10

2.1 Optical properties of MM10

2.1.1 Standard Light Microscopy

First microscopic observations were made by T. Jin (PhD, TU Delft) using a standard light microscope (Jenatech) with the samples on a white cloth background at 50,100 and 200x magnification (2.1).

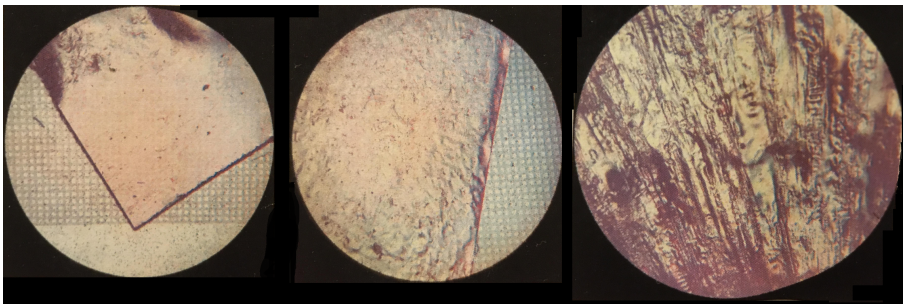

Figure 2.1: Light microscopy imaging of an MM10 strip at 50, 100 and 200x magnification (left to right).

2.1.2 Scanning Electron Microscopy (SEM) imaging

SEM-imaging was done at the TU Delft EKL Lab (*SEM Hitachi Regulus 8230*). A rectangular LCE sample was sputter-coated in gold before imaging. The sample thickness measured with the micrometer-technique was 16μm, which was confirmed by SEM measurement (also 16μm). A smooth surface was observed upon a magnification of 700x (2.2 left, 0.5kV) and a smooth curved surface with a teared edge could be observed at 250x magnification (2.2 right, 1.0kV).

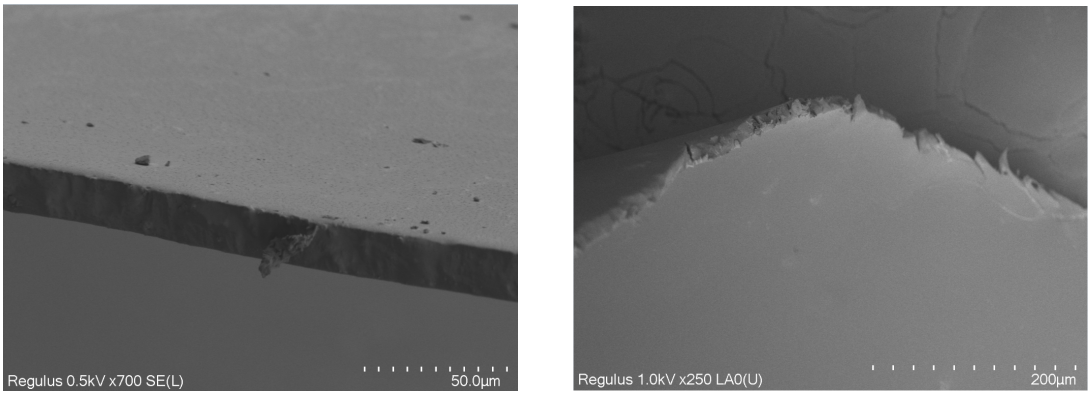

(a) (b)

Figure 2.2: SEM imaging of a MM10 LCE sheet (thickness 16μm). Left (700x): Side view with a homogeneous surface. Right (250x): Folded sheet with a teared edge. Thanks to S. Rangaswamy for processing the images.

2.1.3 Birefringence measurement

Birefringence is an optical effect present in stretched plastics such as cellophane and non-cubic crystals such as calcite [physics book], but also in LCEs [56] .

Crucial for this effect is anisotropy of the material. A light ray passing through an anisotropic material (such as LCE) is separated into an ordinary ray (**o-ray**) and an extraordinary ray (**e-ray**). Both rays experience a different refraction index when passing through the material. The rays are polarized in mutually perpendicular directions, and their speed and direction differ. The o-ray travels in the same direction as the incident light ray, but the direction of the e-ray is dependent on the orientation of the birefringent material to the incident light

ray. When a birefringent material is rotated, the extraordinary ray revolves in space around the ordinary ray [57], [58].

One special axis of an anisotropic material where no birefringence occurs is called the optic axis. When light is polarized parallel to the optic axis, it is transmitted as it would through an isotropic material, and the light is not separated into two components.

When light is polarized perpendicular to the optic axis, it is separated in to an o-ray and an e-ray, but their trajectories and direction coincide. And, there is a phase difference, because the speed by which the waves travel through the material differs (2.3).

Birefringence can be defined as:

$$Birefringence(B) = |n_e - n_o|$$

Where n_e and n_o are the refractive indices experienced by resp. the extraordinary ray and the ordinary ray. This equation holds true only if the incident light beam is not parallel to the optic axis (when parallel, there is no birefringence). Birefringence is not a constant value, but varies according to the orientation of the material to the incident light.

Relative retardation (Γ) can be defined as:

$$Retardation(\Gamma) = t_{MM10} \cdot |n_e - n_o|$$

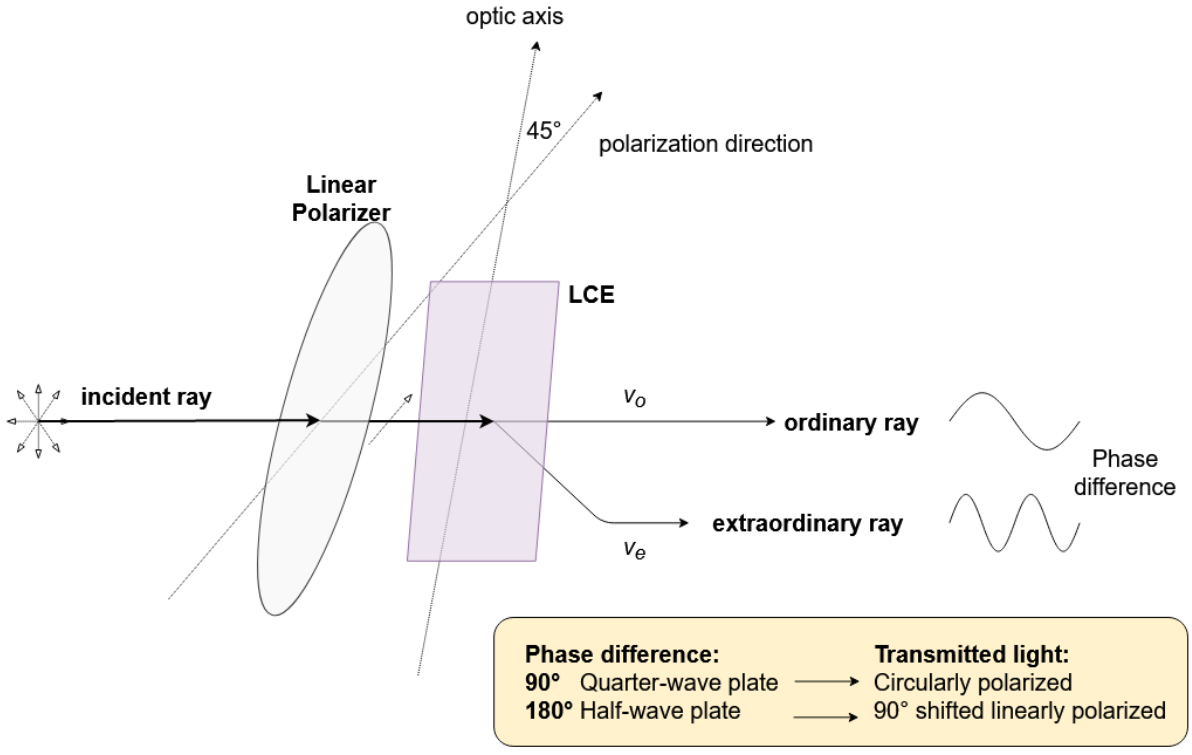

Figure 2.3: A non-polarized incident ray will pass through a linear polarizer with the polarization direction in an angle of 45° to the optic axis of the LCE. Birefringence due to LCE anisotropy will generate an ordinary and extraordinary wave with difference in wavelength and speed. This phase difference can rotate the polarization direction of the transmitted light with 90° compared to the incident light (half-wave plate), or transform the transmitted light to circularly polarized light (quarter-wave plate). Image by author of thesis.

It was observed that light transmittance through two crossed linear polarizers is possible when an MM10 sample is placed in between (see figs. 2.4, 2.5). No light will be transmitted around the LCE samples as expected, because the crossed polarizers block all the incoming light. This means that **MM10 acts as a birefringent half-wave plate**. The sample rotates the polarization direction of the incoming light with 90° before transmittance. This rotated polarized light can be transmitted through the second linear polarizer without being absorbed, so that light is visible through the crossed polarizers when an MM10 sample is placed in between. It is shown that light transmittance is maximal when the nematic director of the LCE makes an angle of 45° compared to the polarization direction (of both the polarizers, see figure 2.4). This means that the optic axis of MM10 is closely aligned with its nematic director [58].

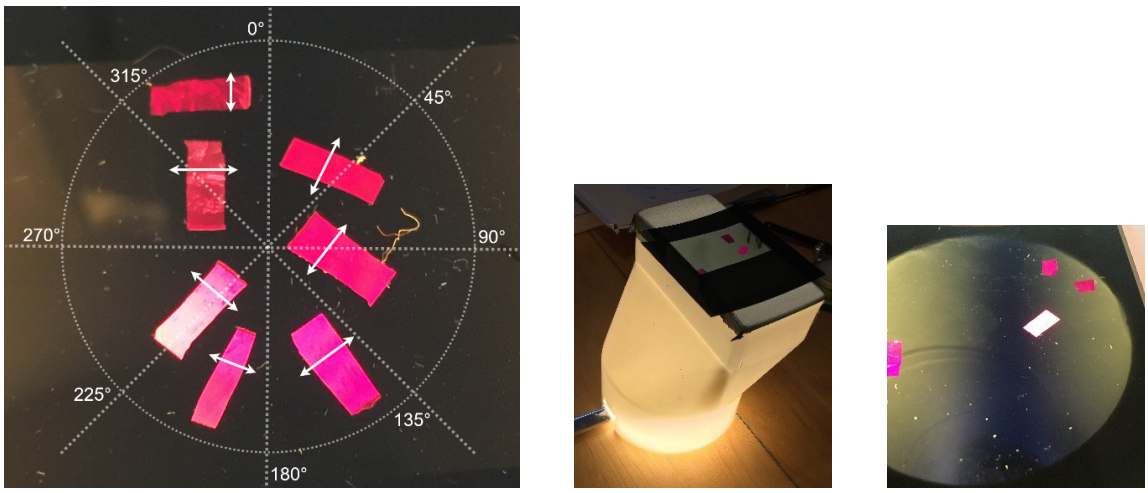

(a) (b) (c)

Figure 2.4: (a): Close-up. Most light is passed through the crossed polarizers when the nematic director (small white arrows) of the LCE has an angle of 45° with the top polarizer direction. (b): Setup for examining birefringence, consisting of a non-polarized LED-lamp, plastic tube and two crossed linear polarizers. (c): Clearly visible birefringence effects.

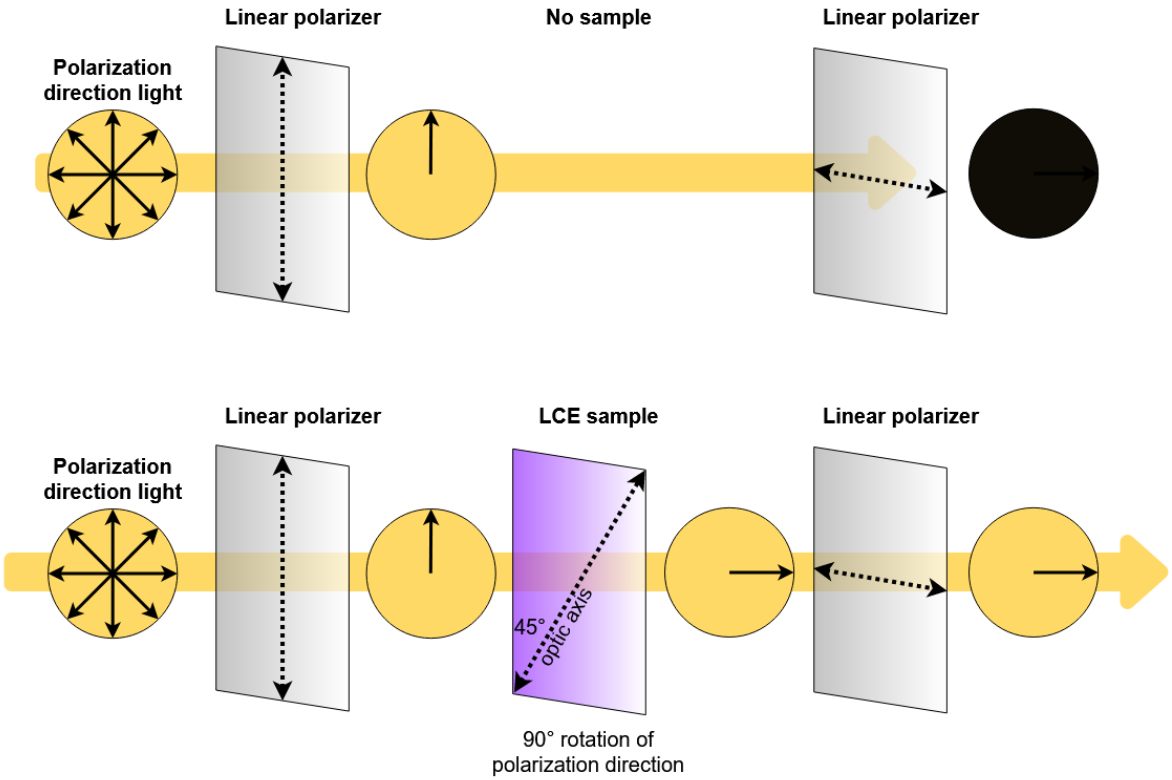

Figure 2.5: Crossed polarizers with and without LCE sample in between. No light comes through without an LCE sample. The birefringent LCE rotates the direction of incoming linearly polarized light, so that it can pass the second linear polarizer. This effect is maximal when the optic axis of the LCE sample has an angle of 45° with the polarization direction of the first polarizer. The optic axis of the LCE happens to be parallel to the nematic director. (Image by author of thesis)

Microscopic birefringence quantification

A further detailed birefringence analysis was done on two MM10 samples (LCE 1 ($26 \pm 1\mu m$) and LCE 2 ($42 \pm 1\mu m$)) at the *Signify* laboratorium in Eindhoven, the Netherlands. A polarization microscope (*Leitz Laborlux 12 Pol*) with 1942K-compensator was used. This compensation filter can determine the phase difference between o-ray and e-ray and the relative retardation (Γ) can be obtained from a table.

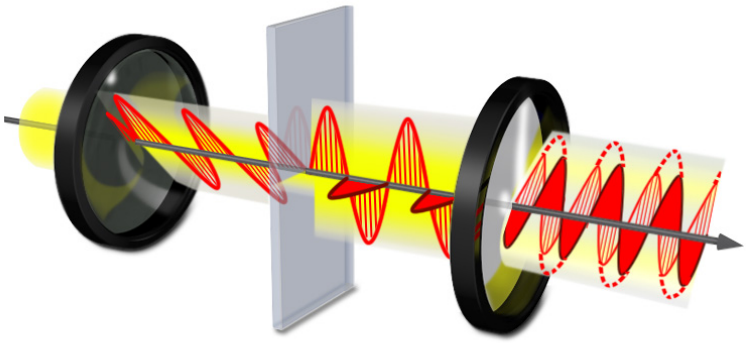

Figure 2.6: White light enters through the first polarizer, and is polarized when hitting the LCE surface. The LCE refracts the light into two separate compontents perpendicular to eachother. The light then hits the second polarizer, which only lets through light in a certain polarized direction.However, this polarized light now consists out of two rays with a phase difference. The retardation equation applies here. From [58].

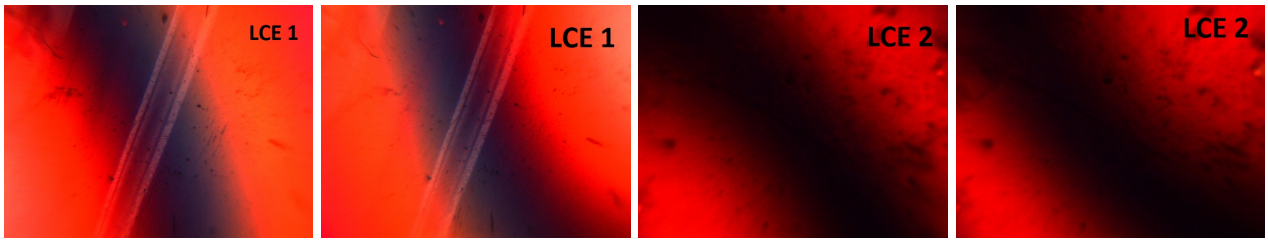

(a) (b) (c) (d)

Figure 2.7: (a) LCE 1 ($26 \pm 1 \mu m$) first half angle 9.25° (b) LCE 1 second half angle 10.5° (c) LCE 2 ($42 \pm 1 \mu m$) first half angle 9.4° (d) LCE 2 second half angle 10.2°.

LCE sample 1 showed angles of: $\Theta_1 = 9.25°$ and $\Theta_2 = 10.5°$ LCE sample 2 showed angles of: $\Theta_1 = 9.4°$ and $\Theta_2 = 10.2°$. We know that:

$$2i° = \Theta_1 + \Theta_2$$

The retardation can be approximated as:

$$\Gamma = 1.6115 \cdot 2i° + 0.4231 \cdot 2i° - 1.1402$$

We then find:

$$\Gamma_{LCE1} = 636nm$$

$$\Gamma_{LCE1} = 626nm$$

As previously mentioned we can now find the birefringence of each sample:

$$\Gamma = t_{MM10} \cdot B$$

And find $B_{LCE1} = 0.0245$ and $B_{LCE2} = 0.0149$.

These first-order wavelength differences between o-ray and e-ray correlate to the sample thickness and birefringence. When two of the three variables are known, birefringence can be read off the *Michael Levy birefringence chart*:

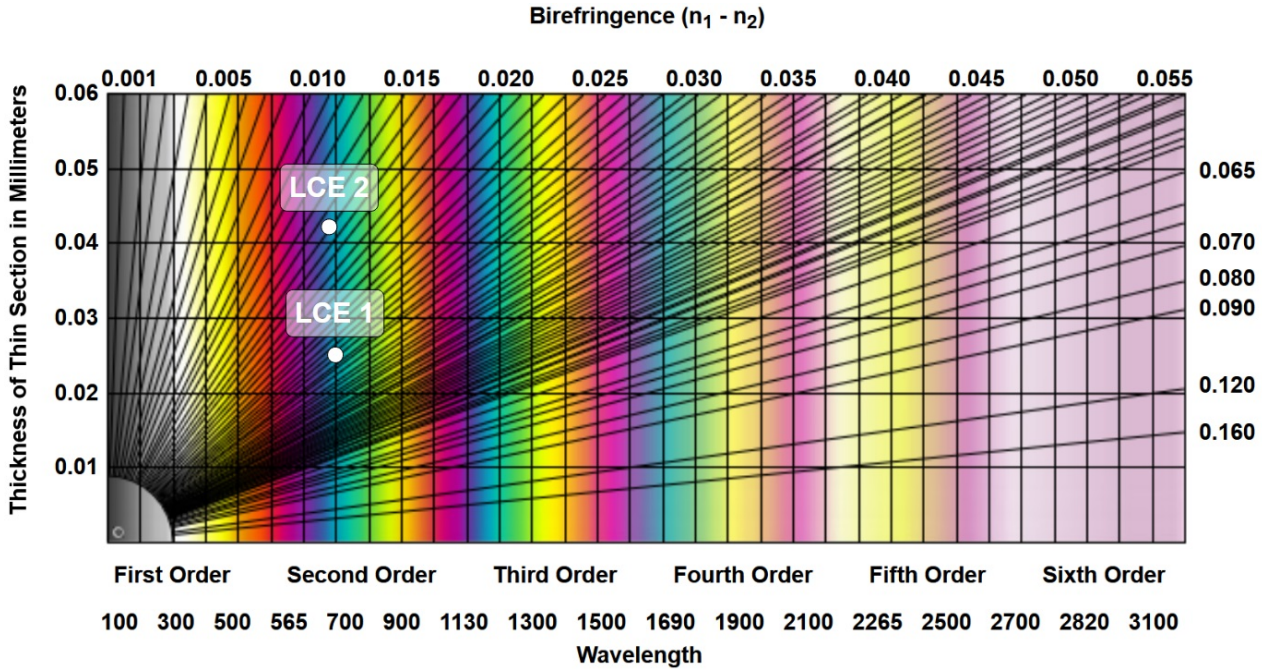

Figure 2.8: Michael Levy birefringence chart for estimating birefringence when sample thickness and wavelength difference between o-ray and e-ray are known

We find the birefringence $B_{LCE1} = 0.025$ for LCE 1 and $B_{LCE2} = 0.015$ for LCE 2, corresponding with our calculation above.

Wavelength-dependent birefringence

Reflection and transmission were measured at the *Signify* company (Eindhoven, the Netherlands) with use of a Cary 500 spectrophotometer (*Agilent/Varian*) in the wavelength range of 250-800nm, with a resolution of 1nm.

Two 20μm-thick MM10 samples were placed between two crossed polarizers, whereby the nematic director has an angle of 45° with the polarizing direction one of the polarizers. We obtain here the transmission quantified per wavelength, also called the effective anisotropy [39].

Reflection overall varied between 5-10% for both samples in the wavelength spectrum 250-800nm. In the spectrum of effective azobenzene absorption (400-600nm) the reflection is around 6%.

Transmission varied from 0-20% over the whole wavelength spectrum. A transmission higher than zero means that there is effective birefringence, whereby the MM10 sample acts as a refractor of the direction of the incoming linearly polarized light, allowing it to pass (partly) through the second polarizer, after which it can be measured as transmission. No transmission is seen below 400nm. In the effective azobenzene absorption spectrum (400-600nm), we see some transmission, though low ($< 5\%$). As expected, the transmission is the lowest where the azobenzene absorption is the highest, namely around 535nm. A transmission of $< 1\%$ is seen in this region. Above 600nm, the transmission begins to rise fast, up until around 20% in the 700-800nm spectrum. Here, the largest effect of birefringence has been made visible. Our observations are as follows:

Setup (in the 700-800nm range)	**Transmission (%)**
Crossed polarizers	0%
MM10 sample (20μm) + Crossed polarizers	20%
MM10 sample (20μm)	85%
None	100%

Table 2.1: Transmission in wavelength spectrum 700-800nm of MM10 through crossed polarizers, nematic director 45° with first polarizer.

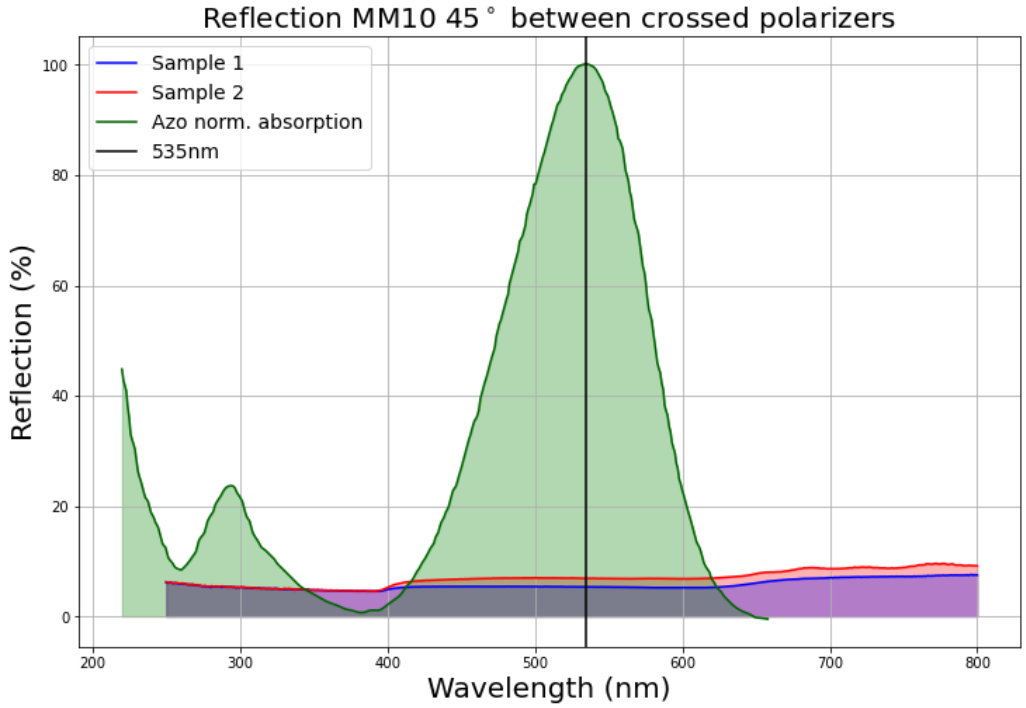

Figure 2.9: MM10 sample between crossed polarizers: Wavelength-dependent reflection

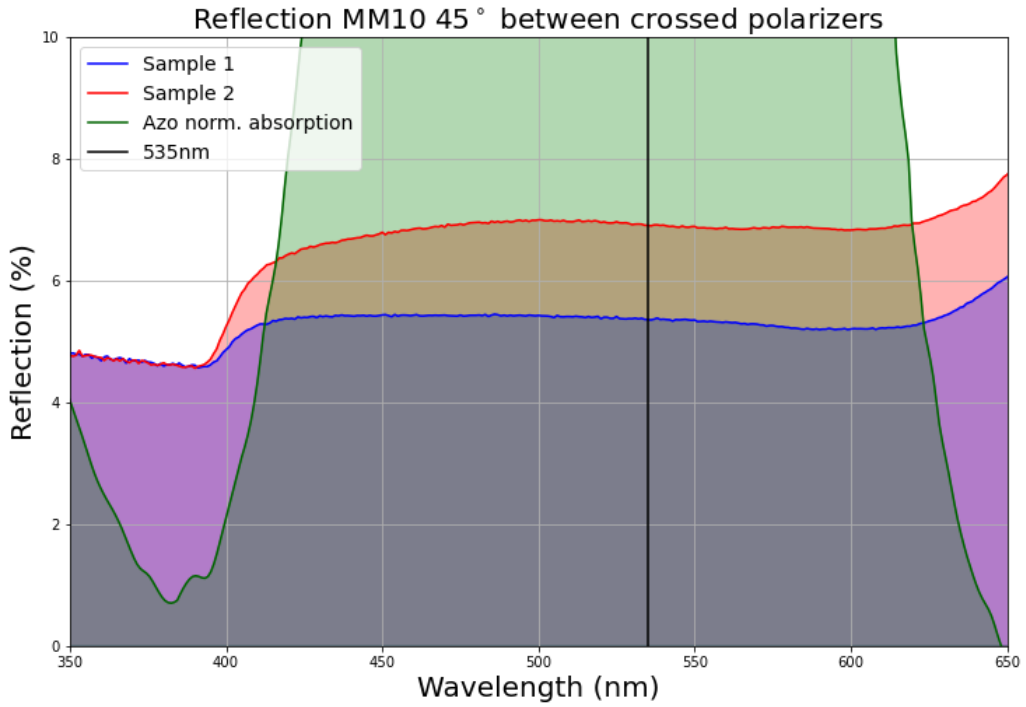

Figure 2.10: Wavelength-dependent reflection: Close-up in spectrum of azobenzene absorption

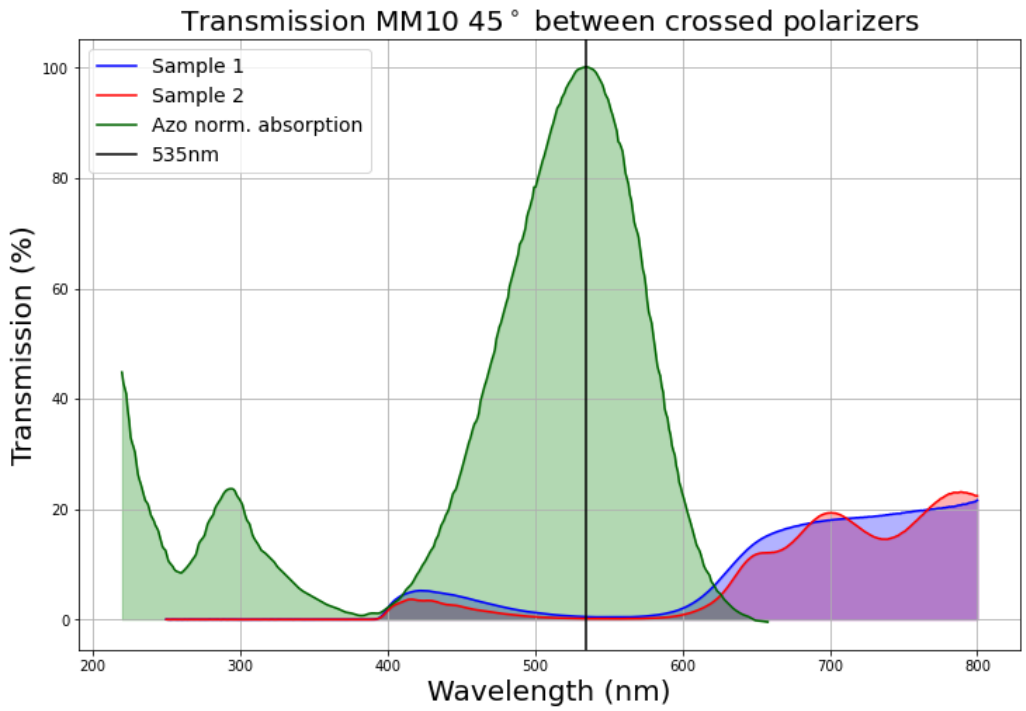

Figure 2.11: MM10 sample between crossed polarizers: Wavelength-dependent transmission (birefringence effect)

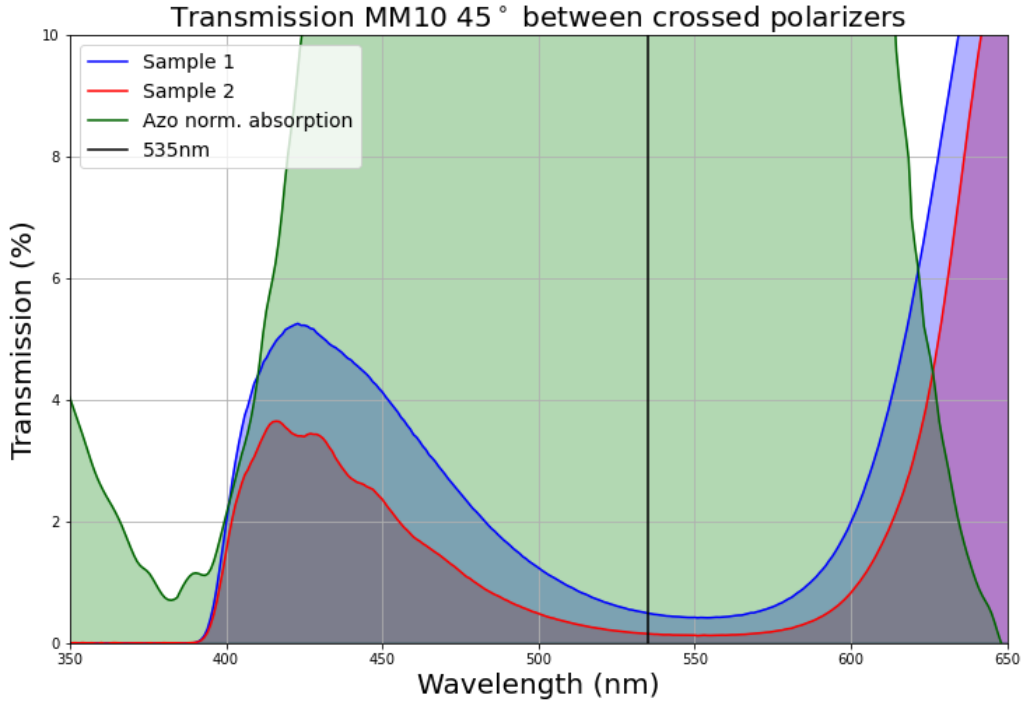

Figure 2.12: Wavelength-dependent transmission (birefringence effect) in the spectrum of azobenzene absorption

2.1.4 Reflection and transmission

Reflection of MM10

Reflection was measured at the *Signify* company (Eindhoven, the Netherlands) with use of a Cary 500 spectrophotometer (*Agilent/Varian*) in the wavelength range of 250-800nm, with a resolution of 1nm. Six samples (2x2cm) of the same production batch of MM10 were measured. It can be seen in 2.13 that the amount of reflection is the lowest in the range of around 500-600nm with minima between 581-589nm (5.09±0.18%). This

finding is beneficiary for the characteristics of azobenzene, reactive to light in the range of 420-620 nm, with a maximum sensitivity at 535nm [53]. In this range we find a mean reflection of only 5.87±0.73%. At 535nm we find a reflection of 5.45±0.21%. These results are displayed in table 2.2.

In later experiments, a green LED light (*ThorLabs M530L3*) is used to stimulate the MM10 samples. We here already present the mean reflection and transmission that occurs within the spectrum of this light: 498-541nm, where the relative intensity of the light is $> 50\%$.

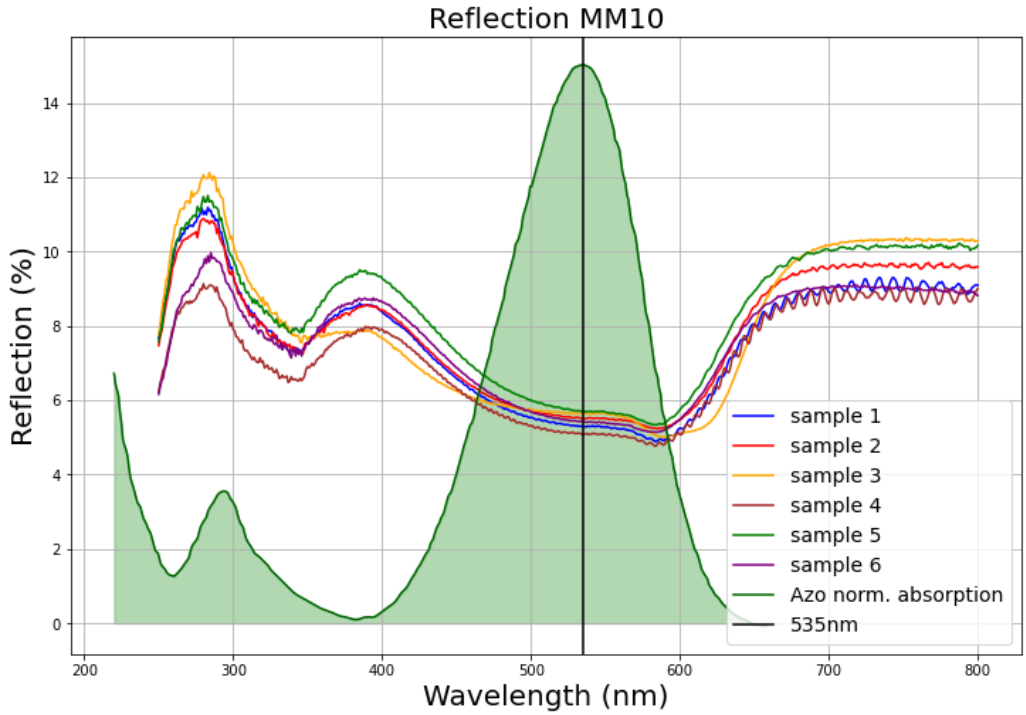

Figure 2.13: The amount of light that is reflected (%) per wavelength from 250-800nm. The azobenzene normalized absorption profile (with peak absorption at 535nm) is also displayed.

MM10 samples (n=6)	**535nm** (azo peak)	**420-620nm** (azo spectrum)	**Minimum**	**498-541nm** (LED peak)
Reflection (%)	5.45±0.21	5.87±0.73	5.09±0.18	5.53±0.22
Transmission (%)	8.13±3.36	22.41±15.34	7.35±3.10	10.57±4.63

Table 2.2: Average reflection and transmission (%) of light per wavelength spectrum. 535nm represents the absorption peak of azobenzene, with it's absorbance spectrum between 420-620nm. Minimal reflection is found between 581-589nm, and minimal tranmission between 550-551nm. Overall mean reflection and transmission are calculated between 250-800nm.

Transmission of MM10

Transmission was measured with same equipment as reflection (2.14). It was found that a peak of transmission occurs around 400nm, and that transmission is $> 80\%$ above wavelengths of 650nm. Below 300nm, there is no transmission, in other words, all light is absorbed by the LCE. For the active range of azobenzene, 420-620nm, transmission is fairly low, with a minimum of 7.35±3.1% at 550-551nm for all samples. At 535nm, the wavelength to which azobenzene is most active, the transmission was found to be 8.13±3.36%. These results are displayed in table 2.2.

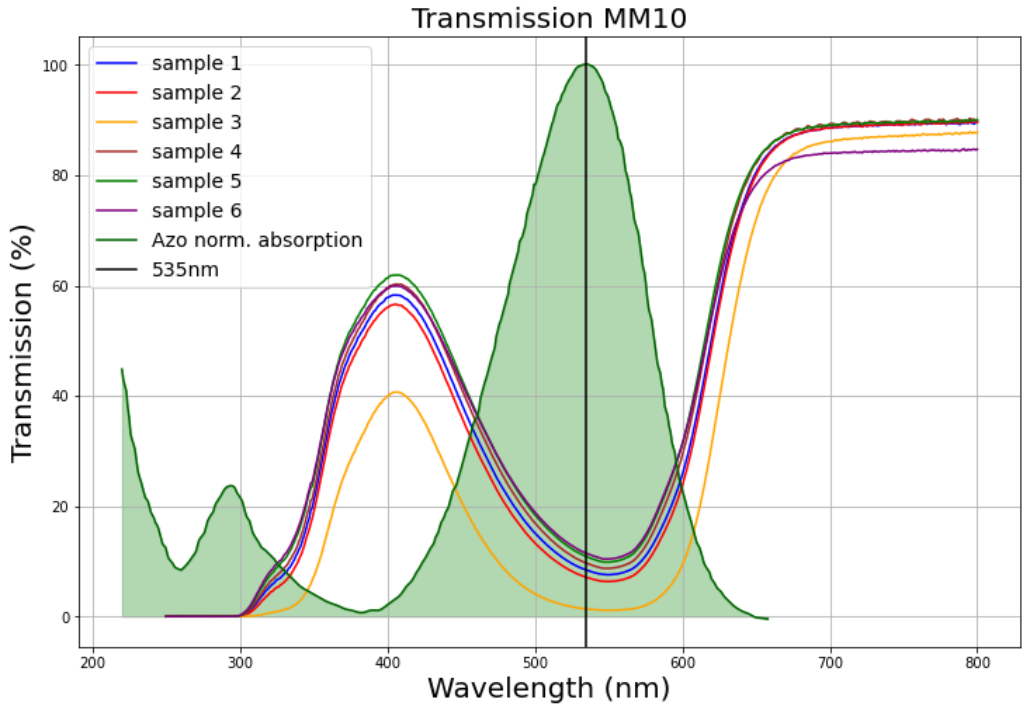

Figure 2.14: The amount of light that is transmitted (%) per wavelength from 250-800nm. The azobenzene normalized absorption profile (with peak absorption at 535nm) is also displayed.

The combined reflection, transmission characteristics are displayed in figs. 2.15 and 2.16.

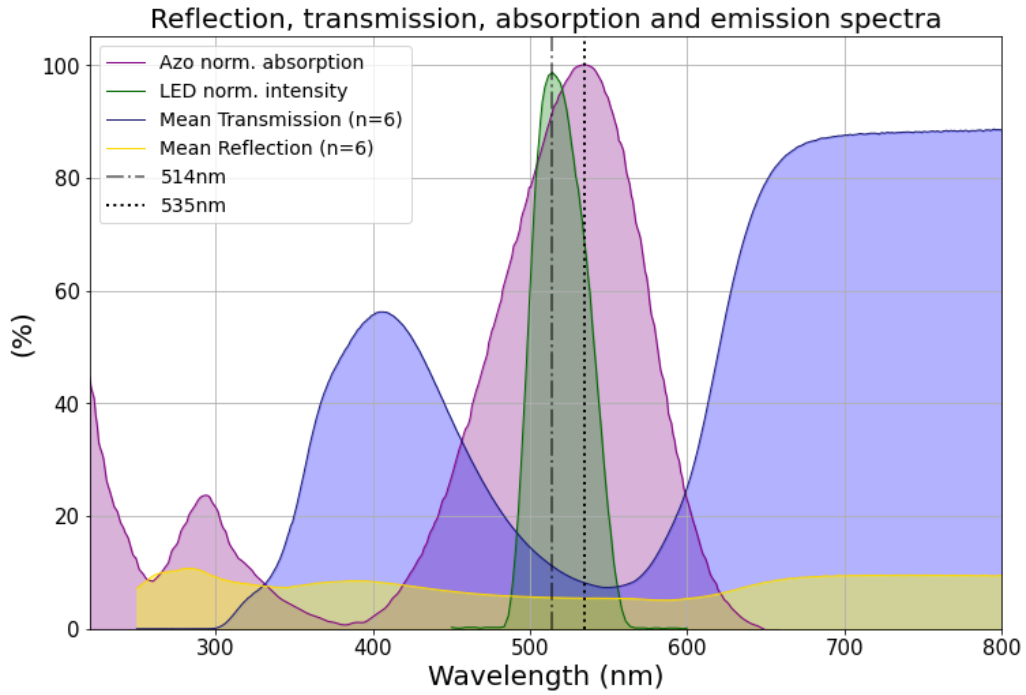

Figure 2.15: Intensity spectrum of used light source compared to absorption spectrum of azobenzene molecules, and wavelength-dependent mean reflection and transmission of MM10

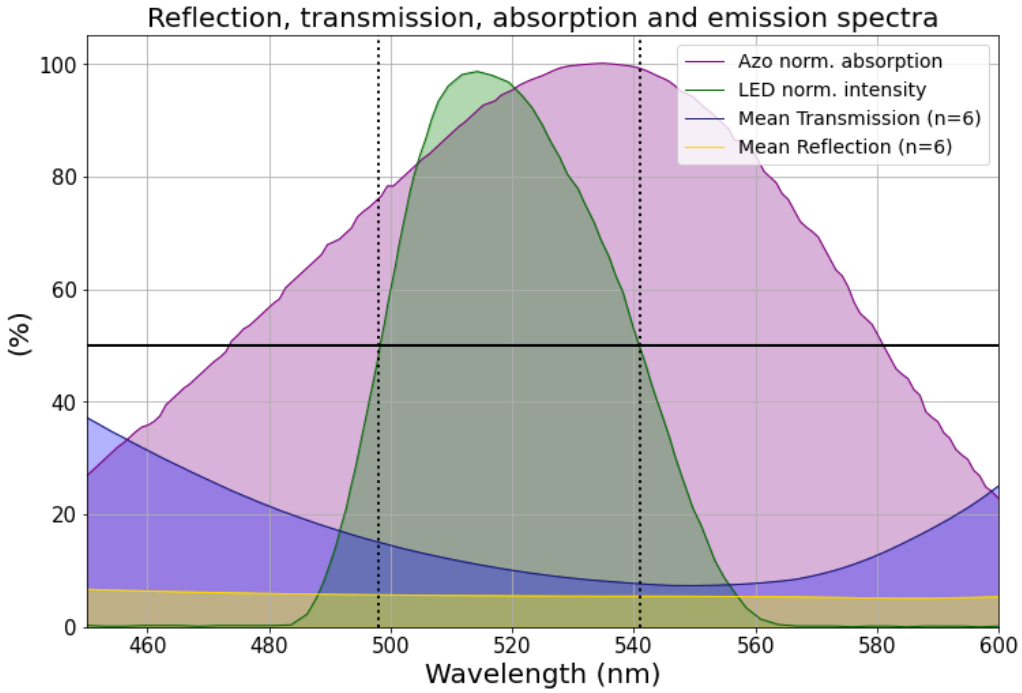

Figure 2.16: Close-up: Intensity spectrum of used light source (green LED, from manufacturer), compared to absorption spectrum of azobenzene molecules (purple), and wavelength-dependent mean reflection (yellow) and transmission (blue). The light source has a relative intensity $> 50\%$ between 498-541nm.

2.1.5 X-ray diffraction measurement (XRD)

X-ray diffraction measurement was done in the TU Delft Physics laboratory with the help of dr.Xiaohui Liu. Unfortunately, the samples proved to be to thin (around $20\mu m$) to obtain good measurements. This problem was also encounteren when trying Small-angle X-ray scattering measurement in the TU Eindhoven Physics department with the help of dr. Sean Lugger.

2.2 Passive mechanical properties of MM10

2.2.1 Sample preparation

The group of *Parmeggiani et al.* (Florence) produced all LCE samples used in this thesis. Thickness of the samples was measured with a micrometer (Mitutoyo IP65, USA) with an accuracy of 1μm.

2.2.2 Thickness measurement

The samples were cut as described before in rectangular slices varying between 30mm in length and 7-10mm width (avoiding inconsistencies in the surface of the original samples). The samples were measured by subtractive thickness measurement using a Mitutoyo micrometer (fig. 2.18). The micrometer was first calibrated by placing two silicon wafers (of exact 500μm thickness each) between the measuring surfaces. Then, the LCE samples were gently placed between the smooth sides of both wafers, and thickness was measured again. The difference between the calibration measurement and the sample measurement is the thickness of the sample. For each sample, thickness was measured on at least 5 different random points on its surface. This method proved to be superior compared to measuring directly on the surface, because the samples were not damaged at all.

(a) Measure sample (b) Cut to fit (c) Glue paper frame (d) Fix and tape sample (e) Cover second paper frame (f) Mark and store

Figure 2.17: Sample preparation for DMA testing. The samples are cut to fit the box of 3x1 cm as best as possible. Artefacts and holes in the material are avoided. A paper frame (3x3cm) is cut out with a rectangular opening in the middle (2x1.6cm) and glue is applied, The sample is glued onto the paper and fixated with tape (Scotch). A second paper frame is glued onto the tape with the sample in between.Finally, the sample is marked and stored in a dry and dark box.

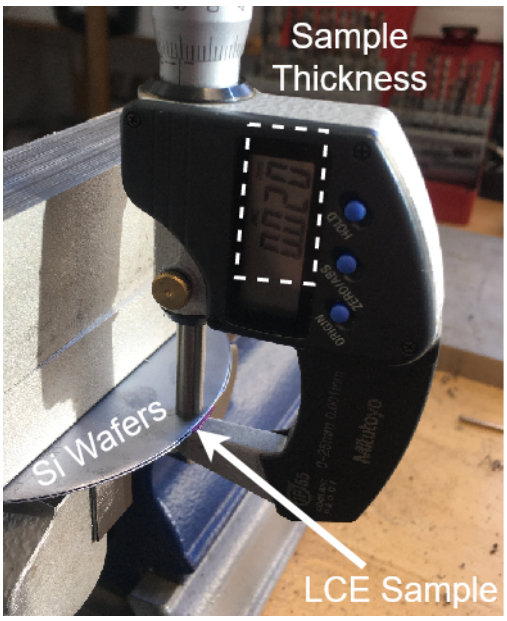

Figure 2.18: Thickness measurement of LCE sample between two 500μm-thick silicon wafers.

Table of sample thicknesses

MM10 samples	Name	Thickness (μm)	μ, σ	Used for
Batch 1	20.1	20.9±1.9	**22.93±1.47**	SS25,
	20.2	24.3±1.1		LM
	20.3	23.6±1.0		
Batch 2	1.1	25.57±0.73	**21.79±3.90**	SS37,
	1.2	25.57±0.73		SEM
	2.1	19.17±0.69		
	3.1	17.33±1.12		
	4.1	28.00±0.63		
	5.1	16.67±0.47		
	6.1	21.20±0.75		
	6.2	20.80±0.75		
Batch 3	Sample 1	19.83±0.69	**25.76±7.42**	Dyn,
	Sample 2	23.83±0.69		Bir,
	Sample 3	29.67±2.56		RT,
	Sample 4	39.33±1.11		SAXS
	Sample 5	16.17±1.07		
	Sample 6	25.70±0.96		
Batch 4	sample 1	47.27±3.25	**32.49±12.61**	LS,
	sample 2	22.82±0.72		Bir,
	sample 3	17.45±1.23		PRT
	sample 4	42.40±0.87		
Batch 5	sample 1	33.80±2.23	**34.84±10.32**	CT,
	sample 2	50.75±1.79		IR
	sample 3	29.50±0.87		
	sample 4	25.50±1.32		
	sample 5	31.58±3.38		
	sample 6	50.75±8.39		
	sample 7.1	49.58±1.50		
	sample 7.2	36.75±1.64		
	sample 6.1	25.00±1.22		
	sample 6.2	28.75±2.77		
	sample 7.1	21.33±1.43		
Batch 5 DR-1	sample 1	27.00±3.96	**21.72±3.73**	CT
	sample 2	19.08±1.38		
	sample 3	19.08±0.86		
Bands	band 2	15.67±0.75	**21.13±9.31**	CPM
	band 3	33.58±2.53		
	band 4	18.67±1.11		

Table 2.3: Thicknesses of MM10 and DR-1 MM10 LCE samples used during experiments. SS25/ SS37: Stress-strain experiments at 25 or 37°C, LM/SEM: light- or scanning electron microscopy, Bir: birefringence measurement, RT/PRT: (Polarized) reflection and transmission measurements. LS: light stimulation. CT: Contraction test. IR: Infrared measurement. CPM: Concentric pressure measurement.

2.2.3 Stress-strain measurements

Stress-strain measurement at 25°*C*

20μm-thick samples were used for stress-strain measurements. These were performed on a Dynamical Mechanical Analysis test bench (*DMA Q800*). The samples were fixed between two clamps with a moment of 0.7Nm and tests were performed in daylight at room temperature (±25°C). Strain rate and total displacement were determined by trial-and-error. After testing at a strain rate of 100μm/min with a displacement of 2000μm (sample 20.1 run 1) and a strain rate of 1000μm/min with a displacement of 4000μm (sample 20.2 run 1, which resulted in a break), a constant strain rate of 400μm/min (2.5%/min) with a displacement of 2000μm (112.5% of original length) was applied on sample 20.1 (run 2) and sample 20.3 (run 1-3). This occurred in a break of sample 20.1 in run 2 (see fig. 2.19).

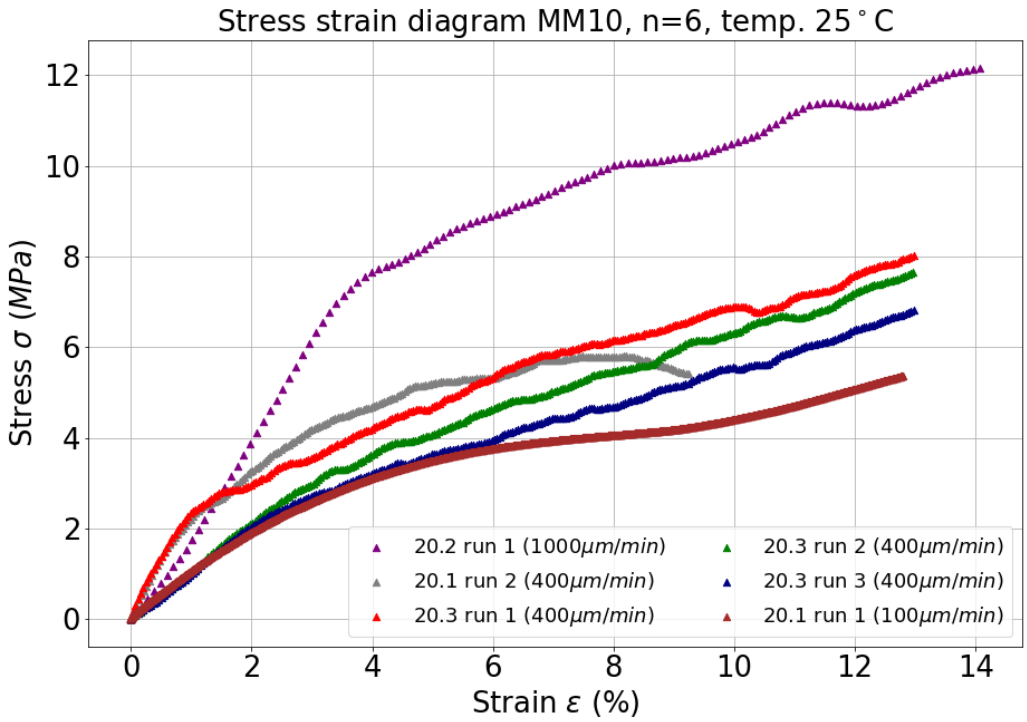

Figure 2.19: Stress-strain performance of LCE samples of a 20μm batch developed by *Ferrantini et al.* . Samples were tested on a DMA Q800 machine at 25°C daylight conditions with a strain rate between 0.625-6.25%/min and a total elongation between 12.5-25%. * Sample 20.3 did not break after three runs in of stress-strain testing, whereas sample 20.1 and 20.2 broke at resp. run 2 and run 1.

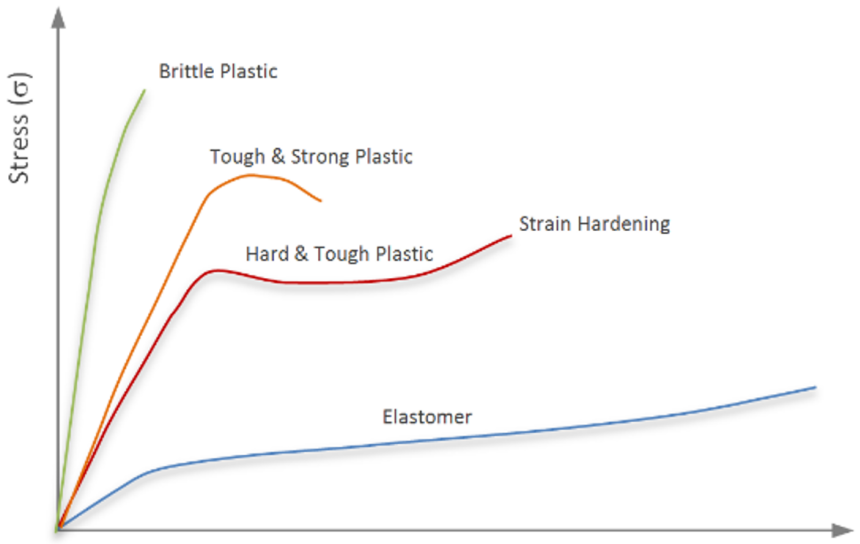

Figure 2.20: Stress-strain diagram of different types of plastics. MM10 is believed to be an elastomer. [59]

The stress-strain diagram shows behaviour of elastomer material (fig. 2.19). Samples 20.1 and 20.3 perform relatively similar, whereas sample 20.2 endures a higher displacement and stress before break. This difference can be attributable to the fact that sample 20.2 was exposed to a faster strain rate (1000μm/min vs. 400μm/min) and larger total displacement (4000μm vs 2000μm) than the other samples. Unfortunately, this sample then broke and could not be tested again (fig.2.21). Run 1 of sample 20.1 was done under a slower strain rate (100μm/min). This resulted in a lower stress exposure than when the sample was tested under a strain rate of 400μm/min (run 2).

(a) Strained (b) Formation of tear (c) Sample break

Figure 2.21: MM10 Stress-strain testing on DMA. (a) Sample strained at maximum strain (2000μm). (b) Formation of a rupture (incorrect break) during strain (green circle). (c) Correct sample break.

Young's Modulus was calculated in the area from 0.1 to 2% strain (tab.2.4). In this range a linear behavior was seen for all samples. Young's Modulus was also calculated for the 4-6% strain range. In this range a similar linear function was seen between samples, however less steep than in the 0.1-2% range. This behaviour is common for elastomer materials, where non-linear stress-strain behavior is seen. Tensile stress and elongation at break were also calculated.

The tensile strength is the stress at rupture and is calculated as [60]:

$$T_s = F_{break}/A_{cross}$$

Where T_s is the tensile strength (Pa), F_{break} the force at rupture (N) and and A_{cross} is the cross-sectional area of the unstrained specimen, in mm^2 (as in table 2.4). The amount of elongation of the LCE sample is calculated as [60]:

$$E = 100(L - L_0)/L_0$$

Where E is the elongation (in %), L is the observed distance between bench marks on the extended specimen (mm), and L_0 is the original distance between the bench marks (mm). The Young's modulus can then be derived as:

$$E_Y = \sigma/\epsilon = (F/A_{cross})/(\Delta L/L_0)$$

Where E_Y is the Young's Modulus (Pa), σ is the stress (N/mm^2) and ϵ is the ratio of elongation.

Sample MM10 (25°C)	**20.1**	**20.2**	**20.3**	μ, σ
Cross. Area, mm^2	0.21	0.24	0.24	0.23±0.01
Young's modulus, $0.1 < \sigma < 2\%$, (MPa)	95.41 (run 1) 157.26 (run 2)	207.14	140.68 (run 1) 109.84 (run 2) 105.41 (run 3)	135.96±38.30
Young's modulus, $4 < \sigma < 6\%$, (MPa)	33.40 (run 1) 32.61 (run 2)	64.90	58.91 (run 1) 51.91 (run 2) 38.04 (run 3)	46.63±12.64
Max. Tensile strength, (MPa)	>5.37 (run 1) 5.80 (run 2)	12.16	>8.03 (run 1) >7.66 (run 2) >6.83 (run 3)	>7.64±2.23
Elongation at break (%)	>11.94 (run 1) 7.09 (run 2)	13.85	>11.58 (run 1) >11.74 (run 2) >11.60 (run 3)	>11.30±2.24

Table 2.4: DMA test results of 3 MM10 samples. Young's moduli were calculated in two ranges in the stress/strain cycle, namely from 0.1-2% strain and 4-6% strain to describe this elastomeric material. Maximum tensile strength (at sample break) and elongation at break were calculated as if sample 20.3 break at the end of the tests (it stayed intact, while sample 20.1 and 20.2 broke).

These results are in a similar range of values compared to previous research where a Young's modulus of 60MPa, a maximum tensile stress of 7.4Mpa and an elongation at break of 20.33% were found at a temperature of 30°C (a higher temperature tends to increase elongation at break and lower Young's Modulus). Another study produced azobenzene-containing LCEs with a Young's modulus of 96±19MPa and a maximum tensile strength of ±20Mpa [41].

Stress-strain measurement at 37°C

To examine MM10 behavior at human body temperature, 20μm-thick MM10 samples were tested in the same manner but at 37°C (see fig. 2.22).

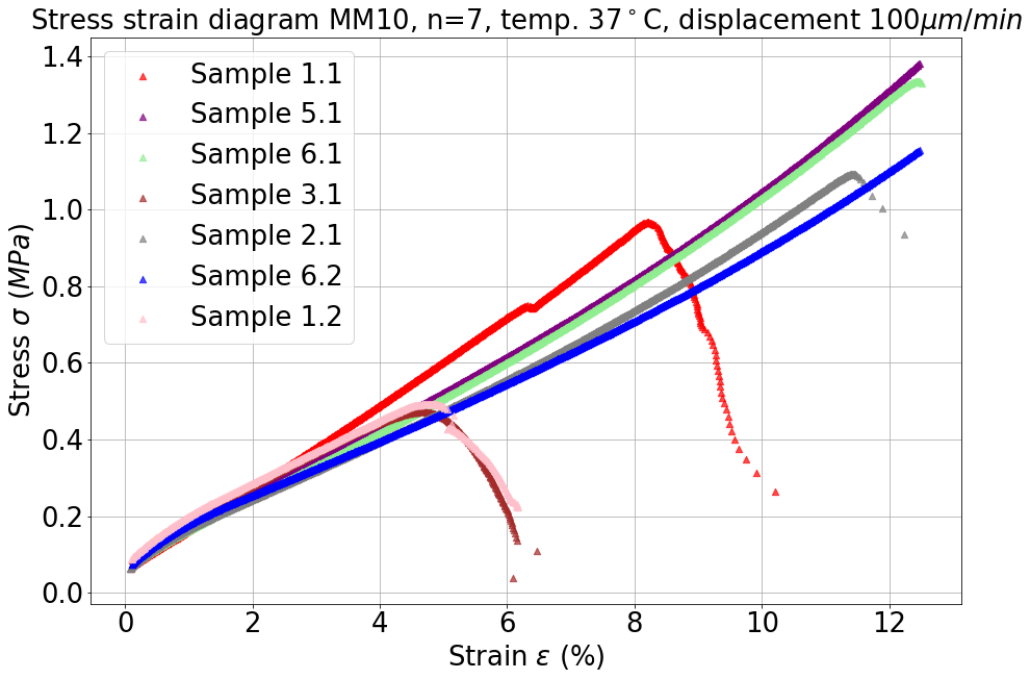

Figure 2.22: Stress-strain diagrams of seven tested LCE strips. Average sample thickness was 20μm. Tests were conducted in a dark environment at a temperature of 37°C, representing human body temperature. Strain was applied until samples were elongated to 112.5% of their initial length (16mm).

Three samples broke at a strain below 10%. Most likely, this is caused by tiny tears in the sample (fig. 2.22). The exact mode of failure could not be observed in this experiment as a result of the furnace covering the samples.

Upon closer inspection, a linear trend can be observed in all stress strain curves in the strain range 0.1-1%. These results and the linear approximation formulas for each sample can be seen in fig. 2.23 and table 2.5.

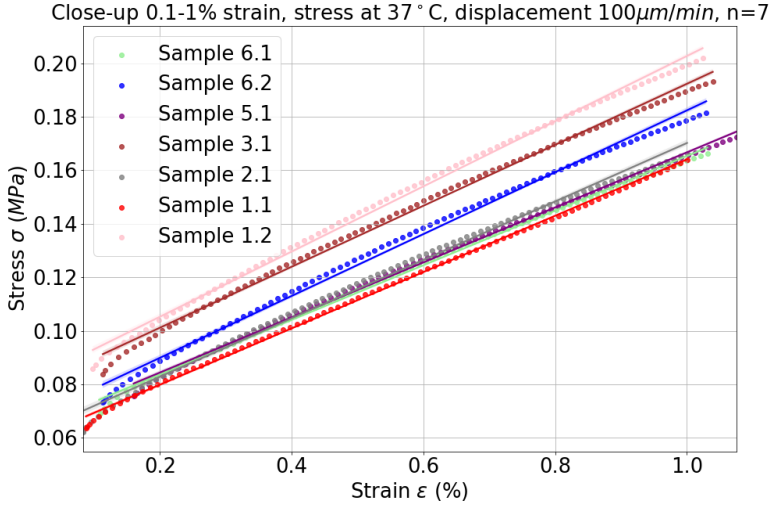

Figure 2.23: Close-up of the results in figure 1 for the strain range 0.1-1%. Linear approximations can be found for each tested sample.

Sample MM10	Linear approximation [0.1-1%] strain
Sample 1.1	$0.10x + 0.06$
Sample 1.2	$0.12x + 0.08$
Sample 2.1	$0.11x + 0.06$
Sample 3.1	$0.11x + 0.08$
Sample 5.1	$0.11x + 0.06$
Sample 6.1	$0.10x + 0.06$
Sample 6.2	$0.12x + 0.07$

Table 2.5: Linear approximation functions as obtained from figure 2.23.

Combining these linear functions, we can approximate the behavior of MM10 at $37°C$ between 0.1-1% strain and stress as:

$$\sigma = 0.11 \cdot \epsilon + 0.07$$

Where σ is stress (MPa) and ϵ the strain (% of original length).

For each sample, cross-section, Young's moduli, tensile strength and maximum elongation were calculated as described in the first batch testing procedure. These results are presented in table 2.6.

Sample MM10 (37°C)	**1.1**	**1.2**	**2.1**	**3.1**	**5.1**	**6.1**	**6.2**	μ, σ
Cross. Area, mm^2	0.20	0.18	0.19	0.14	0.12	0.17	0.15	0.16±0.03
Young's modulus, $0.1 < \sigma < 2\%$, (MPa)	10.90	10.51	9.48	10.36	9.93	9.56	9.65	10.05±0.50
Young's modulus, $4 < \sigma < 6\%$, (MPa)	11.47	-	8.12	-	9.22	9.18	7.55	9.11±1.34
Max. tensile str., (MPa),	0.97	0.49	1.09	0.47	1.38	1.33	1.15	0.99±0.34
Elongation at break, (%),	8.14	4.37	11.32	4.25	12.06	11.71	11.60	9.07±3.24

Table 2.6: Results of stress-strain tests of MM10 LCE samples (batch 2) with a thickness of $\pm 20\mu m$. Samples were tested at $37°C$ in darkness.

Comparison of MM10 properties between 25°C and 37°C

Sample MM10	**25°C** (n=6)	**37°C** (n=7)	Change (%)
Cross. Area, mm^2	0.23±0.01	0.16±0.03	-30.43
Young's modulus, $0.1 < \sigma < 2\%$	135.96±38.30	10.05±0.50	-92.61
Young's modulus, $4 < \sigma < 6\%$	46.63±12.64	9.11±1.34	-80.46
Max. tensile str. (MPa)	>7.64±2.23	0.99±0.34	-87.04
Elongation at break (%)	>11.30±2.24	9.07±3.24	-19

Table 2.7: Comparison of stress-strain tests of MM10 samples at 25° (daylight) and 37° (darkness).

It can be seen that there are vast differences between the test results of the LCE samples with different temperatures and light conditions (table 2.7). Samples tested in daylight at 25°C show a >10x higher Young's modulus from 0.1-2% strain and a >4x higher modulus from 4-6% strain. In other words, the samples tested at 25°C are far stiffer and can withstand larger pulling forces before collapse than those at 37°C. This effect was seen in all samples tested at 25°C compared to those at 37°C, independent of the strain rate. The two batches of samples are identical in recipe and mean thickness. The effect can thus only be explained by the large difference in temperature and/or the light conditions (darkness vs. daylight). It is assumed that daylight cannot elicit a contraction of the LCE, because the incorporated azobenzenes are unresponsive most of the wavelengths of the daylight spectrum. Also, the intensity of this light is far too low ($\ll 0.2mW/mm^2$). Therefore, daylight cannot cause a photomechanic or thermomechanic effect in LCEs . The differences in Young's moduli are thus caused by the temperature differences. The heating of the sample can make the LCE more elastic, causing it to elongate with less pulling force than in colder conditions. This effect is widely recognized in polymers.

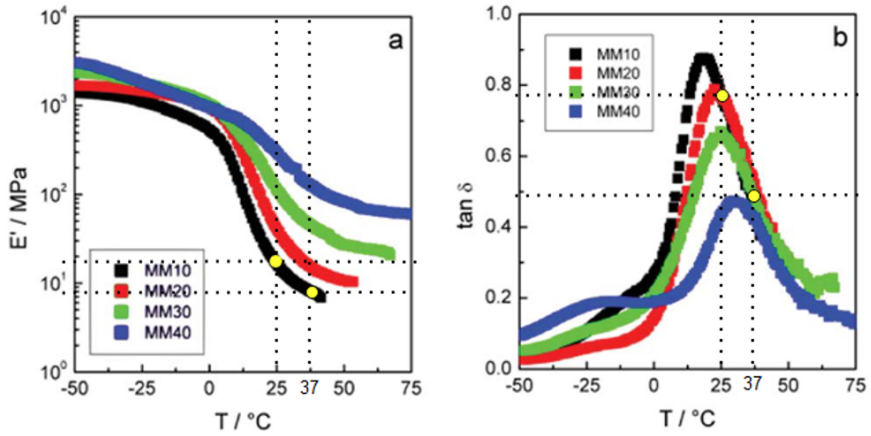

Figure 2.24: Trends of E' and $tan(\delta)$ for MM10 (black lines) analyzed with the pulling direction parallel to the nematic director of the LCE (adapted and edited from [40]

A similar LCE (MM10) was tested in 2017 by *Martella et al* [40]. and showed a fast decline in Young's moduli with a temperature increase from 0-37.5°C (see fig. 2.24). Although the Young's modulus found in our experiment was fairly similar to the findings by Martella et al. at 37°C (E≈10Mpa), at 25°C our Young modulus was far higher (E≈100MPa vs. E≈20MPa). The highest Young modulus found by *Martella et al.* (for MM10) was at -25°C, namely 1000 MPa. The glass transition temperature (T_g) is found to be somewhere between 5-10°C. This would mean that our samples tested at 25 and 37°C have already passed the T_g in both cases.

Mathematical modeling of stress-strain behavior of LCE

We try fitting our findings of MM10 (side-chain LCE) to an earlier described model for main chain LCEs:

$$\frac{F}{A_0} = \mu_1 \left(\frac{\lambda_t}{1+2Q} - \frac{1}{(1-Q)\lambda_t^2} \right) + \dot{\lambda}\mu_2 \left(\lambda_t^2 - \frac{1}{2\lambda_t^4} \right)$$

Parameter	**Name**	**Unit**	**Calculated as**
F	Tensile force	N	
A_0	Cross-sectional Area	mm^2	
Q	Order parameter	set as 0.50	
λ	Deformation along tensile axis	mm	$\Delta L/L_0$
ΔL	Elongation	mm	
L_0	Initial distance betw. clamps	mm	
$\dot{\lambda}$	Deformation rate	mm/s	$\dot{u}/L_0$
$\dot{u}$	Strain rate	mm/s	
μ_1, μ_2	Two parameters to be fitted		

We first plot the left part of the function as:

$$H(t) = F(t)/A_0$$

Then the right part of the function (G) is plotted (as dotted lines in fig. 2.25, 2.26):

$$G(t) = \mu_1 \left(\frac{\lambda_t}{1+2Q} - \frac{1}{(1-Q)\lambda_t^2} \right) + \dot{\lambda}\mu_2 \left(\lambda_t^2 - \frac{1}{2\lambda_t^4} \right)$$

Where optimal values of μ_1 and μ_2 are found by curve fitting in Python. These values and the curves are displayed in table **??**. The deformation rate $\dot{\lambda}$ is constant over time and the order parameter Q is constant (Q was first estimated 0.48 [44] but was later measured 0.50). A very good overlap of our experiments and the model is found (see fig. 2.25).

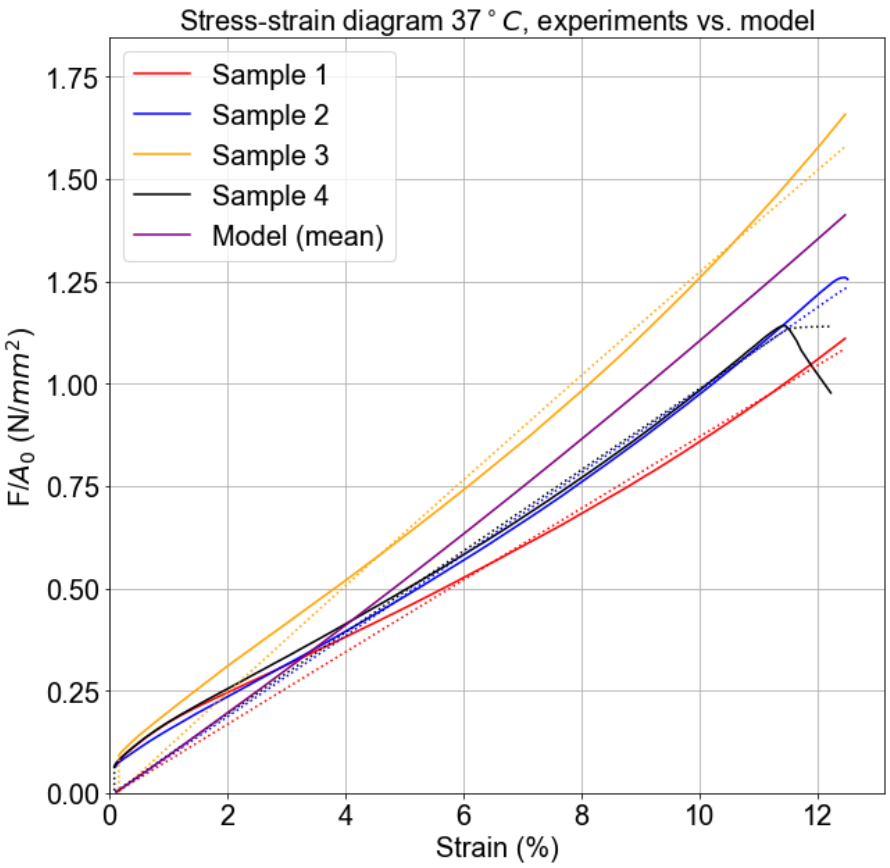

Figure 2.25: Until break, $37°C$, strain rate $\dot{u} = 100\mu m/min$ Dotted lines: Model (per sample).

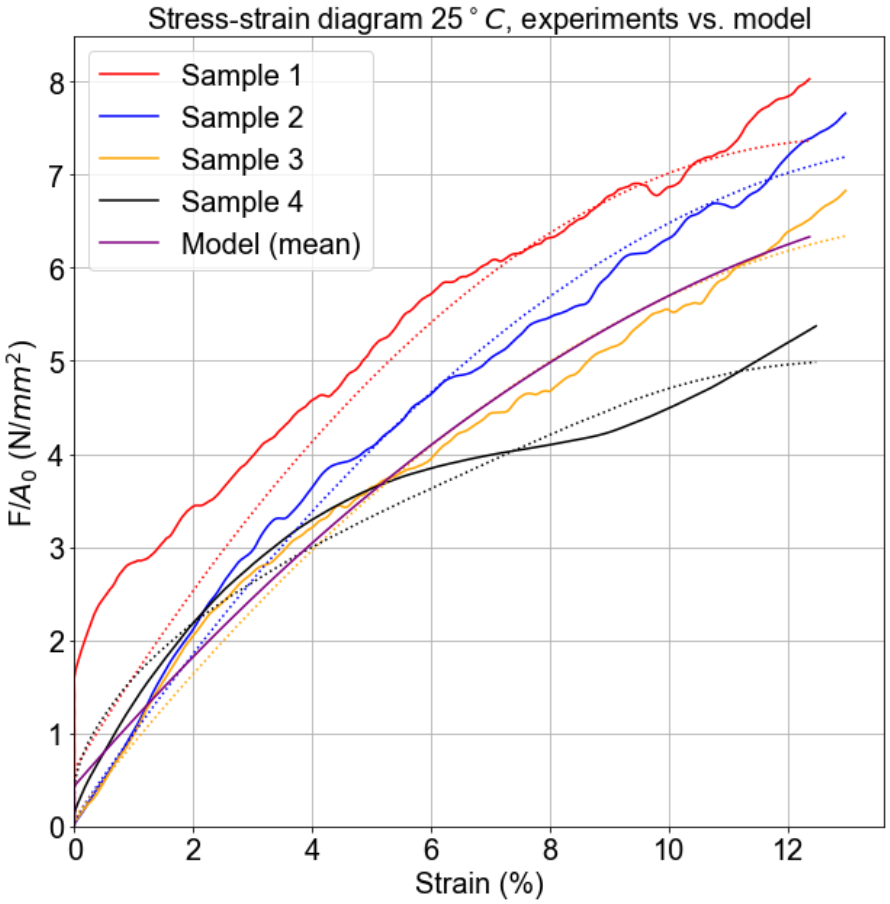

Figure 2.26: Until break, $25°C$, strain rate $\dot{u} = 100 - 400\mu m/min$ Dotted lines: Model (per sample).

Until break		μ_1	μ_2
$\dot{u} = 100\mu m/min$	n=4 (37°C)	0.0021 ± 0.0004	0.0011 ± 0.0022
$\dot{u} = 100 - 400\mu m/min$	n=4 (25°C)	$0.0661 \pm 0,0304$	$-0,1247 \pm 0,0603$

As such, we find the approximations for $25°C$:

$$G(t) = 0.0021\left(\frac{\lambda_t}{1+2Q} - \frac{1}{(1-Q)\lambda_t^2}\right) + 0.0011\dot{\lambda}\left(\lambda_t^2 - \frac{1}{2\lambda_t^4}\right)$$

And $37°C$:

$$G(t) = 0.0661\left(\frac{\lambda_t}{1+2Q} - \frac{1}{(1-Q)\lambda_t^2}\right) - 0.1247\dot{\lambda}\left(\lambda_t^2 - \frac{1}{2\lambda_t^4}\right)$$

2.3 Dynamical properties of MM10

Stiffness and damping were measured in the range of 1-3Hz (representing a 60-180bpm heart rate). A constant (10mN) and a sinusoidal force (10mN) were applied, so that the modulus can be described as an in-phase component (storage modulus E', MPa) and an out-of-phase component (loss modulus E", MPa). The ratio of the loss to the storage is the tan delta ($tan(\delta)$) and describes the energy dissipation of the material, also known as damping:

$$tan(\delta) = \frac{E"}{E'}$$

The storage modulus E' describes the samples' elastic behavior. This modulus, and so tan delta, vary with temperature and frequency. Higher elasticity (high E') generates lower damping (low tan delta) and vice versa. When frequency increases, usually the storage modulus will increase, because of a decreased recovery time for the material.

Temperature-dependent dynamical behavior of MM10

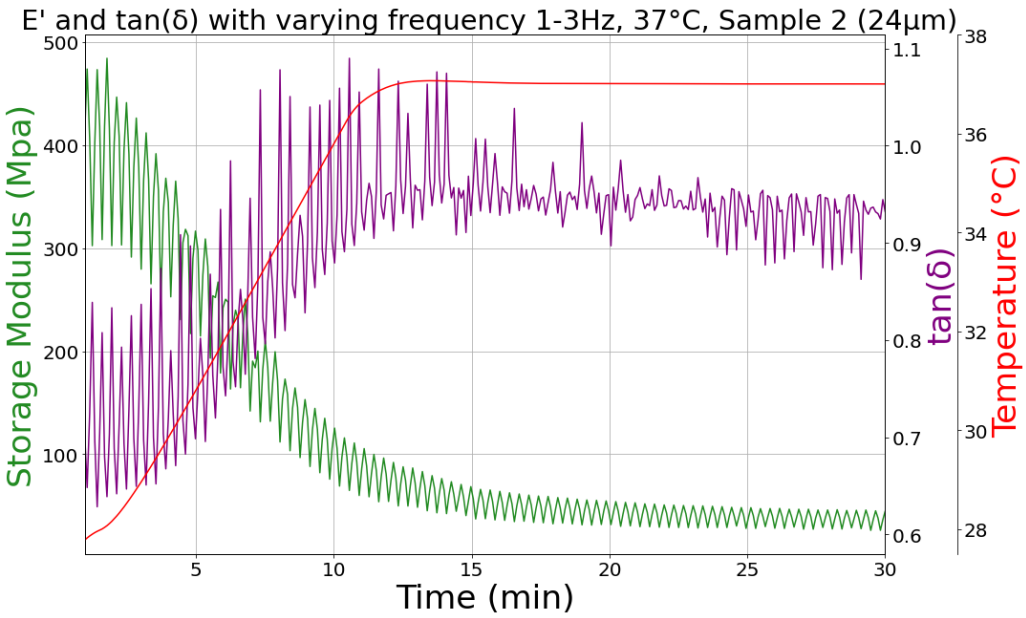

Figure 2.27: MM10 storage modulus and tan delta with varying temperature, rising from 27.5° to 37.0°C (1°/min) and then constant temperature (37°C) for 15 minutes. The frequency of the applied dynamical load cycles in steps of 1, 2 and 3Hz (7s. per step).

It was observed that temperature has a larger influence than frequency on MM10 stiffness (E') and damping ($tan(\delta)$) (see fig. 2.27). When the temperature was slowly increased from 28° to 37°C (1°/min), an eight-fold decrease in storage modulus was observed (from 400MPa to 50MPa).During this increase, the frequency of the dynamical load was constantly varied between 1,2 and 3 Hz. Correspondingly, the tan delta increased from 0.75 to 0.95 during heating from 28° to 37°C. When the temperature was kept constant at 37°C for >15 minutes, storage modulus and tan delta were constant. It can therefore be concluded that temperature is the decisive influence on the material properties. We observe a very high tan delta (> 0.7) at the whole temperature range. This indicates that the temperatures lie within the glassy temperature (T_g) range, as reported in [40] . This finding corresponds to findings during static stress-strain measurements, where Young's moduli decreased heavily in this temperature range.

Light-dependent dynamical behavior of MM10

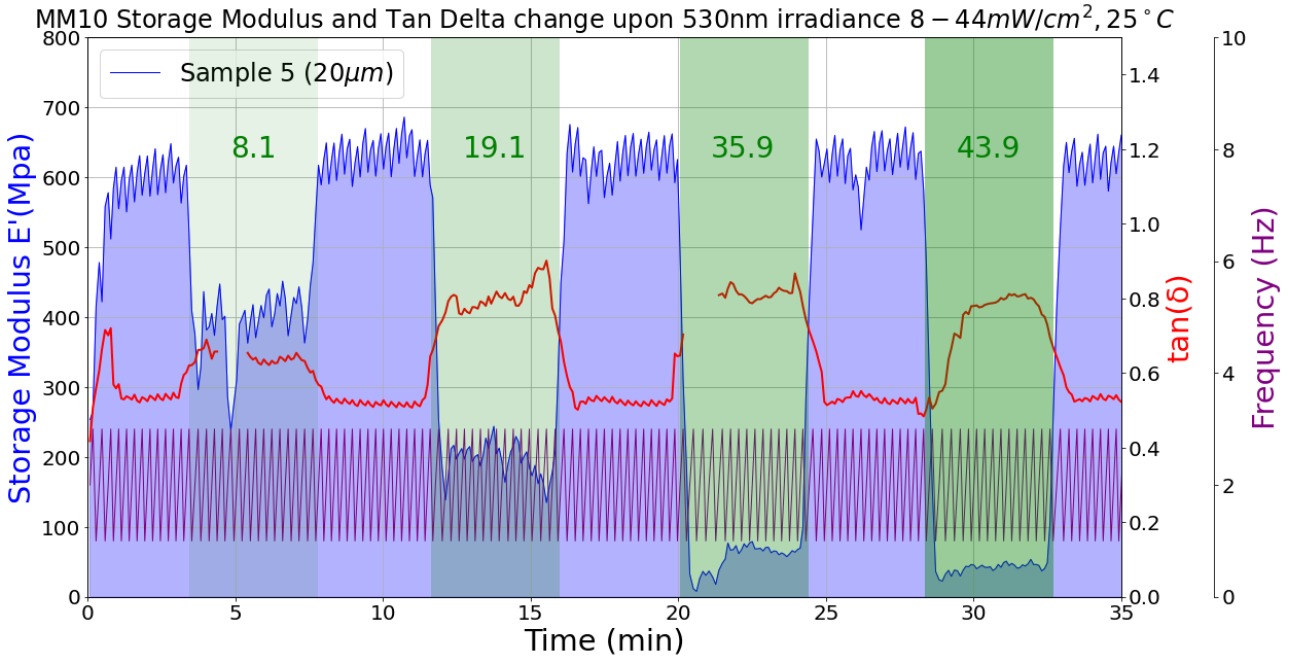

Figure 2.28: Influence of irradiation on MM10 storage modulus and tan delta. Irradiance was increased every lightning period of 5 minutes (green blocks, mW/cm^2). A dynamical load was applied by the DMA with an amplitude of $10\mu m$ (sample length is 16mm) in a varying frequency of 1,2 and 3 Hz (60,120, 180bpm).

An MM10 sample ($21\mu m$ thickness) was placed in DMA and exposed to a dynamical displacement of $10\mu m$ with a varying frequency of 1,2 and 3 Hz (see figure 2.28 and supplementary Movies). The preload is 10mN. After 5 minutes of calibration, the sample was irradiated with the 530nm LED beam at a time interval of 5min. on / 5min. off (using the square pulse generator) with an increased irradiance per lightning period. The irradiance steps taken were 8.1, 19.1, 35.9 and 43.9 mW/cm^2 (see green blocks in fig. 2.28).

Irradiance (mW/cm^2)	**E'**(mean)	**tan(δ)** (mean)
0	603 (=100)	0.52 (=100)
8.1	398 (-34%)	0.63 (+21%)
19.1	210 (-65%)	0.78 (+50%)
35.9	63 (-90%)	0.82 (+58%)
43.9	42 (-93%)	0.78 (+50%)

Table 2.8: MM10 Mean storage value E' and tan delta upon illumination with 530nm LED light

When the sample is irradiated, contraction takes place. As a result, the storage modulus declines, while the tan delta increases. This means that the elasticity of the material declines and the damping increases upon illumination. The storage modules decrease is larger when irradiance is increased. This can be explained by our earlier findings that an increased irradiance causes an increased contraction, in a linear fashion (see contraction tests). We observe that the storage modulus decreases up to 12-fold upon irradiation with $43.9mW/cm^2$ (the maximum irradiance before the sample is expected to breakdown, see table 2.8). Such behavior is not observed in the tan delta values. As tan delta is only dependent on the storage modulus and the loss modulus, this must mean that a decrease in storage modulus E' goes hand in hand with a decrease of the loss modulus E'' (though this decrease is somewhat smaller, as tan delta increases during illumination).

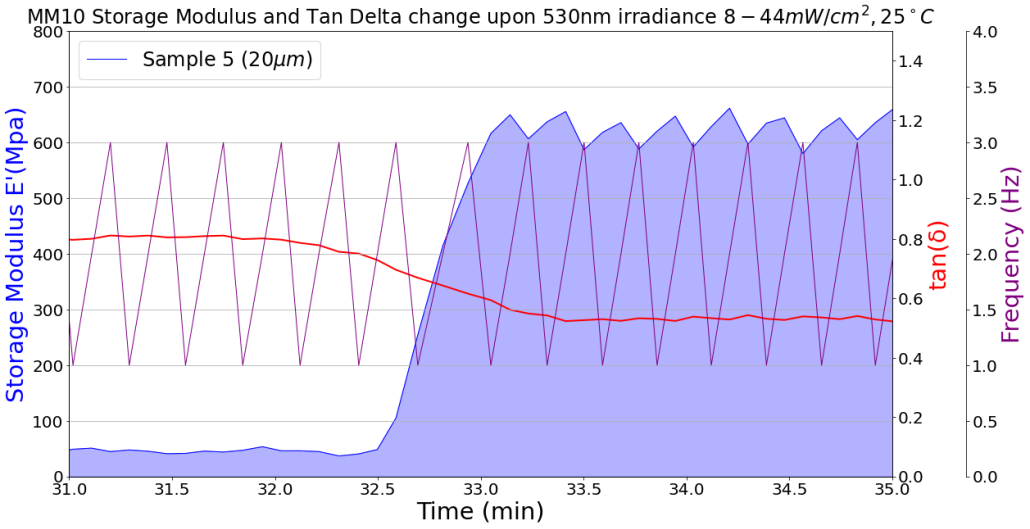

Figure 2.29: Influence of irradiation on MM10 storage modulus and tan delta. A dynamical load was applied by the DMA with an amplitude of 10µm (sample length is 16mm) in a varying frequency of 1,2 and 3 Hz (60,120, 180bpm). This is a close-up of figure 2.28

Upon closer inspection, it can be observed that the frequency of dynamical load (varying between 1,2 and 3 Hz) influences the storage modulus: The higher the frequency, the lower the storage modulus and vice versa (see figure 2.29). This could be explained by the lower recovery time of the material to its original (more elastic) state upon higher frequency loads.

2.4 Order parameter determination

To find the order parameter S, we use [45]:

$$S = (Ab_{\parallel} - Ab_{\perp})/(Ab_{\parallel} + 2 \cdot Ab_{\perp})$$

Where $Ab_{\parallel}$ and $Ab_{\perp}$ are the absorbance for light polarized parallel and perpendicular to the direction of the applied strain (which is the same direction as the nematic director of the LCE). We again approximate the absorbance (fraction) as 1 minus the transmission and the reflection:

$$Ab_{\parallel} \approx 1 - (T_{\parallel} + R_{\parallel})$$
$$Ab_{\perp} \approx 1 - (T_{\perp} + R_{\perp})$$

The reflection was measured $5.53 \pm 0.22\%$ in the LED spectrum for non-polarized light and is assumed to be equal in polarized light. The transmission however is extremely dependent on polarization direction. We measure the transmission to be 8.3% when the polarization direction is perpendicular to the nematic director of LCE at t=0. We measure the transmission to be 0.3% when the polarization direction is parallel to the nematic director.

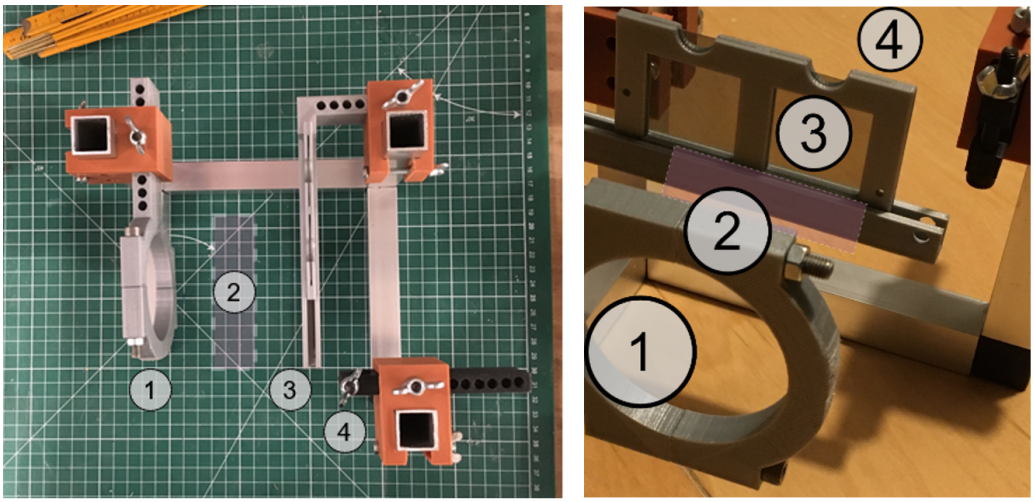

Figure 2.30: Left: Top view of the frame with the rail attached, allowing changing of polarizing filter direction during experiments. Right: Close-up of measurement frame, (1) collimated beam holder (2) location for LCE sample in DMA machine (3) linearly polarized filters rail (4) holder for irradiance detector. Note: the position of the filters and sample can be interchanged during experiments.

The setup described above was used with the addition of linearly polarized filters between the light beam and the MM10 sample (see figure 2.30). The sample is, mounted between the DMA clamps with the nematic director in the stretching direction. First, a filter with the polarization direction perpendicular to the nematic director is applied. Hereby, only green light is passed through with the polarization direction parallel to the nematic director.

When a polarizer with the filtering direction parallel to the nematic director was applied, higher transmission was measured (see table 2.9). This filter lets through only light with a polarization direction perpendicular to the nematic director. This light will largely pass through the LCE sample, because the sample's inner polymer alignment prevents large uptake of the light perpendicular to the polymer's backbone direction. So, a larger transmission is measured (see figure 2.31).

It was measured that a single polarizer already causes a loss of 58.1% of irradiance (see figure 2.31). A stress-strain experiment was performed on an MM10 sample (182x9mm, thickness $32\mu m$) with a strain rate of $50\mu m$ up to 1000 μm (105.5% of it's original length). The experiment was performed at 25°C with an initial displacement of 0 and a static force of 10mN. **We calculated the order parameter as stated above to be around 0.50. The order parameter did not significantly change during stretching.** (see tab. 2.9).

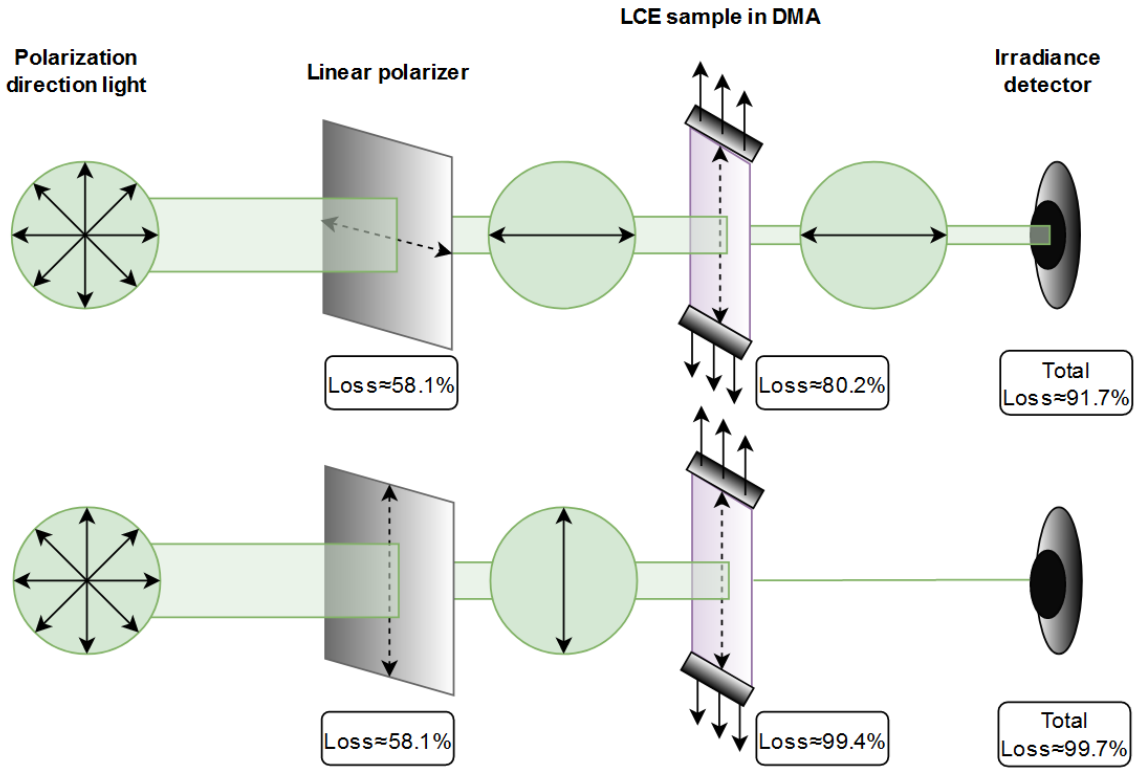

Figure 2.31: Schematic test setup with linear polarizers applied during DMA testing where a displacement of $50\mu m/min$ is applied up to 1000μm. Losses in irradiance are measured before any strain was applied (t=0). These losses are due to absorbtion, reflection and scattering of incoming light.

$I_0 = 15.1mW/cm^2$	**Transmission, Refl=0.055**				**Order param.**
Displ. (μm), $l_0 = 18250\mu m$	$T_\parallel$		$T_\perp$		$S = \frac{Ab_\parallel - Ab_\perp}{Ab_\parallel + 2 \cdot Ab_\perp}$
	$\frac{mW}{cm^2}$	$\frac{T_\parallel}{I_0}$	$\frac{mW}{cm^2}$	$\frac{T_\perp}{I_0}$	
0	0.198	0.061	2.99	0.253	0.510
100	0.110	0.062	2.83	0.242	0.491
200	0.110	0.062	2.86	0.244	0.494
300	0.110	0.062	2.88	0.246	0.494
400	0.113	0.062	2.91	0.248	0.495
500	0.112	0.062	2.94	0.250	0.497
600	0.115	0.063	2.96	0.251	0.501
700	0.115	0.063	2.99	0.253	0.503
800	0.119	0.063	3.03	0.256	0.505
900	0.120	0.063	3.04	0.256	0.506
1000	0.122	0.063	3.09	0.260	0.509

Table 2.9: Measured transmission through MM10 sample (32μm thickness) with polarized filters applied, corrected for daylight irradiance. The sample was irradiated with polarized green light perpendicular and parallel to the nematic director while stretched with $50\mu m/min$. Transmissions were measured and calculated as fraction of the irradiance I_0, reflection was found in earlier experiments. Order parameter was calculated as explained.

It was found that the MM10 sample proved to be less elastic when the polarizer was placed perpendicular to the nematic director than when placed parallel (see fig. 2.32). This can be explained by the fact that MM10 absorbs more light polarized parallel to the nematic director (a lower transmission so a higher absorption is observed, see table 2.9). If the polarizer is placed parallel to the nematic director, all such light is blocked, resulting in less absorption and higher transmission. This absorption causes contraction of the MM10, resulting in less elasticity (more stress generation). It can be seen in figure 2.32 that the stress strain diagram is very linear in the whole range of the experiment (0-6% strain). **Therefore, we argue that MM10 keeps a constant amount of contraction for 20-minutes of illumination during the stress-strain test.**

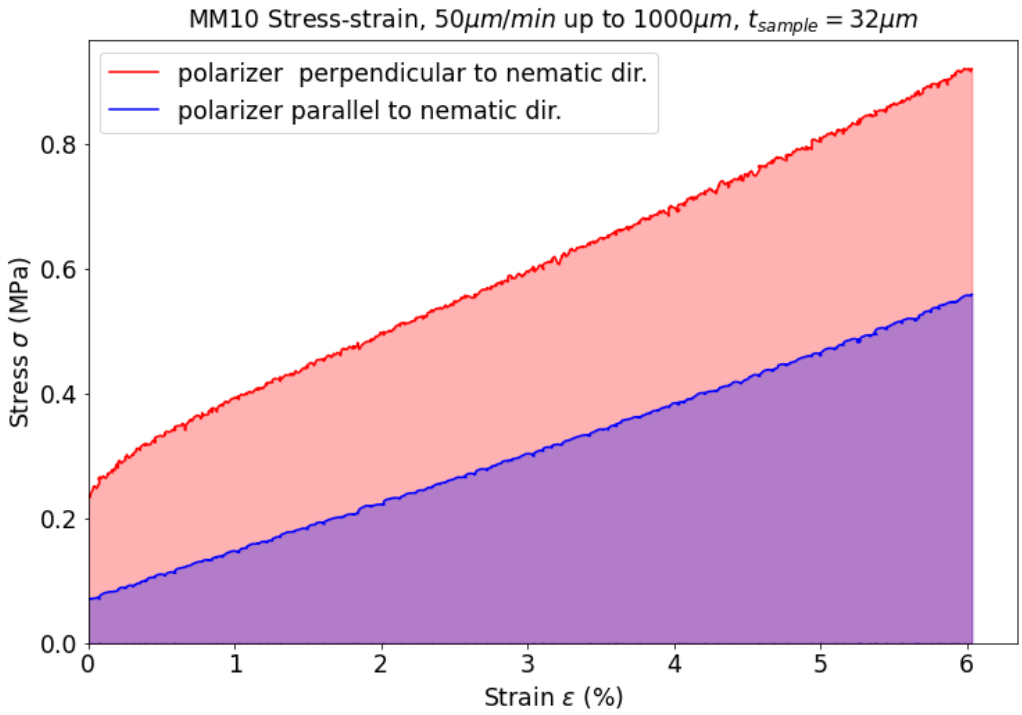

Figure 2.32: MM10 is highly reactive to polarized light direction, because of the inner structure (nematic director). When a stress-strain test is performed, a stronger MM10 is seen when the linear polarizer is perpendicular to the nematic director, than when the polarizer is parallel to the nematic director. This is because MM10 absorbs more light parallel to the nematic director (let through by the perpendicular polarizer), causing contraction of the material.

2.5 Active mechanical properties of MM10

A custom-made aluminium/3D-printed frame was used to hold all equipment in the DMA machine (see figure 2.33). This allowed for optimal placement (3 degr. of freedom) for all used equipment. A 530nm green LED (*ThorLabs M530L3*) was placed in the holder with a collimating lens attached (*ThorLabs COP1-A*). An irradiance detector was placed behind the MM10 sample (*ThorLabs S130VC*). The measured irradiance was then displayed on a hand-held energy meter (*ThorLabs PM400*). Baseline daylight irradiance was $1.7\mu W/mm^2$. Maximum beam intensity was $89.1\mu W/mm^2$. It was found that the measured irradiance did not depend on the distance of the detector to the light beam. The LED was powered by a current driver (*ThorLabs LEDD1B*, 3.2V, 1A).

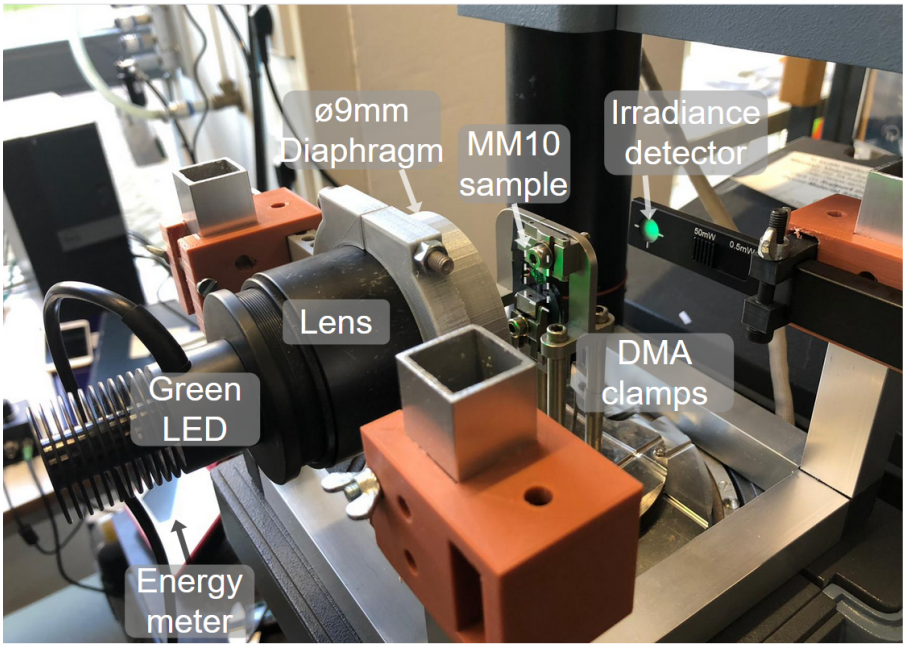

Figure 2.33: Used setup for light stimulus experiments in the DMA machine. A 530nm-LED was applied with a collimating lens, providing homogeneous irradiance onto the MM10 sample surface, which was clamped in the DMA machine. The DMA can apply force or (pre)strain on the sample, as well as record generated force by the sample upon light stimulus. Irradiance was measured by a digital photodiode connected to a display (energy meter). All equipment is held together by a custom-made frame

Applied pre-strain

An MM10 sample was placed in the DMA machine and force generation upon light stimulus was measured with three different pre-strain rates applied: 0.1%, 1% and 2%. Also, a higher pre-strain of 4% was applied, but this lead to immediate breakdown of the sample, possibly due to the abrupt onset of the strain. For the pre-strain rates of 0.1,1 and 2%, the sample was tested for 15 minutes at a static force of 10mN. During this time frame, the LCE was stimulated by the collimated beam ($89.1\mu W/cm^2$) using a pulse generator (*LXI 33210A*). A square pulse was generated continuously for 60 seconds on – 60 seconds off. By doing so, at least 5 LCE contractions were recorded as a result of the stimulus. No differences in the generated contraction force were found between different pre-strain rates (see figure 2.34). **Therefore, we use a pre-strain rate of 0.1% in all our experiments**.

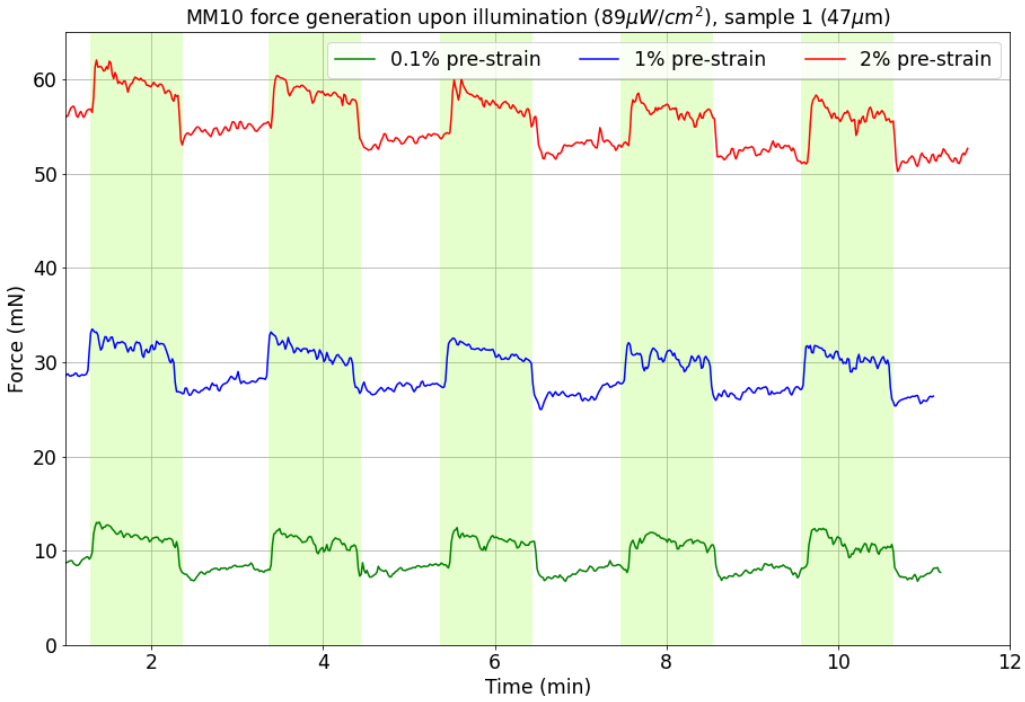

Figure 2.34: Different pre-strain rates were applied to an MM10 sample (0.1,1 and 2% pre-strain) and the generated contraction force was recorded upon 530nm light stimulation (89.1$\mu W/cm^2$, green bands). Square pulses of 60 sec. ON / 60 sec. OFF were applied during a 15 minute period.

Timing interval of illumination

One sample was tested at three different time intervals, with the LED illumination on/off timing 5/5, 10/10 and 15/15 seconds at an irradiance of 24.4mW/cm^2 (see figure 2.35). It was seen that a schedule of 5/5 produced a lower contraction than 10/10, and 10/10 produced a lower contraction than 15/15. **That is why a schedule of 15/15s. was chosen as timing interval in our experiments.** A clear plateau was visible (especially at higher intensities) so the maximum response could be observed, where this is not the case in the 5/5 and 10/10 regimen.

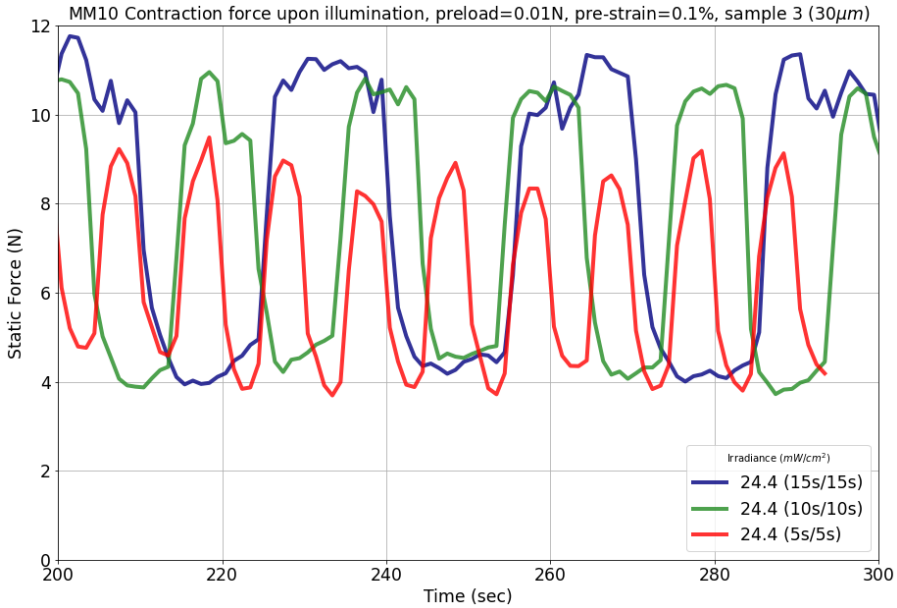

Figure 2.35: Testing of a MM10 sample at a constant irradiance but with different on/off intervals (5/5, 10/10 and 15/15s). At the 15/15 interval, a clear plateau phase is reached, whereas this is uncertain at shorter intervals.

MM10 Displacement upon illumination

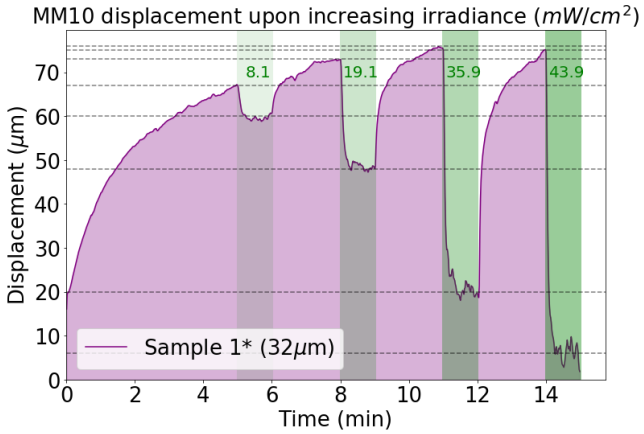

Figure 2.36: Displacement of an MM10 sample mounted between DMA clamps, with nematic director parallel to the clamps. Irradiance was given with the green 530nm LED beam. Displacement was recorded.

An MM10 sample (16x9.3mm, thickness $32\mu m$) was mounted in between the DMA clamps, without any prestrain applied, for 15 minutes at $25°C$. After 5 minutes of resting, the green LED was turned on for one minute, then turned off for two minutes. This cycle was repeated four times, with each time an increased irradiance. Displacement (μm) was measured by the DMA.

We see a steady elongation of the MM10 sample during rest (see figure 2.36). This can be attributed to the fact that the elastic MM10 responds to the weight of the bottom clamp.

It can be seen that the irradiance causes a negative displacement (=contraction) of the material as expected (see table 2.10). A higher irradiance generates more displacement, with an observed maximum of 0.42% shrinkage.

Irradiance (mW/cm^2)	**Length** (μm)	**Displacement** (%)
0	16248	0
8.1	16241	-0.043
19.1	16223	-0.1539
35.9	16192	-0.3447
43.9	16179	-0.4247

Table 2.10: Displacement of MM10 sample upon green LED illumination with increasing irradiance. A negative displacement means a contraction of the sample.

MM10 Contraction force upon illumination with green LED light

Six samples (19±1.9, 21.8±2.0, 34±2.2, 29±2.8, 21±1.4 and 51±1.8 μm thickness) were mounted in the DMA clamps and irradiated on incremental irradiance levels from 3.9 up to $53.2 mW/mm^2$. The earlier described setup with a green (530nm) collimated LED beam was used. A pulse generator generated a square pulse in a timing interval of 15s. on 15s. off. Ten separate contractions were recorded at each irradiance level (see figure 2.38). For each contraction, the plateau phase was found in the data, and the mean contraction force was calculated over this interval (spanning over ±11sec.). This mean force (corrected for the baseline force) was then divided by the cross-sectional area of the sample A_0 to obtain the generated stress $\sigma(mN/mm^2)$ or contraction force per cross-sectional area. A baseline correction could well be done because no drifting of the baseline was observed (see figure 2.37). Sample 1 broke at an irradiance of $53.2 mW/cm^2$, sample 2 at $42.0 mW/cm^2$, sample 3 and 4 at $43.3 mW/cm^2$, and sample 5 and 6 at $41.1 mW/cm^2$. **We observe a clear linear trend in the relation between irradiance and generated stress** (see fig. 2). However, we see that thicker samples relatively under perform compared to thinner samples. The three thinnest samples (3,4,6) produce a higher contraction force per area than the three thickest samples (1,2,5). **This indicates that thin samples generate force more efficiently than thick samples upon one-sided illumination.** As such, penetration depth of the light plays an important role in LCE force-generation.

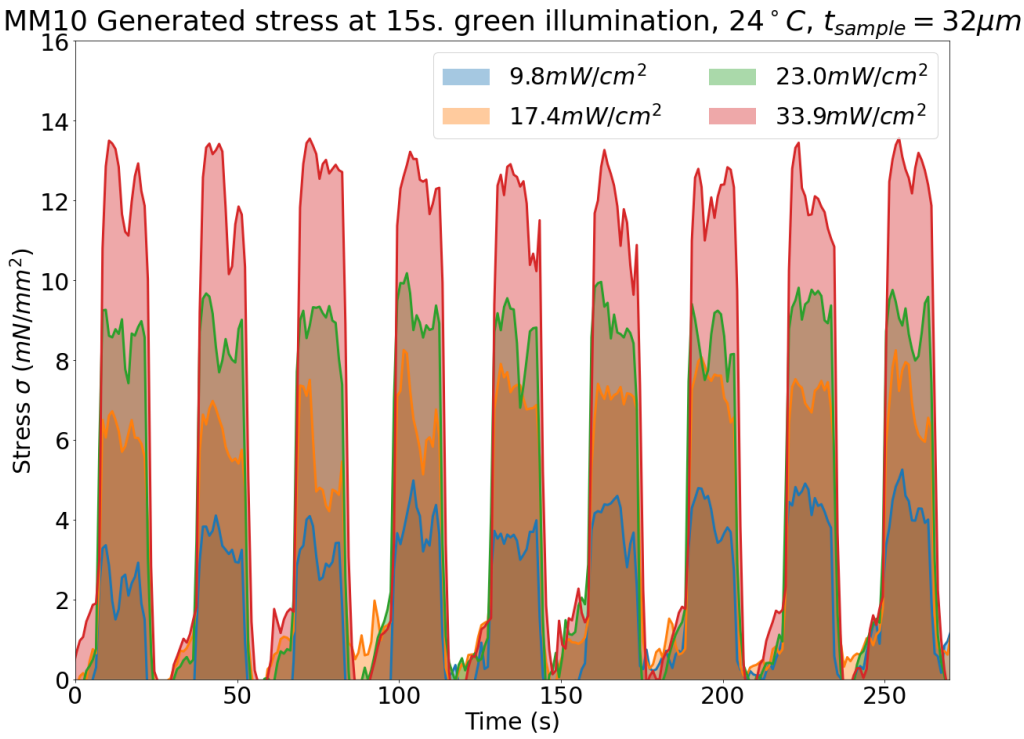

Figure 2.37: Generated stress upon MM10 illumination in one sample at varying irradiance steps. For each step, at least 10 contractions were recorded. No baseline drift is observed.

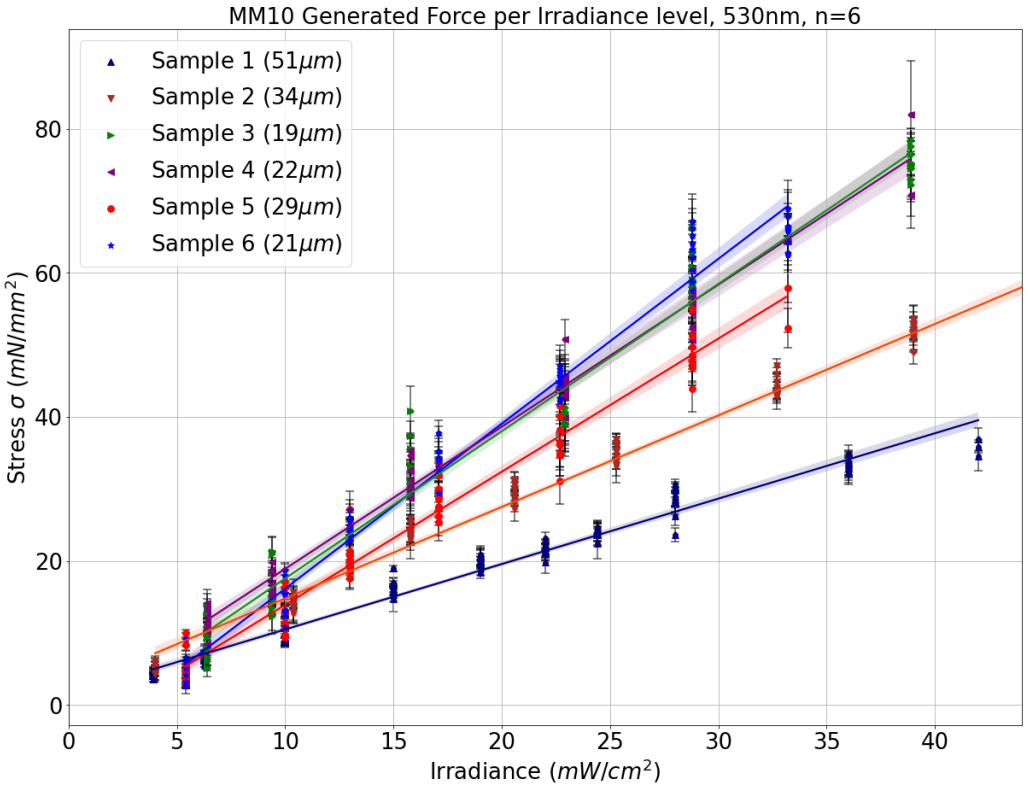

Figure 2.38: Generated stress for several MM10 samples under green (530nm) LED irradiance at ten different intensity levels. Every data point is the mean stress of a 'contraction plateau' during illumination (standard deviations are displayed). For all samples, trend lines are displayed. T=25°C.

The applied preload was 10mN per sample. Given that the average sample has an cross-sectional area of $20 \cdot 10^{-3} * 7 = 0.14mm^2$, this means that a pre-stress of $71.4mN/mm^2$ was applied. We find a maximum stress generation of approximately $60mN/mm^2$. If we imagine an MM10 string with a cross-sectional area of

$1cm^2$, it could theoretically bear a 7.14N preload and generate an additional 6N of contraction force, given all circumstances equal. This means that such a string could hold more than 1kg of weight.

DR1-MM10: LCEs responsive to blue light

In similar fashion, three samples of DR-1 MM10 were tested. These are newer MM10 samples with a modification of the azobenzene group, causing the samples to react to blue light (460nm) instead of green light. Results can be seen in figure 2.39. **We find that DR-1 MM10 shows a stress-generating capacity similar to MM10.** Because of the higher efficiency of blue LEDs compared to green LEDs, DR-1 MM10 can be a worthy replacement for MM10 to lower the power needed for stress generation.

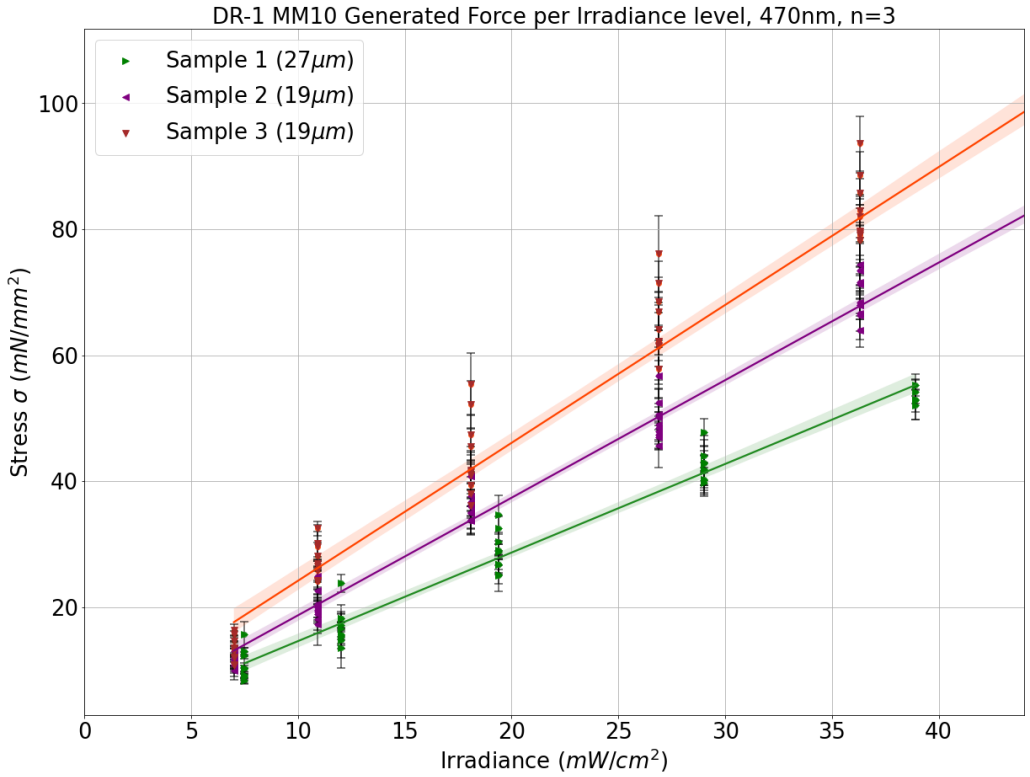

Figure 2.39: Generated stress for three DR1-MM10 samples under blue (470nm) LED irradiance at different intensity levels. Every data point is the mean stress of a 'contraction plateau' during illumination (standard deviations are displayed). For all samples, trend lines are displayed.T=25$°C$.

Linear approximations

When we make a linear regression of all MM10 data points (see figure 2.40), we find a linear approximation ($R^2 = 0.7618$):

$$\sigma_{MM10} = 1.517 \cdot I + 0.4182$$

Where σ is the stress in mN/mm^2 and I is the irradiance in mW/cm^2 (see figure 4).

If we take only the three thinnest MM10 samples (with mean thicknesses of 19,21 and 22 μm) and apply the same linear regression we find a very accurate approximation ($R^2 = 0.9736$):

$$\sigma_{MM10} = 2.1054 \cdot I - 3.528$$

We do the same for DR1-MM10, the LCE variant reacting to blue light. We find a similar linear approximation ($R^2 = 0.8911$):

$$\sigma_{DR1-MM10} = 1.9875 \cdot I - 1.3713$$

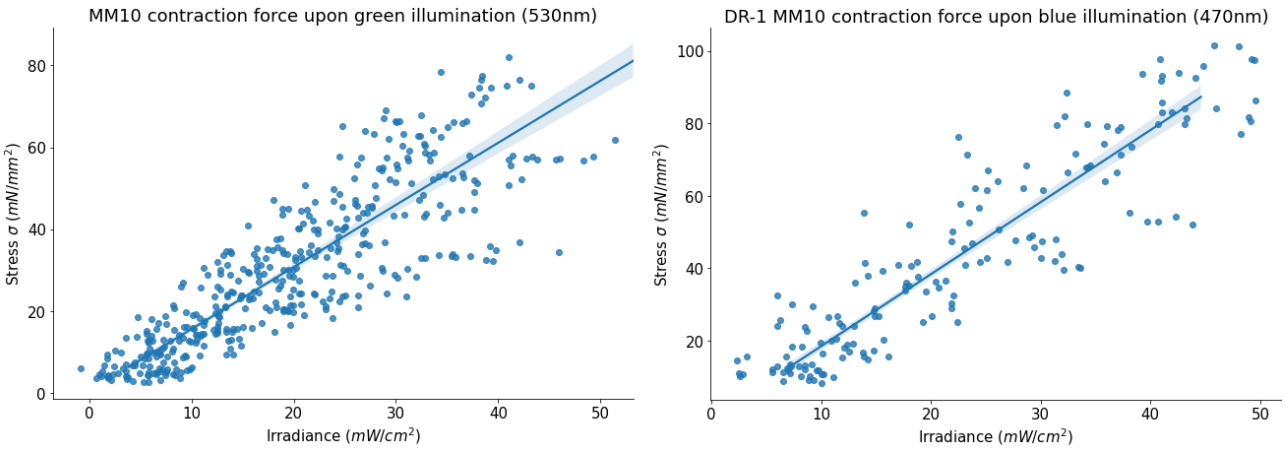

Figure 2.40: Scatter plots of MM10 contraction force (left) and DR-1 MM10 (right) containing all data points (which are jittered for display purposes). Linear trend lines are displayed.

Environmental temperature influence

One very hot day in summer, the contraction experiment was repeated. After analysing, a large difference was found in the stress generation capacity of the same samples (of 27 and 32μm thickness) on different days. All other things equal, only the room temperature in the lab differed between experiments (24.0 vs. 26.5°C). Results are displayed in fig. 2.41. We found that the samples generated a (far) lower stress when the temperature was increased 2.5 degrees. Furthermore, samples at 26.5°C could endure much higher irradiance before breakdown than at 24°C ($\pm 65 mW/cm^2$ vs. $\pm 35 mW/cm^2$ resp.). This can be explained by our earlier findings of a higher elasticity at higher temperatures.

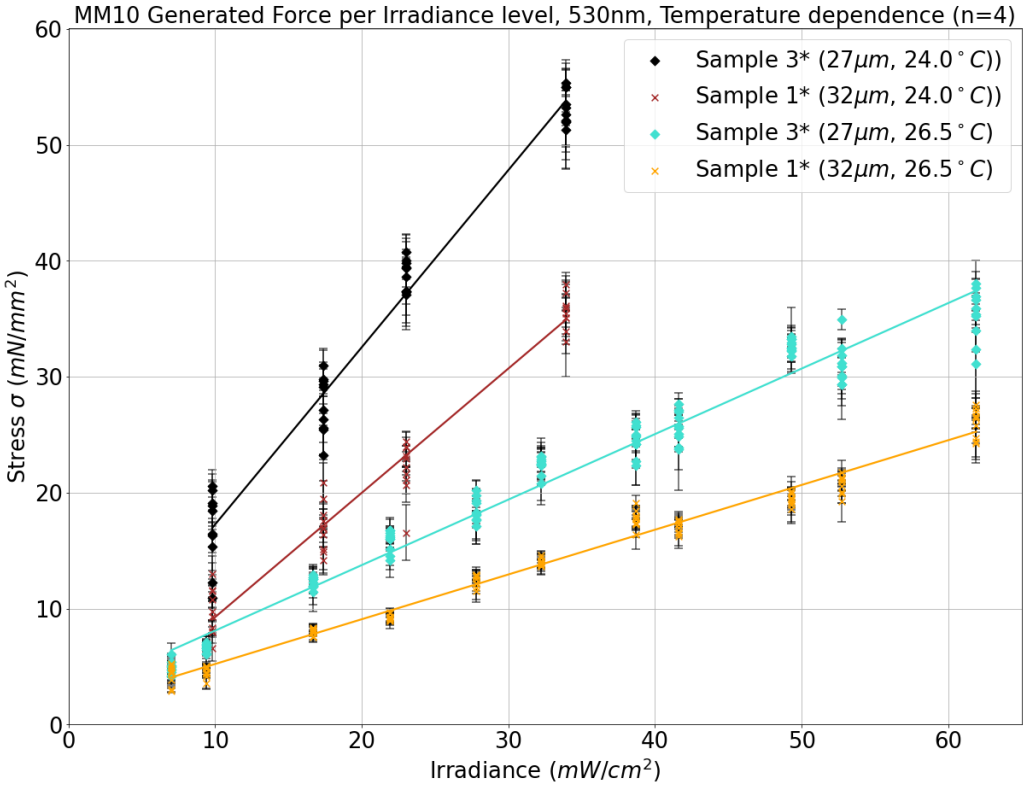

Figure 2.41: Differences in stress generation of two samples tested at different room temperatures.

Our findings show that environment temperature plays a very important role in MM10 behaviour. This has to be taken into account when making predictions or setting up models for MM10 behaviour.

2.6 Heat generation properties of MM10

As explained in the literature review, MM10 contraction depends a thermo-mechanical and an opto-mechanical effect. The thermo-mechanical effect consists of local heating of MM10 above the phase transition temperature. This occurs not by direct heating of MM10 by the light source, but by indirect heating through azobenzene light absorption. It is therefore interesting to measure surface temperature of MM10 upon illumination. This is done in this chapter. Movies of these experiments can be found in the 'Movies' section.

2.6.1 Surface temperature development in MM10: IR-measurements

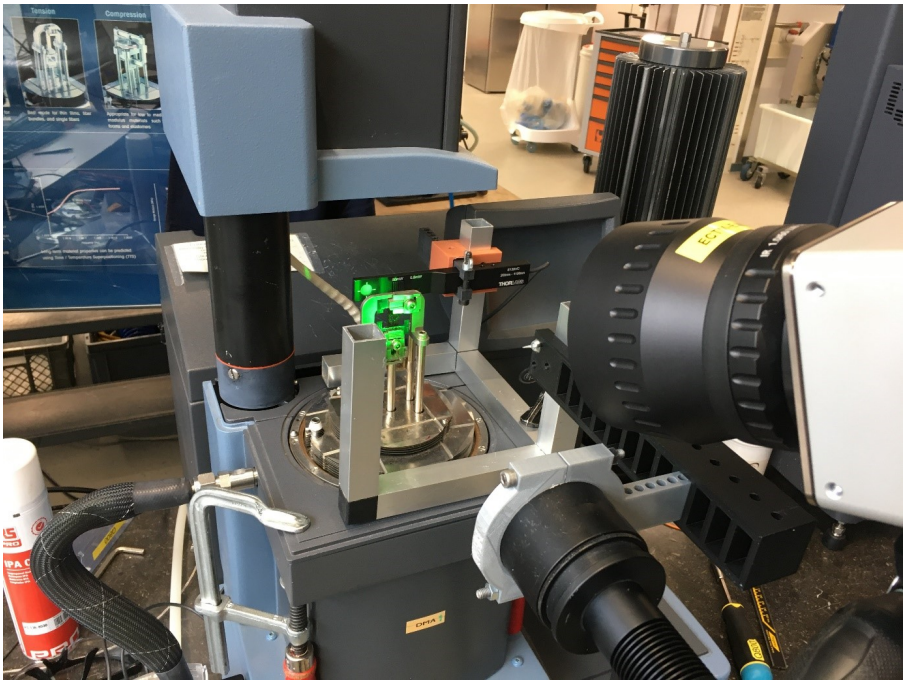

Figure 2.42: Setup of MM10 surface temperature measurement using an HD infrared camera during illumination in DMA machine.

A 27μm-thick MM10 sample was placed in the DMA without any stress applied. The samples were illuminated at various irradiance steps as earlier described. Heat generation on MM10 surface was measured with an infrared detector (*Infratec VarioCam 800HD*, close-up-lens 0.5x to 60 mm) while irradiated at a timing interval of 15s. on 15s. off (with use of a square wave pulse generator) (see fig. 2.42, 2.43). At each intensity, three separate illumination periods were recorded. The green light is assumed not to interfere infrared detection because the light spectrum (500-600nm) is far lower than the detection region of the infrared camera ($\geq$7500nm). **The infrared emissivity coefficient was set to 0.7 as in other LCEs [30], though it is not confirmed for MM10.** We found that temperature increases with higher irradiance (see fig. 2.44). During the 15s. off periods, the samples cooled down to baseline temperature (24.2°C) at every intensity. Temperatures were measured as average over a 5mm-diameter circle around the beam center on the MM10 surface, and the maximum reached during a 15 second illumination period was recorded as displayed in fig. 2.44 and 2.45.

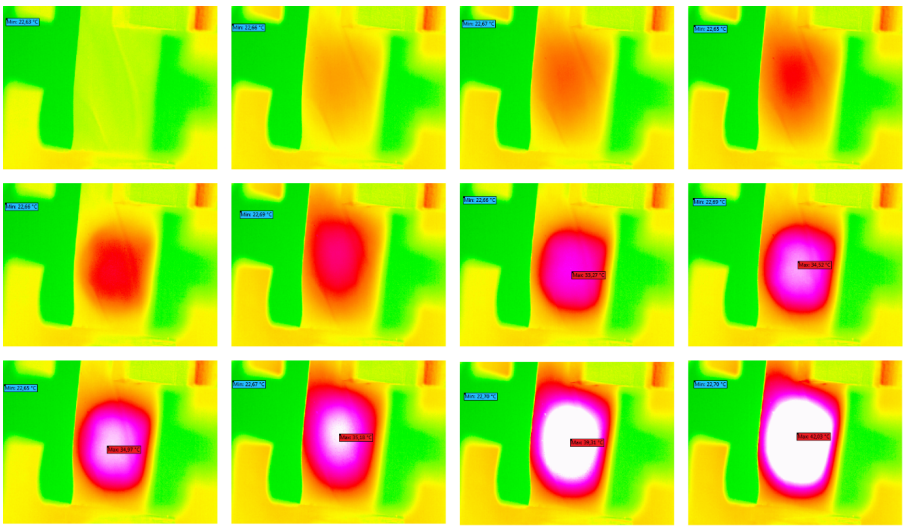

Figure 2.43: Gradual heating of a $27\mu m$-thick MM10 sample upon 15s. irradiation with the green LED at an intensity of $51.5mW/cm^2$. This intensity is around the maximum irradiance a fixed sample can bear before breakdown. Heating is caused by the incorporated light-responsive azobenzene molecules. A few seconds after the start of illumination, the maximum temperature of $39.02°C$ was observed while the environment is at room temperature ($24.2°C$).

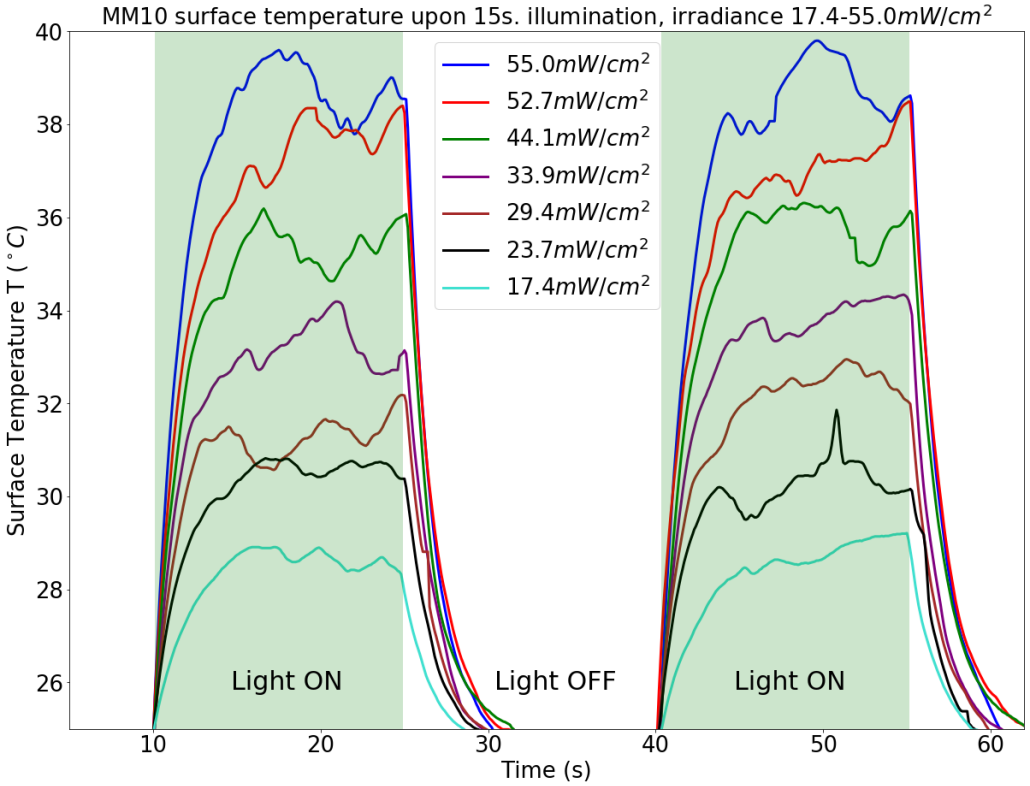

Figure 2.44: 15s. illumination of a $27\mu m$-thick MM10 sample with the green LED. Surface heat is recorded by an IR-camera at different intensities. Emissivity coefficient is set at 0.7.

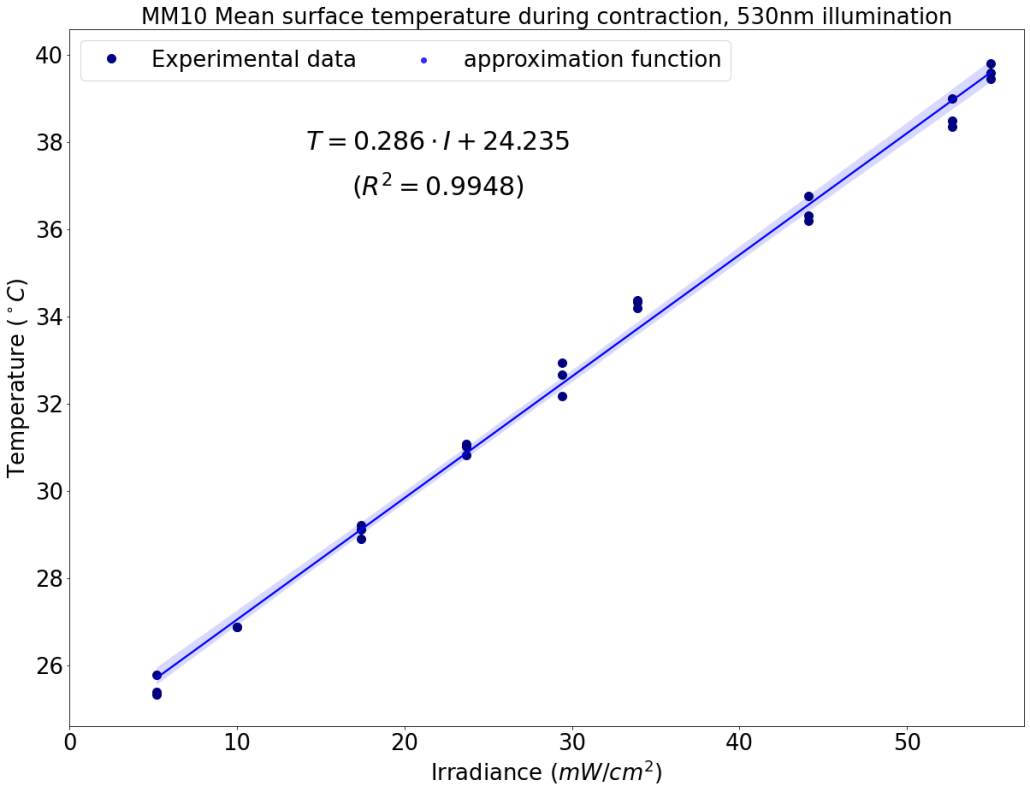

Figure 2.45: Average temperature on MM10 surface upon (one-sided) illumination in a circle of 5mm diameter around the light beam center. Illumination was done for 15s on 15s off with a green 530nm LED. The sample thickness is $27\mu m$. A linear approximation is found.

We found a very precise linear approximation ($R^2 = 0.9948$) for the relation between the maximum MM10 surface temperature and irradiance (see fig. 2.45):

$$T_{surface} = 0.286 \cdot I + 24.235$$

Where $T_{surface}$ is the average MM10 surface temperature in a circle of 5mm around the beam center ($^\circ C$), and I is the surface irradiance of the green LED (mW/cm^2). The sample thickness is $27\mu m$.

Influence of duty cycle, frequency, and irradiance

An MM10 sample ($27\mu m$ thickness) was tested in the DMA without any strain applied, as described in the above sections. The sample was irradiated in 9 different instances, with a varying frequency (1,2 and 3Hz), duty cycle (20,30 and 50% ON time), and irradiance (17.4, 33.9 and $52.7 mW/cm^2$). Our earlier findings showed that MM10 performs optimal within this range of irradiance levels. Each instance had a duration of 10 seconds. We chose the frequency to represent real human heart rates (60,120 and 180bpm). The duty cycle is interesting because if the material performs equally on different duty cycles, the lowest duty cycle is preferred as it would save energy, and make the MM10 performance more efficient overall.

We try to see if the MM10 is able to return to baseline temperature in between light pulses. This is important because excessive heat buildup must be avoided if LCE would be applied in the human body.

Results are displayed in figure 2.46. We see that for each instance, the baseline temperature of $24.5^\circ C$ is rapidly elevated. After this onset (<3s.), the temperatures stay a new stable baseline in all instances. We see that the highest temperature is reached in 50% duty cycles, compared to duty cycles of 20 and 30%. This is expected because a higher duty cycle means more longer illumination of the MM10 and thus more absorption and conversion of light into heat. **Also, we see that the higher the irradiance, the higher baseline temperature.** We see that temperature rise moves synchronously with light frequency (see fig. 2.46). Even in very short pulses (3Hz with a duty cycle of 20%) the temperature immediately increases upon illumination, and decreases when the light is turned off (see fig. 2.46c). A maximum temperature is reached of $32.3^\circ C$, which is 7.8° above baseline.

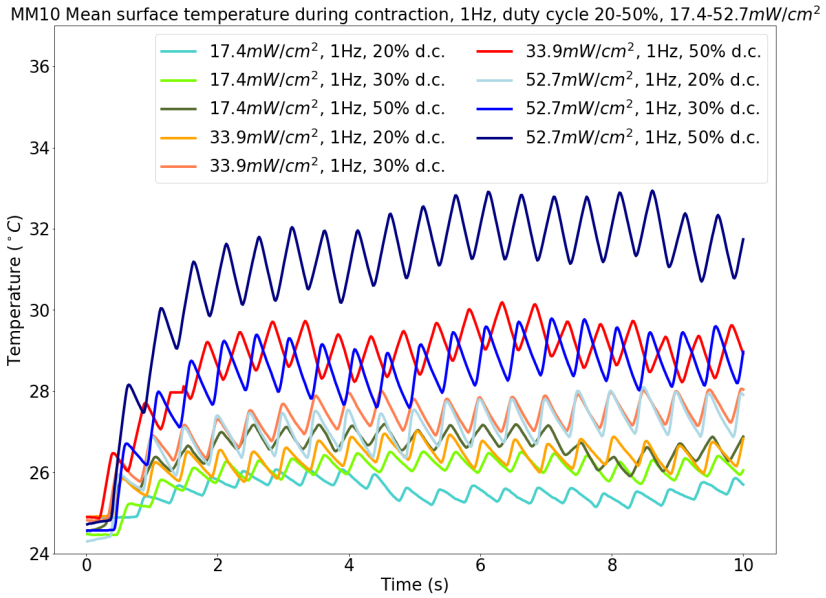

(a)

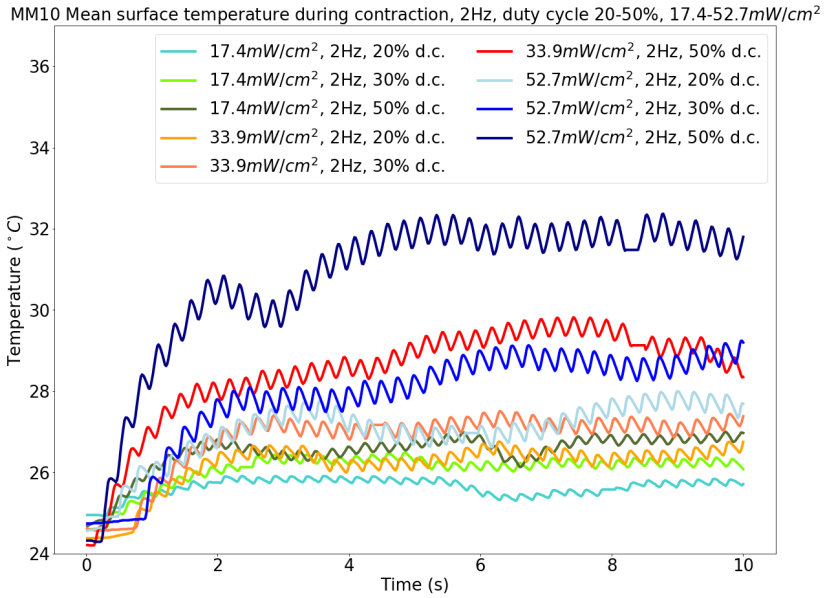

(b)

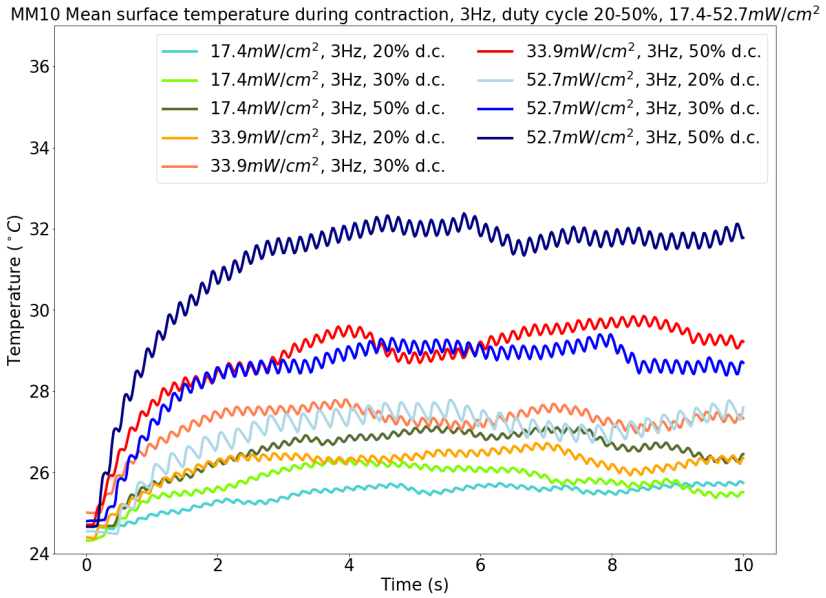

(c)

Figure 2.46: Infrared measurements of MM10 surface temperature during illumination with pulses of 1,2 and 3Hz in frequency, 20-50% in duty cycle and 17.4-52.7mW/cm^2 in intensity. Baseline temperature: 24.5°C.

We combine the three figures above into one (figure 2.47). We calculate for each measurement the total dosage of energy deposited on the MM10 surface in mW/cm^2. For example, a sample exposed to a 3Hz irradiance of $52.7mW/cm^2$ at a duty cycle of 20%, obtains an average energy dose of $52.7 \cdot 0.2 = 10.54mW/cm^2$. We see that a new baseline temperature is reached in all experiments after 5s. of illumination at 1,2 and 3Hz. This new baseline is plotted against the energy dose.

As such, we plot all measurements and find a linear approximation with high overlap ($R^2 > 0.99$):

$$T = 0.277E + 24.506$$

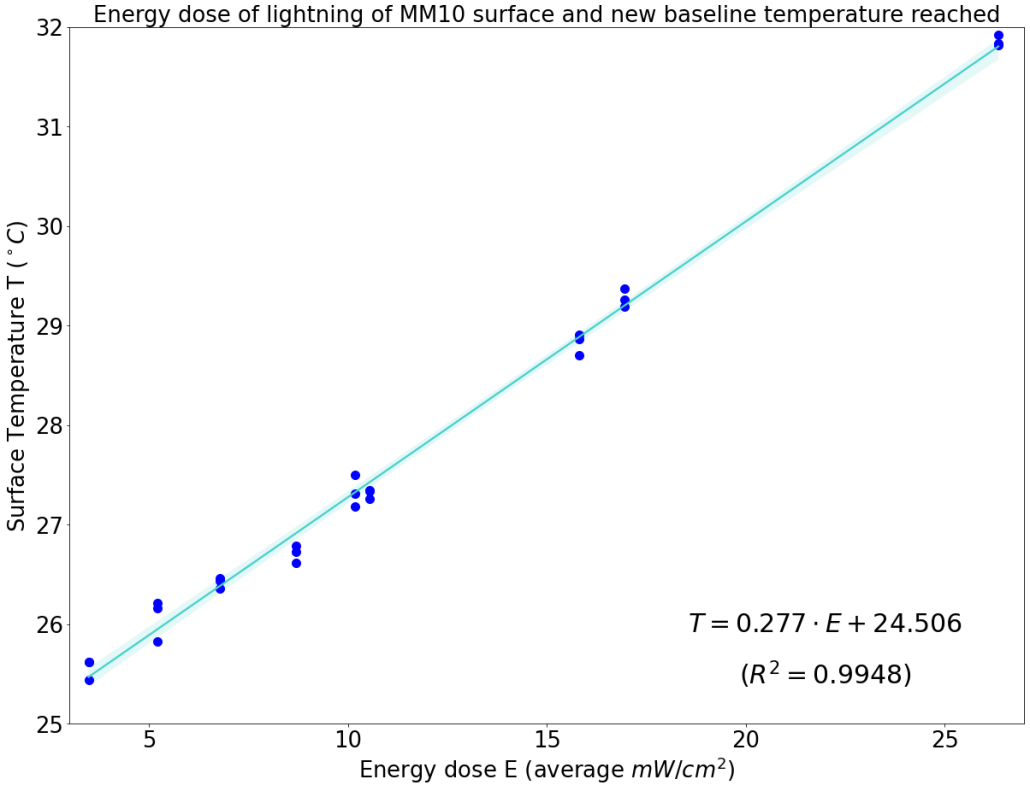

Figure 2.47: Relation between energy dosage deposited on the MM10 surface and the new stable baseline temperature reached after 5 seconds of illumination with a green LED at frequencies of 1,2, and 3 Hz. Surrounding temperature is $24.5°C$.

Surface temperature is a result of azobenzene molecule absorption of green light. The rise in surface temperature is very quick (in the order of milliseconds), as is the decrease after illumination. The surface temperature rises linearly in concordance with energy dose deposited on the surface. A new stable baseline temperature is reached in light cycles of 1,2 and 3Hz. **This means that it is possible to pace MM10 in concert with a heart rate between 60-180bpm without excessive heat build-up.** A maximum temperature on the surface is reached only after seconds. This means that the maximum achievable temperature was not reached in lightning cycles of 1,2 and 3Hz.

Speed of heat generation

We study the speed of heat generation with the same lightning settings as above. The samples were irradiated at the varying frequency, irradiance and duty cycle for 20s. per setting. At each setting, the average rise time (T_{rise}, ms) was calculated as the time it took for the sample to reach a maximum temperature from baseline when illuminated (average of 10 periods of illumination). These findings are displayed in fig. 2.48.

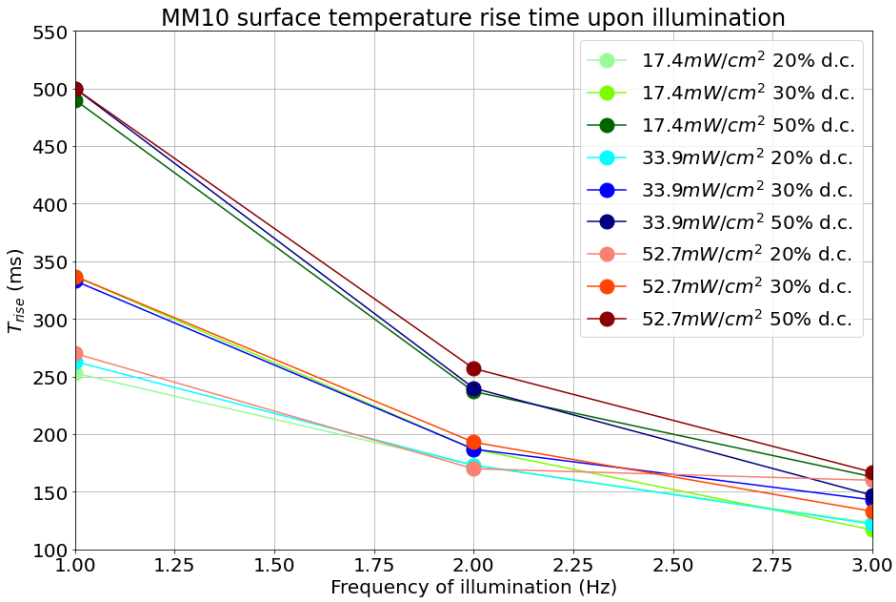

Figure 2.48: Per illumination setting, mean time from baseline to maximum temperature was calculated (T_{rise}). The green 530nm LED beam was used for illumination.

We see that rise time decreases as frequency of illumination increases. This means that in short pulse illumination, the MM10 surface does not reach it's maximum temperature (which it would achieve upon longer illumination at the same irradiance). The longest rise time is observed in the longest pulse durations (1Hz, 50% duty cycle), simply because in this setting the temperature can rise longer, without reaching the maximum temperature yet. **This maximum temperature is thus achieved upon 15s. illumination, but not in short pulse illumination.**

We can calculate duration of a light pulse:

$$T_{illumination} = 1/f * dc$$

Where $T_{illumination}$ is the illumination time in ms, f is the frequency of illumination in Hz, and dc is the duty cycle of illumination in percent. We then plot the illumination time against the rise time in fig. 2.49. There is a clear linear relationship between the illumination time and the rise time upon 1-3Hz illumination, **meaning that MM10 surface heats up in a linear fashion upon illumination, until a maximum temperature is reached.** This maximum temperature is not yet reached in fig. 2.49. The maximum surface temperature depends on the irradiance (as can be seen in fig. 2.47).

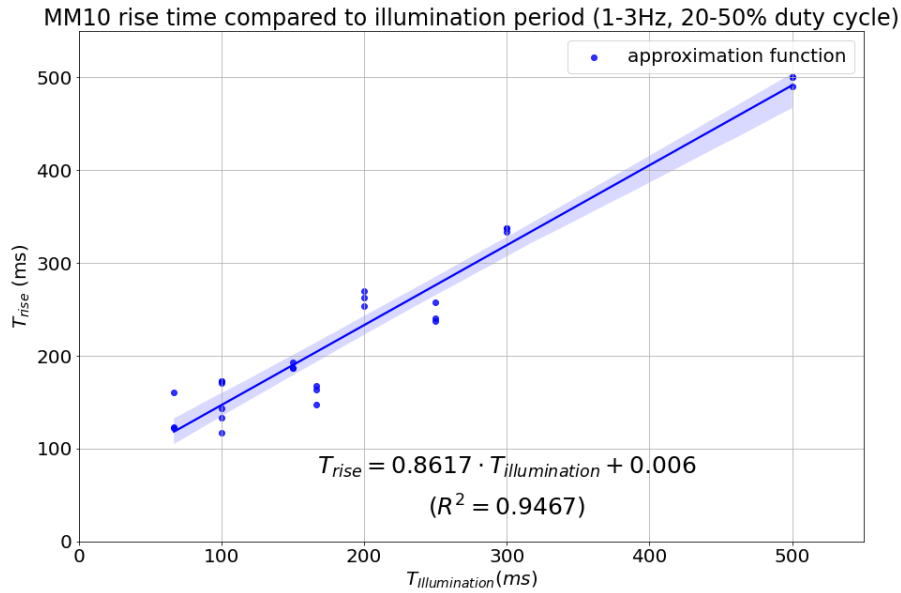

Figure 2.49: The illumination time per period of lightning was calculated compared to the rise time. A linear approximation function was found.

If the maximum surface temperature is not reached upon pulse illumination, does the MM10 then generate lower force than it would do upon long (15s) illumination? This question is investigated below.

2.6.2 Force vs. heat in 1-3Hz illumination

We compared the heat generation with generated stress in the two MM10 samples (50% duty cycle, 1-3Hz, 17.4-52.9mW/cm^2). When an illumination period started, the material started to contract (see fig. 2.50). However, not enough time was in between lightning periods to fully relax the material in between light pulses. As a result, a contraction was seen when the light cycle started, but no difference in stress generation could be seen in between light pulses. Even at 1Hz at the lowest irradiance (17.4mW/cm2), no full relaxation of MM10 was observed (fig. 2.50). **As such, it can be concluded that MM10's has a too slow response to act as effective contractile unit at a frequency of 1, 2 or 3Hz.** While we know that the *trans-to-cis* isomerization takes place in milliseconds, and observed that a full contraction only takes place after seconds, we conclude that the slow response is due to slow heating and cool down of MM10. A faster response time is thus expected in thinner samples, which are also more efficient.

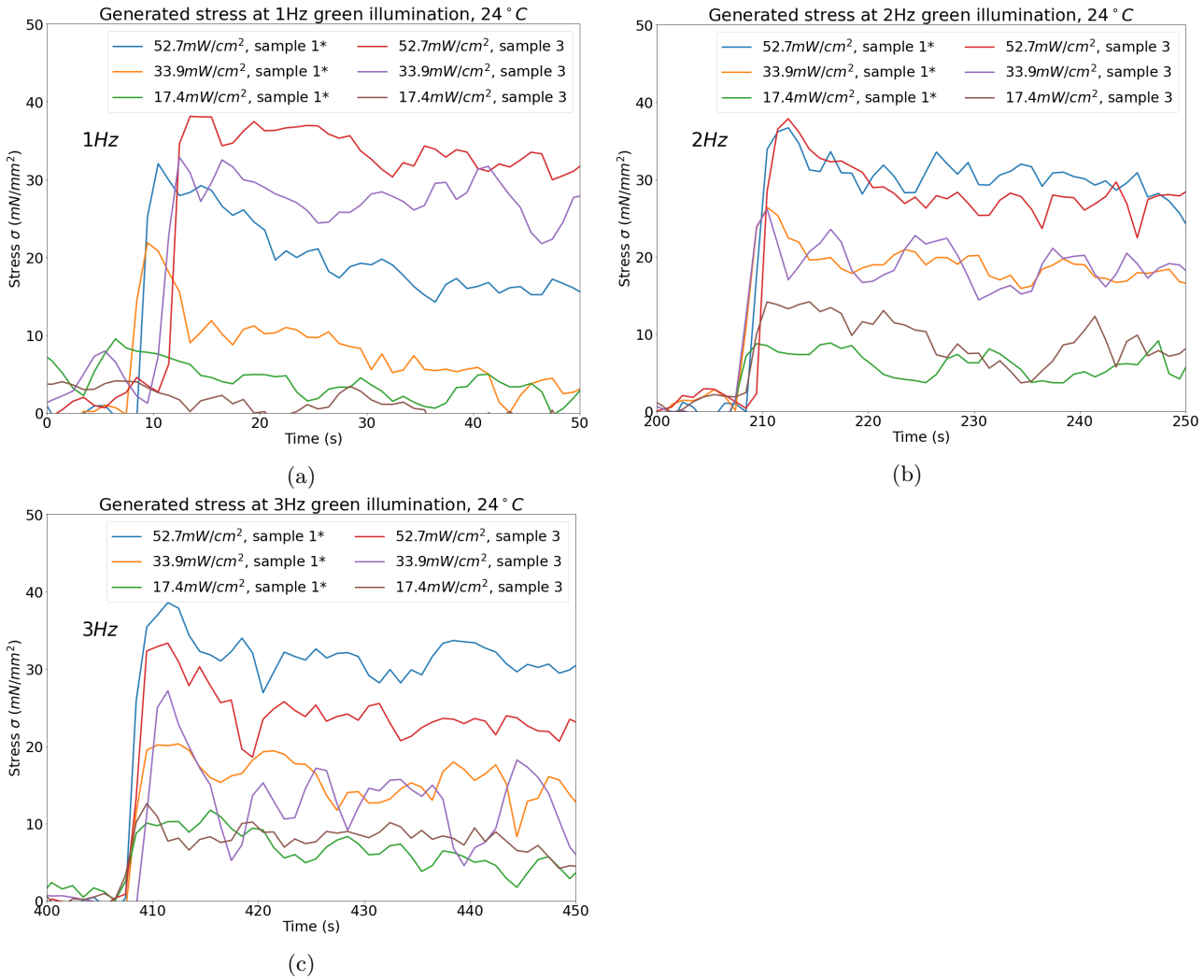

Figure 2.50: Generated stress upon illumination with a green LED at 1,2 and 3 Hz light pulses (50% duty cycle, 17.4-52.9mW/cm^2) in two samples of 27 and 32μm thickness.

Force vs. heat in 15s. illumination

In continuous illumination (15s.) we see that the maximum temperatures are reached after ±5s at each irradiance step (fig. 2.51). Temperature increases in a non-linear way, although we see the same linear trend at the start of heating as observed in short pulse lightning (2.49). **MM10 surface temperature and force generation coincide. We observe that the greater the magnitude of the stimulus (irradiance), the faster the stress generation.** This effect was also shown in other LCEs stimulated by electromagnetic fields instead of light [61]. The amount of radiant energy determines the amount of active azobenzene molecules. While the optomechanical part takes place fast (isomerization), the thermomechanical effect relies on thermodynamic effects; ie. how heat transfers through the material.

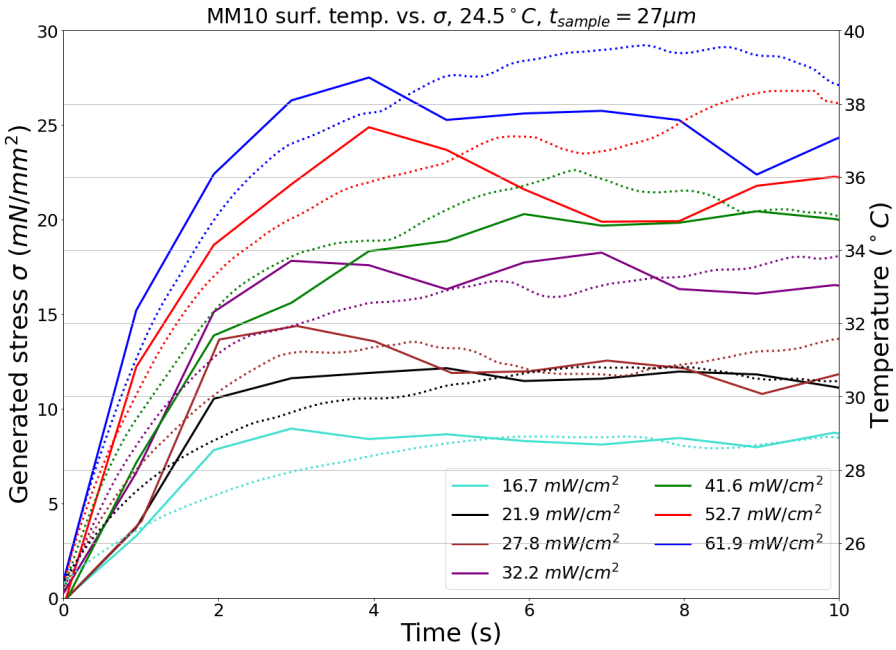

Figure 2.51: Rise in MM10 surface temperature upon illumination with a green LED at different irradiances (dotted lines), and corresponding generated stress (solid lines) at 24.5°C room temperature) Sample thickness: 27μm.

3 Mathematical Modeling of MM10 Force Generation

We try to fit our data to make an approximation of the generated stress (mN/mm^2) based on the sample thickness (μm) and the irradiance (mW/cm^2). It was observed that thicker samples perform worse (fig. 2.38). Generally, they generate fewer stress than thinner samples at the same irradiance. We hypothesize that this is due to penetration depth: One-sided illumination does not penetrate linearly into the material, and so the backside of an LCE strip is relatively underperforming. In a thick strip, this could even lead to a '*dead weight*', a part of the LCE where light does not penetrate at all and thus there will be almost no contraction in this part (maybe only in case of a prolonged stimulus, where the heating of the material generates a thermomechanical effect in this part).

According to the Beer-Lambert law of penetration depth of electromagnetic waves into a material, the intensity of a wave at depth z is:

$$I(z) = I_0 e^{-\alpha z}$$

Where $I(z)$ is the intensity at depth z, I_0 is the intensity before penetration in the material, and α is a coefficient dependent on the material characteristics.

We note from the Beer-Lambert law that the penetration of irradiance is not linearly dependent on the sample thickness, but (negatively) exponential. This relationship must be incorporated in our model. Furthermore, it can be argued that two-sided illumination is more effective than one-sided illumination at equal irradiance, because the absorption of light by MM10 is more efficient closer to the surface.

3.1 Deriving absorption coefficient *a*

The absorption coefficient a for MM10 reacting to the green LED beam was estimated by irradiating two samples with different thicknesses at different irradiances. The irradiance before hitting the sample (I_0) was measured and compared to the transmitted irradiance after the sample ($I(z)$). We neglect losses of irradiance through air and by doing so, $I(z)$ is the irradiance at the back surface of the MM10 sample (z is sample thickness in μm). We can then estimate a according to the Beer-Lambert Law.

We know that:

$$I_{(z)} = I_0 * e^{-az}$$

Where $I(z)$ and I_0 are the irradiances in mW/cm^2 and z is the sample thickness (μm). If we rewrite we will find that:

$$a = ln\left(\frac{I(z)}{I_0}\right) / -z$$

If we fill in the found values, we will find:

$I_0(mW/cm^2)$	$I(z=27.1)_{LCE1*}$	a_{LCE1*}	$I(z=32.3)_{LCE3}$	a_{LCE3}
6.53	0.64	0,0859	0.61	0,0732
15.19	1.42	0,0874	1.36	0,0747
28.50	2.63	0,0879	2.50	0,0753
33.93	3.10	0,0882	2.96	0,0755

We then take the average a for all of these measurements and then find absorption coefficient a:

Absorption coefficient *a* was measured:

$$a = 0.081 \pm 0.006$$

3.2 Model for predicting MM10 stress-generation

Now that we estimated the absorption coefficient, we can incorporate it in our model.

We know from earlier measurements that the average reflection of green light by the MM10 surface is around 5.53%. So we subtract this part from the initial irradiance I_0 to know the irradiance truly penetrating the MM10 surface (I_{eff}):

$$I_{eff} = 0.9447 \cdot I_0$$

We know that this irradiance I_{eff} is absorbed by the MM10 according to the Beer-Lambert law with absorption coefficient 0.081 at each depth z:

$$I_{(z)} = I_{eff} \cdot e^{-0.081 \cdot z}$$

We can then calculate the amount of I_{eff} that is absorbed by the MM10 by integrating this function from thickness 0 to the thickness of the sample t:

$$I_{abs} = I_{eff} \cdot \int_0^{t_{samp}} e^{-0.081 \cdot t}\, dt$$

Now, we can see that once the thickness is large enough, all irradiance entering the MM10 (I_{eff}) will be absorbed by the MM10, and so transmission through the sample will be 0.

We need to have a theoretical framework in place estimate how to adjust our model for sample thickness.

Theoretical assumptions regarding sample thickness

We observe in fig. 2.43 that the surface temperature of an homogeneously illuminated MM10 strip rises the fastest in the middle of the surface, and reaches the highest values there, compared to the edges of the surface. This can be explained by the heat transfer capacity of an MM10 strip. At the edges, more heat is conducted to the air, causing a slower rise in temperature, despite receiving the same irradiance as the surface middle part. We assume that this effect is also present in the depth dimension of the sample. Say we irradiate two strips, A and B, with the same irradiance. The strips have the same dimensions but a different thickness: $t_A > t_B$. When they receive the same amount of light energy, and they contain the same concentration of azobenzene molecules, the isomerization and heat production of the azobenzene molecules is equal in the upper layers of A and B. However, the thicker strip A has a bigger volume, and thus the heat production will be spread over a bigger volume than in B. This causes a slower temperature rise and a lower end-temperature in A than in B. This lower temperature means that A has a larger percentage of non-contracting volume (where the local temperature is below the transition temperature) than B. While the stress calculation is corrected for cross-sectional area, strip A will show a lower stress generation than B, as it is less efficient. Furthermore, the layers deep below the surface of a thick strip will produce (almost) no contraction because light does not penetrate there, and the local temperature stays below the phase transition temperature. When surface layers do contract, but deeper layers do not, the contraction force of the surface layers is absorbed by the deeper layers, causing the sample to bend. This bending causes less force registration at the clamps, and thus, lower stress is observed in thicker strips compared to thinner strips given the same irradiance. Thus, these deeper layers act as *dead weight* (fig. 3.1) We note from our experiments that the sample thickness lowers stress generation in a linear fashion (fig. 2.38).

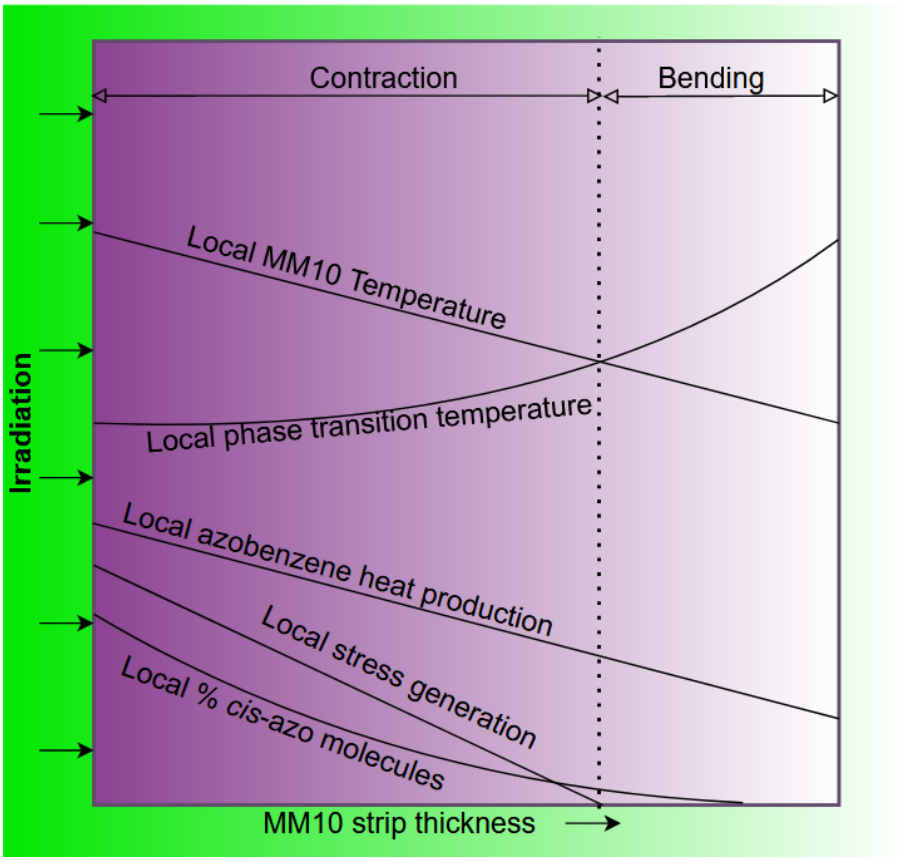

Figure 3.1: Simultaneous effects taking place in an MM10 strip illuminated from one side. If local MM10 temperature is below phase transition temperature, no local contraction will occur.

We therefore add thickness as a denominator in our function, so that the generated stress will go to zero once the sample will become extremely thick. This addition will also preserve the linear trend we observe in our experiments.

$$\sigma = \frac{I_{eff} \cdot \int_0^t e^{-0.081 \cdot t}\, dt}{t}$$

We also add a weighing factor A to compensate for other important factors on stress generation efficiency, mainly environmental temperature as we saw in fig. 2.41 (due to the fact that $24 - 38°C$ is within the *glass transition region*).

$$\sigma = \frac{A \cdot I_{eff} \cdot \int_0^t e^{-0.081 \cdot t}\, dt}{t}$$

We then tested different sizes for weighing factor A and found that the model aligned the closest to our experimental findings (at room temperature) when $A = 4.1$ (see fig. 3.2).

While stress has no time dimension but irradiance does, we take a 'snippet' out of the stress curve with a 1s duration so that we lose the time dimension in our model (fig 3.3).

We still keep the units stress (σ) and irradiance (I) for easy appliance of the model in the real world.

We find a model for estimating the generated stress by MM10 upon illumination:

$$\sigma = \frac{A \cdot (0.9447 \cdot I_0) \cdot \int_0^t e^{-0.081 \cdot t}\, dt}{t}$$

Where σ is the maximal generated stress (mN/mm^2), A is the weighing factor for influences such as environmental temperature ($A = 4.1$ at a room temperature of $\pm 24°C$), I_0 is the irradiance emitted by the (530nm)light source (mW/cm^2), and t is the sample thickness (μm).

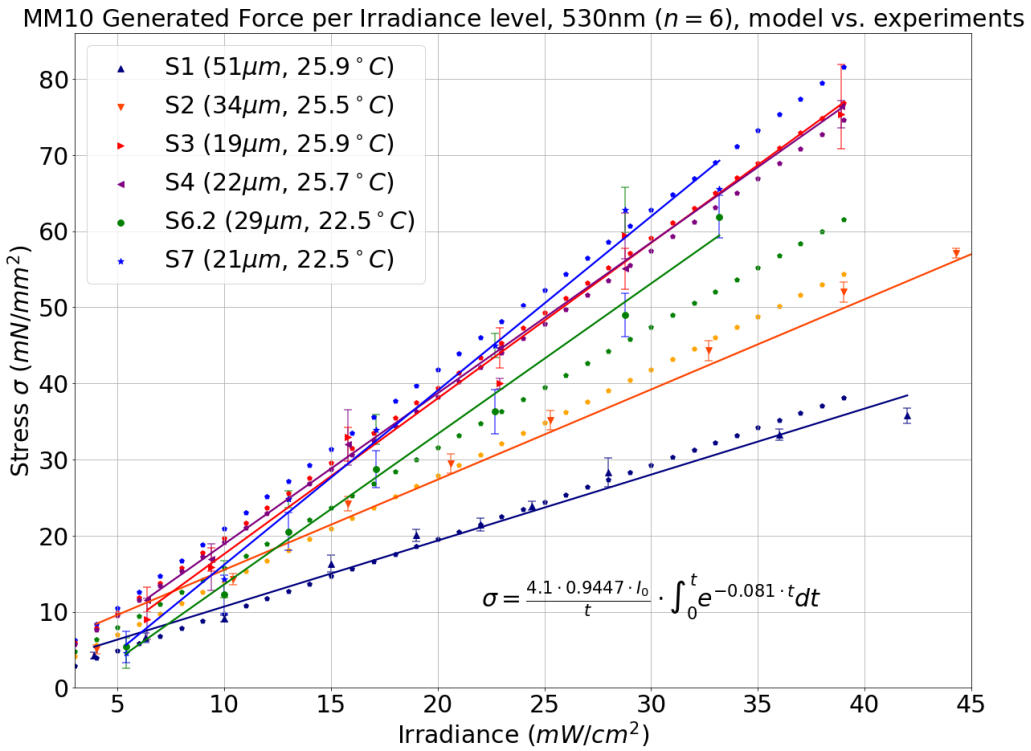

Figure 3.2: Approximation of experimental data with model function. Straight lines are the linear approximations of the experimental data (the semi-transparant markers). The dotted lines are the outcome of the model function per sample. The markers are the original measurements, each marker is the average of 12 measured points during a single contraction plateau

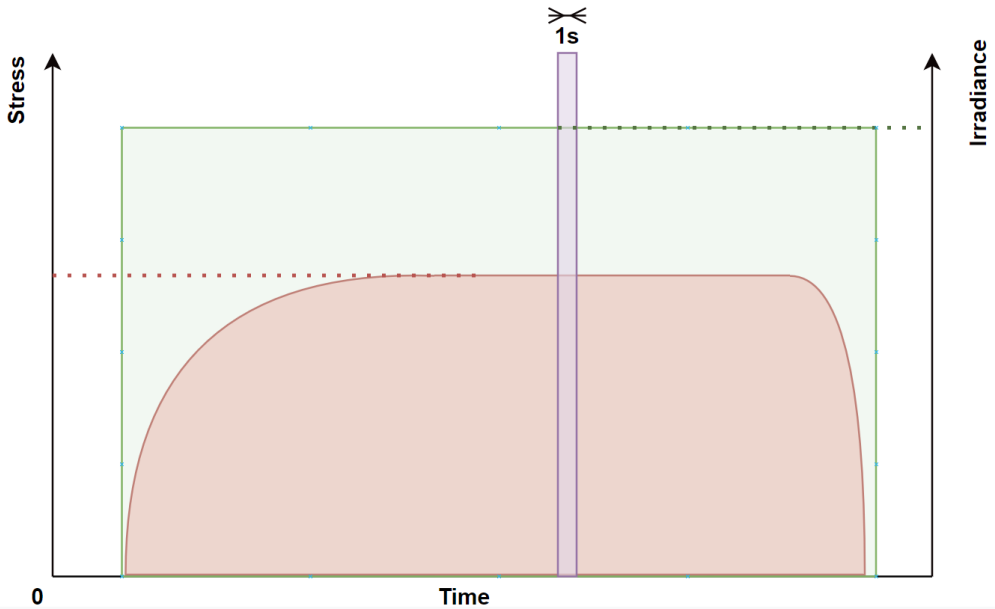

Figure 3.3: Graphical explanation for model. The model takes a 'snippet' out of the stress curve of 1s. duration (at the maximum stress plateau, reached after $\pm 5s$. Therefore the irradiance loses its time dimension ($mW/cm^2 => mJ/cm^2$) .

4 Proof of Concept Demonstrator

4.1 Proof of concept setup

We built a proof-of-concept setup to measure concentric stress generation of MM10 upon illumination (see Movies for the demonstrator in practice). A simpler version of this setup was mentioned in [55]. We expand on this setup to achieve homogeneous irradiance by building a flexible LED sheet, live ECG monitoring and activation of light by heartbeat. Also we provide high accuracy pressure measurement.

4.1.1 Control system

The control system (fig. 4.1) is connected to the power grid using a household plug and switch. The power then goes to four LED drivers (*ESST040E-0900-42*)[62] generating a power of 42V at 1A each. Each current source powers a row of 12 LEDs on the flexible sheet. The current sources are dimmed altogether by one analog 0-10V dimmer (*Luxdrive F019*) [63]. In between the current sources and the LED sheet, a on/off relay module is installed (*Velleman VMA 400*)[64] that enables the circuit to be turned on and off by Arduino control. A separate Arduino Uno was used for detection, as it fully eliminates signal interference from the relay module. Heart rate detection is used as input for the system (*AD8232 ECG sensor kit*)[65]. The bandwidth of the signal is $0.1 - 250Hz$ and the amplitude is between $50\mu V$ and $5mV$. This signal is scaled automatically in to a value between 0-1023. We then set an appropriate value (i.e. >600) to detect QRS complexes and use this signal to switch on the relay module (and thus the light) during a heart beat (see fig. 4.3). The balloon is connected to the pressure sensor module (*MPXV7002DP differential sensor*)[66], which can also be read out by the Arduino (measures up to 2kPa). A temperature and humidity sensor is placed inside the tube to monitor temperature and humidity during experiments (*Iduino DHT22*) [67]. Python and Arduino Create software were used to write the code and read-out ECG, pressure, temperature and humidity (see Appendix). The realtime data were registered using *PuTTY v.076* software. The result can be seen in fig. 4.2. To avoid the mechanical force of clicking relays on measurements, the relay module was placed hanging on rubber bands to the box walls. The system was built in a modular fashion so that the control unit can be easily inserted between the current source and the LED sheet, but the current source can also power the LED panel without the control unit in between..

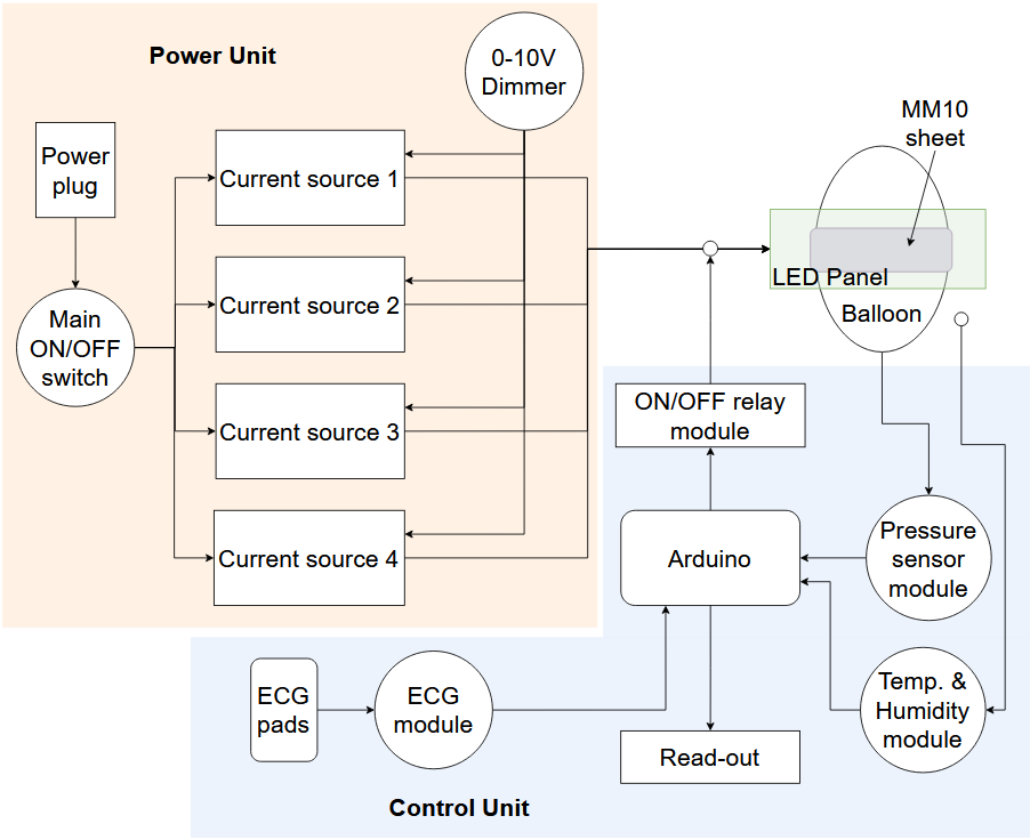

Figure 4.1: Schematic of control system used for flexible LED sheet illumination of an MM10-covered balloon.

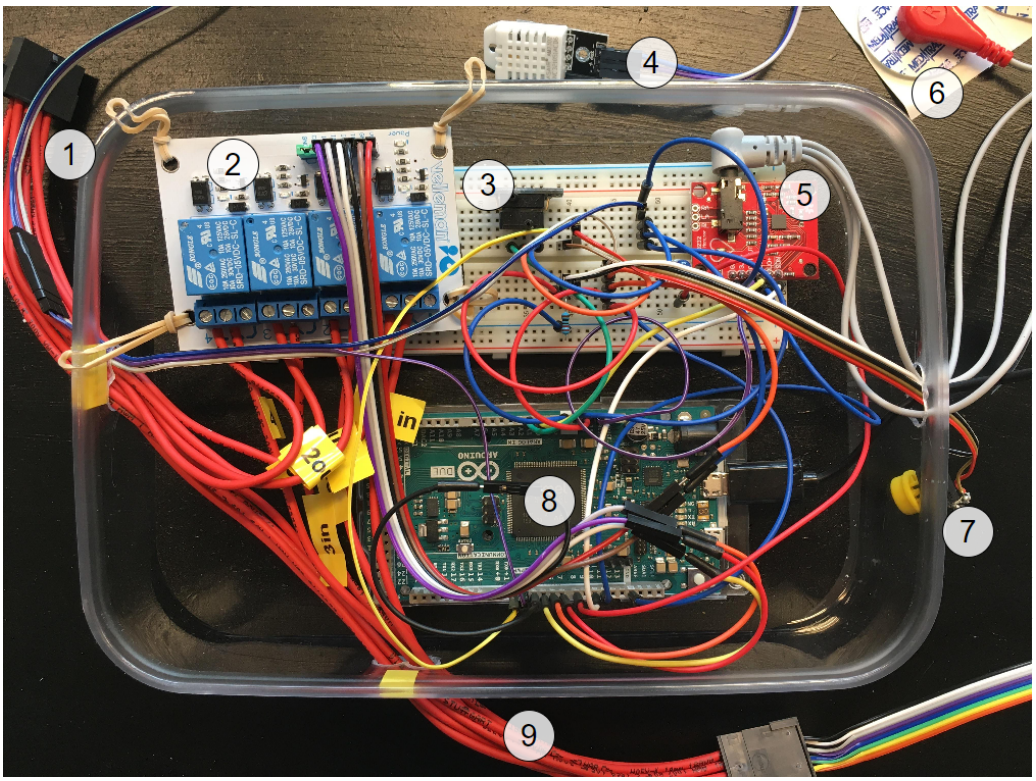

Figure 4.2: Overview of control unit. 1: Connection to power unit. 2: Relay module. 3: Pressure sensor. 4: Temperature and humidity sensor. 5: ECG module connected to ECG pads (6). 7: Manual on/off light button 8: Arduino Due with usb cable for read-out. 9: Connection to LED panel.

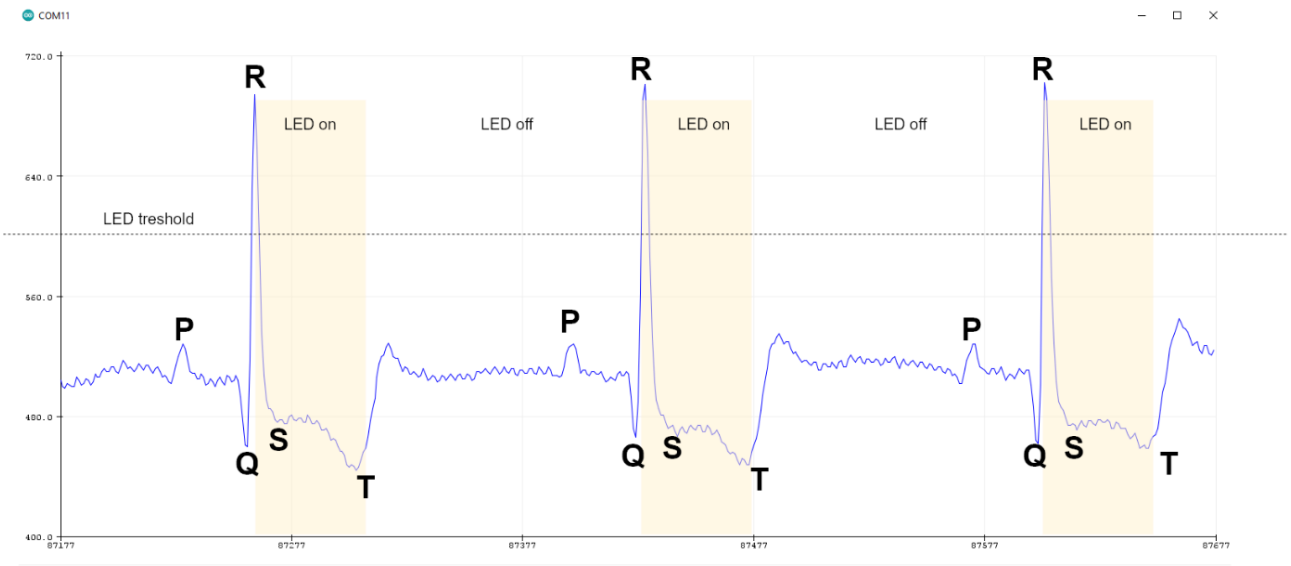

Figure 4.3: ECG signal obtained by placing the pads on the researcher. A clear 1-lead signal can be seen, displaying characteristic P-tops, QRS-complexes and ST-segments. The height of the R can be used to set a threshold for switching the LED on. See Movies for a live recording.

4.1.2 miniLED panel design

As our modeling showed, a hexagonal placement of LEDs gives the most homogeneous irradiance. Because flexible μLED sheets are still in developmental phase, we used miniLEDs instead. These are bigger but should be able to provide the homogeneous irradiance needed. A flexible polyimide LED sheet was designed in *Altium Designer* and produced by *PCBWay* (see fig. 4.4). The sheet has a size of 172x30 mm and a thickness of 0.1mm and consists of a connector area and a lightning area of 122x30 mm where 48 miniLEDs can be placed with an equal spacing of 10mm between adjacent LEDs (see fig. 4.5). As such, the panel can be used as a circular sheet

with a diameter of maximal (see fig. 4.6):

$$122/\pi = 38.8mm$$

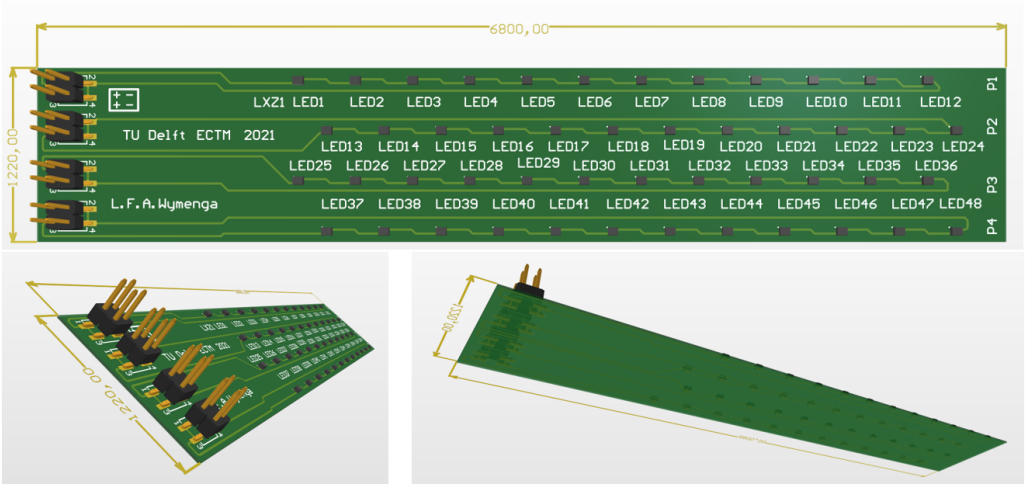

Figure 4.4: Altium Designer 3D-overview of flexible LED sheet. Size is noted in *mils* ($1mil = 0.0254mm$).

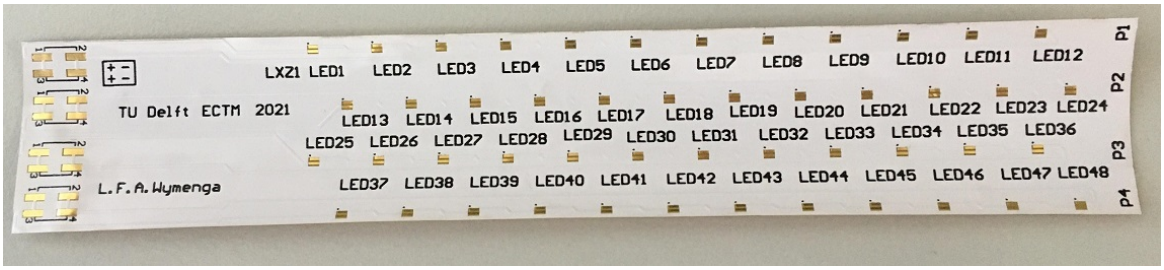

Figure 4.5: Flexible one-layer LED sheet design, with room for four 4-pin SMT connectors and 48 miniLEDs. Surface finish is made of immersion gold.

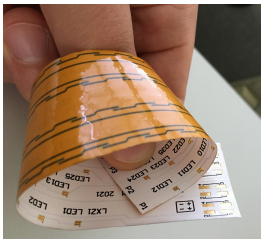

Figure 4.6: Flexibility of the LED-sheet.

Green miniLEDS *LumiLeds LXZ1-PM01* (530nm) were used with a forward voltage of $V_f = 3.27V$ and a size of 1.7x1.3mm [68]. The flexible LED sheet was taped on a metal carrier sheet with heat-resistant tape (see fig. 4.7). A metal stencil plate was placed over the sheet. After that, solder paste was applied over the stencil so that only paste is deposited on the spots on the LED sheet where components must be placed. The stencil was then removed and 48 miniLEDs and four connector pins were placed (Wurth 61000421121 4-pin SMT) [69]. Then, the sheet was placed into the oven and heated according to the temperature curve of the solder paste (up to $250°C$) for 4 minutes. After cooling, the sheet was taken out of the oven. The LEDs were tested per row by connecting a current source providing 30V at 0.1A (see fig. 4.7 bottom). After two times heating in the oven, and manual replacing one of the LEDs, we found that all 48 miniLEDs worked properly.

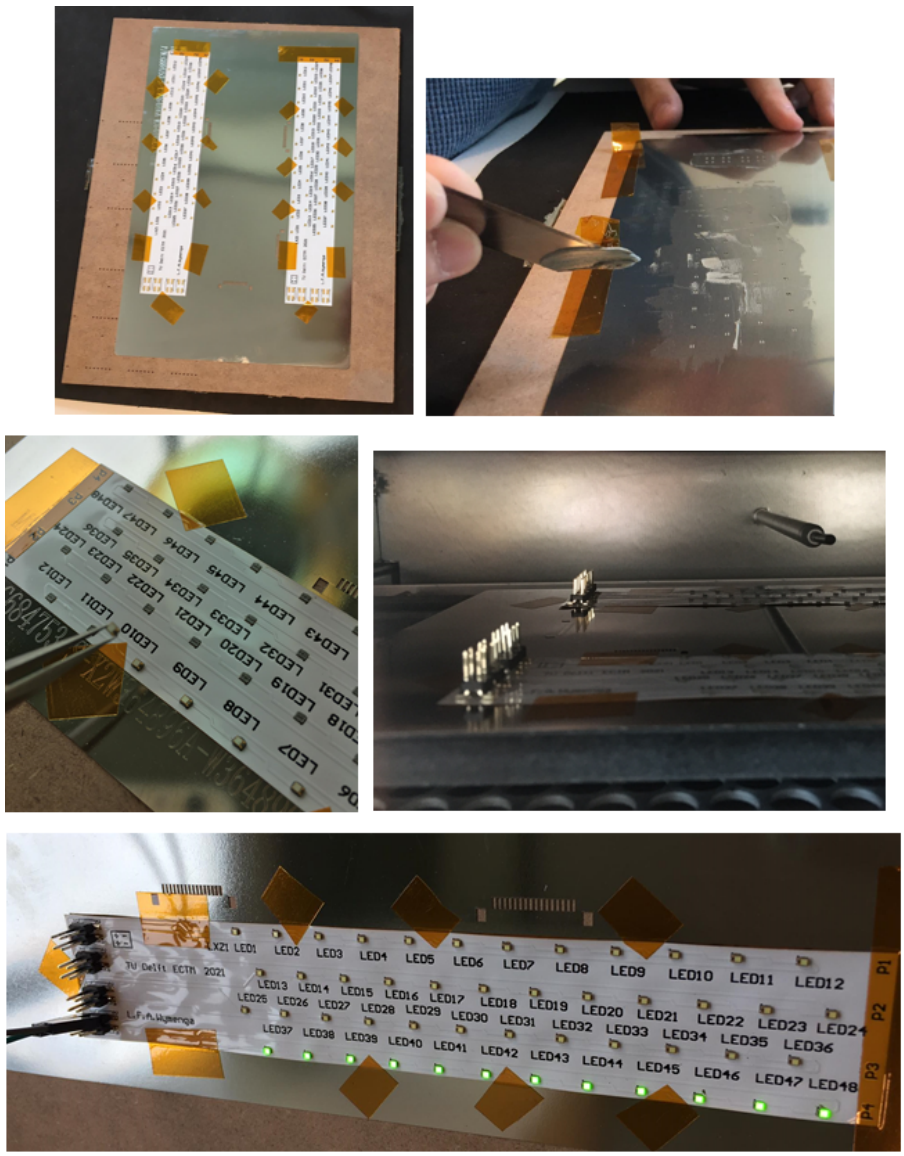

Figure 4.7: **Top left:** Placement of flexible sheets onto carrier, **Top right:** Filling holes through stencil with solder paste. **Middle left:** Placement of components, **Middle right:** Heating of LED panels for solder paste fixation. **Bottom :** Complete LED panel, testing of bottom row.

4.2 MM10 Concentric force measurement

The flexible LED panel was mounted in an aluminium tube with a diameter of 38mm, with a aluminium attached for heat conduction. Due to high current, it was found that the LED panel burns itself upon prolonged illumination (>few seconds). Therefore, the panel was attached to the tube with ZnO heat-conductive paste and heat-resistant tape (fig. 4.8). An aluminum donut-shape was placed around the tube to act as a heat sink. The bottom of the tube is partly open for wiring and this chimney design allows for inflow of cool air from the bottom and outflow of heat from the top.

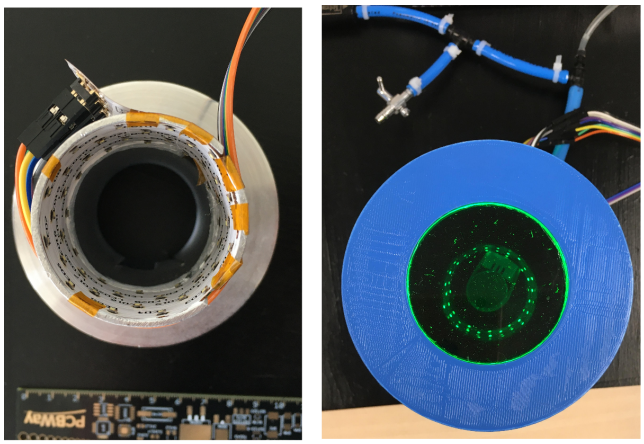

Figure 4.8: Left: Top view of LED panel in aluminium tube. Right: LED panel as seen trough polarizers. Inside the MM10-covered balloon and the temperature/humidity sensor are visible.

4.2.1 Light calibration inside tube

We measured the irradiance in the tube for reference and to check if the heat sink works. We placed our irradiance sensor in the tube, on 1cm from the edge, facing the LED sheet (fig. 4.9). Measurements were taken with the dimmer at three stances. It was found that after a short peak (1s.) the LED panel produced a very constant irradiance for more than 15s. (see fig. 4.10). This indicates that the heat sink works properly. Irradiance is stable after a rise time of 1000ms. in all three instances. After switching off the power, the irradiance turns to zero in a fall time of 1000ms.(see fig. 4.11). Three settings were chosen for optimal irradiance of MM10, as our earlier DMA contraction tests showed (35, 50 and 60mW/cm^2). Our setup is able to generate even higher irradiance, as the dimmer is only at 25% capacity at our highest setting.

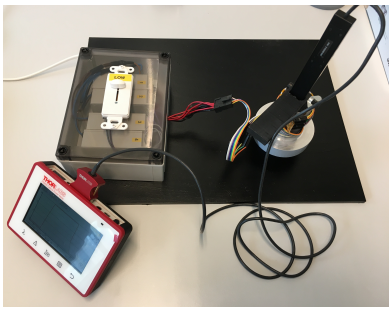

Figure 4.9: Measuring of irradiance inside the aluminium heat sink.

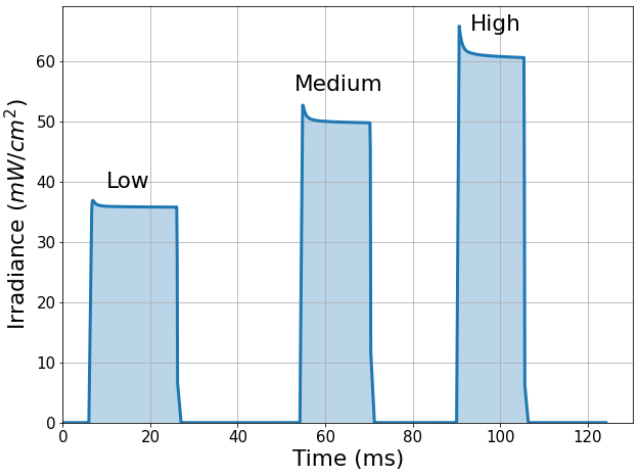

Figure 4.10: Irradiance measured inside the tube with varying dimmer settings.

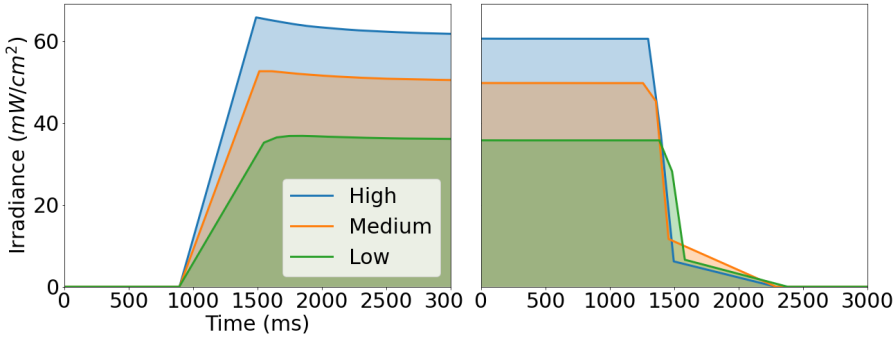

Figure 4.11: Rise and fall times of irradiance inside tube when light is turned on/off manually.

4.2.2 Air system and protection

A system of plastic tubes (*Festo*) was built (see fig. 4.12). The air system contains an inlet (for air injection with a syringe), an air release valve and a tube towards the pressure sensor. A one-way valve (*Tetra*) was applied behind the air inlets. A rubber cap covers the light for eye-protection. The cap is open on top and covered by two rings with linear polarizers. Hereby, the light which is let through is adjustable by rotating the rings. The temperature and humidity sensor was attached to the pipe below the balloon.

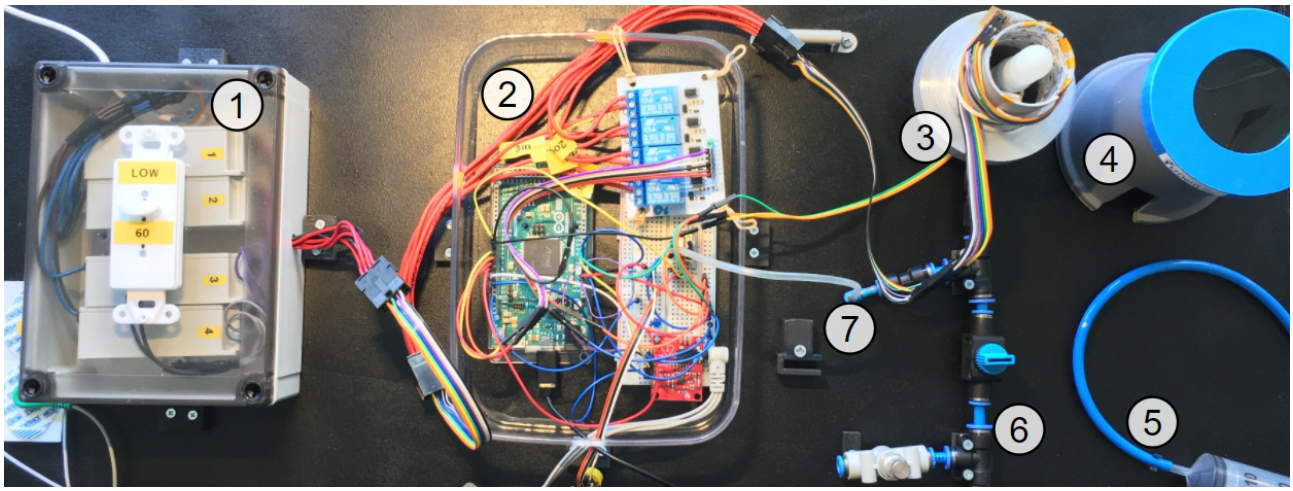

Figure 4.12: Air tube system, protective rubber cap with polarizers, and site for placement of MM10-covered balloon. 1: Power unit. 2: Control unit. 3: Tube with LED panel, balloon with temperature/humidity sensor inside. 4: Protective cap (to cover 3). 5: Air syringe. 6: Air inlet/outlet. 7: Air tube towards pressure sensor.

4.2.3 Concentric pressure measurement

Five MM10 bands ($50x5mm$, $\pm 20\mu m$ thick) were cut and glued. A band was tested by placing it gently around the balloon. After, air was injected in the system using a syringe. The pressure was raised manually to around 1100 Pa. At this pressure, the band was tightly clamped around the balloon, without breaking. The band was illuminated for 15s on / 15s off for 3-4 cycles. Mean pressure rise during illumination was calculated and compared to a control (irradiance of the balloon at 1100 Pa without an MM10 band applied).

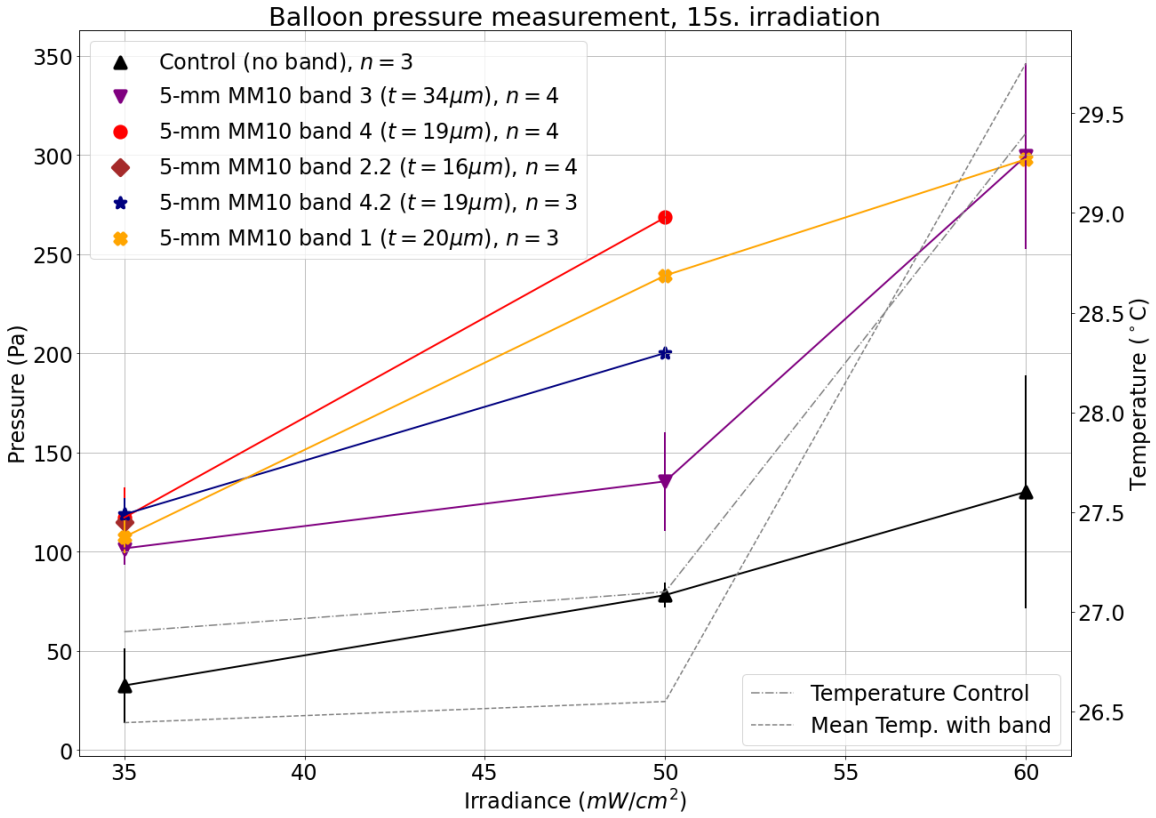

Figure 4.13: Pressure increase inside balloon upon illumination with and without an MM10 band wrapped around it.

It was found that the pressure in the balloon increases more when illuminated with an MM10 band ($t = 20\mu m$) applied than without (see fig. 4.13). We observe that the pressure does increase without a band applied upon illumination (control). Most likely, this is caused by LED heat production that expands the air inside the balloon. Temperature increases upon higher light intensities, and so does pressure in the balloon without a band applied, supporting this explanation (fig. 4.13). However, at similar temperatures, the pressure is increased 70-170Pa more when an MM10 band is applied, compared to control (dependent on light intensity, fig. 4.13). Therefore, this pressure rise must be due to the contraction force of the MM10 band. At an irradiance of $60mW/cm^2$, the pressure rise due to MM10 contraction is 170Pa higher than control. Sometimes, a sample would break, and then the subsequent pressure drop could be seen, as well as a lower pressure generation in the following light cycle (see fig. 4.14).

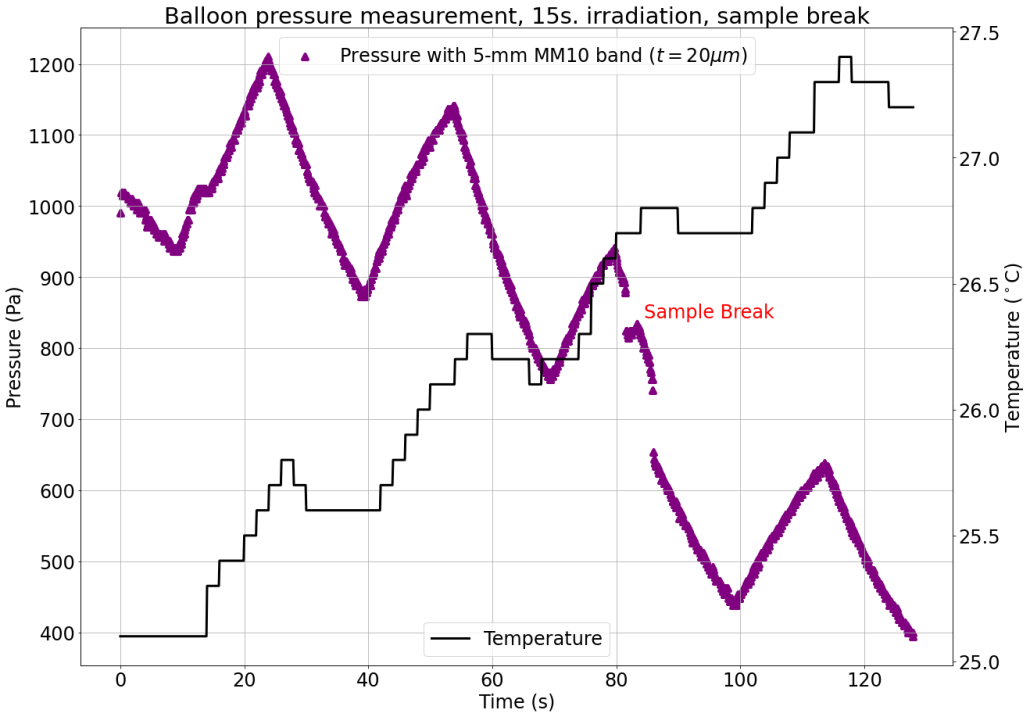

Figure 4.14: Breaking of an MM10 band wrapped around a balloon during illumination with an irradiance of $50mW/cm^2$ at the third light cycle. The pressure sensor notices a large pressure drop. Upon the fourth light cycle, the pressure generated is lower than in the first two cycles, when the band was still intact.

4.2.4 Efficiency

At the highest setting of $60mW/cm^2$ a pressure of 170 Pa was produced by a $5x0.5cm$ band of MM10 ($A = 2.5cm^2$). So, total energy deposited on the MM10 surface (in 15s.) is:

$$2.5 \cdot 60 \cdot 15 = 2.25J$$

At this setting, the current sources use only 25% of their maximum capacity (42W each). We have four current sources so total power used is estimated 42W. The height of the LED panel lightning area is 30mm but the MM10 band only receives light in an area of 5mm height. So, the LEDs really contributing to the MM10 illumination are using $5/30 \cdot 42 = 7W$ of power.The MM10 surface is receiving a total of $60mW/cm^2 \cdot 2.5cm^2 = 150mW$. As such, LED efficiency is:

$$0.15/7 * 100 = 2.14\%$$

The closed air system consists of three tubes with inner radius 3mm,2mm and 1.25mm and respective lengths of 115, 150 and 210mm. The balloon volume is calculated by modeling it as a cylinder of 30mm height and a 50mm circumference (7.96mm radius) with half a sphere on top of radius 7.96mm. The air volume in the system is then calculated to be:

$$(\pi \cdot 3^2 \cdot 115) + (\pi \cdot 2^2 \cdot 150) + (\pi \cdot 1.25^2 \cdot 210) + (\pi \cdot 7.96^2 \cdot 30) + (2/3 \cdot \pi \cdot 7.96^3 = 13.12cm^3$$

The pressure inside the system is acting on the inner surface area of the tubes and balloon. We calculate this area to be:

$$(2 \cdot \pi \cdot 1.25 \cdot 210) + (2 \cdot \pi \cdot 2 \cdot 150) + (2 \cdot \pi \cdot 1.25 \cdot 115) + (2 \cdot \pi \cdot 7.96 \cdot 30) + (2 \cdot \pi \cdot 7.96^2) + (\pi \cdot 1.25^2) = 7605mm^2$$

We know that:

$$F(N) = P(Pa) \cdot A(m^2)$$

So the force generated by the MM10 band (receiving $150mW$ of radiant energy) is:

$$F = 170 \cdot (7.61 \cdot 10^{-3}) = 1.29N$$

Ferrantini et al. [55] found similar concentric pressure generation (around $266Pa$) with a $20\mu m$ thick MM10 band wrapped around a latex condom. However, this band was stimulated only from one side with a high intensity laser ($50mW/mm^2$) for 200ms.

We estimate the maximum stress generated (σ) in our setup using a very rough equation for thin-walled cylinders:

$$\sigma = p \cdot r \cdot /h$$

Where r is the radius of our balloon ($r = 5cm/2 \cdot \pi$), h is the thickness of the sample ($t = 20\mu m$) and p is the generated pressure ($170Pa$). As such:

$$\sigma = 170 \cdot (0.05/2 \cdot \pi)/(20 \cdot 10^{-6}) = 68kPa = 68mN/mm^2$$

Which is of similar order as the result found in DMA testing.

4.2.5 Short pulse illumination

Pressure did not increase significantly upon light pulses of 200ms on / 800ms off (see fig. 4.15, 35-60mW/cm^2). This light cycle represents a heart rate of 60bpm. The same result was observed at a pulse duration of 500ms on / 500ms off (see fig. 4.16. It can be concluded that the response time of MM10 is too low at these intensities to produce a force in the short duration of a light pulse. Our earlier experiments showed that MM10 response time increases upon higher irradiance. However, MM10 becomes unstable and can break at irradiances above $\pm 60mW/cm^2$. This occurs especially when both ends of the MM10 sample are fixed, in other words, when there is external resistance against MM10 contraction. Pacing with 500ms pulses was tried on irradiance above $\pm 60mW/cm^2$, and no break occurred at $80mW/mm^2$ (see fig. 4.16). At maximum settings of the demonstrator, the intensity was above $120mW/cm^2$ 500ms pulses were given for a 15s period (yellow line in 4.16). Then, MM10 behaved as if there is 15s continuous illumination. In other words, MM10 is to slow to cool down at these intensities, and stays contracted while 500ms. pulses are given. **It can be concluded that MM10 does contract at intensities between 0-60mW/cm^2 during pulse illumination, and that response time is too slow to actively assist contraction at a normal heart rate.** Ferrantini et al. showed the generation of around 266Pa by use of a high intensity laser at a 200ms light pulse duration [55]. This laser had an intensity of $50mW/mm^2$, thus 83x higher than the intensity used in our experiment. While this laser experiment could make MM10 react fast enough to produce force at an illumination of 200ms, the force is very low, namely in the same range as our 15s illumination experiments with a 83x lower intensity. It can therefore be concluded that MM10 can produce force at the speed of a normal heart rate, but that the efficiency is very low. MM10 acts more efficiently when illuminated for longer periods, as the maximum response is seen after 5s.

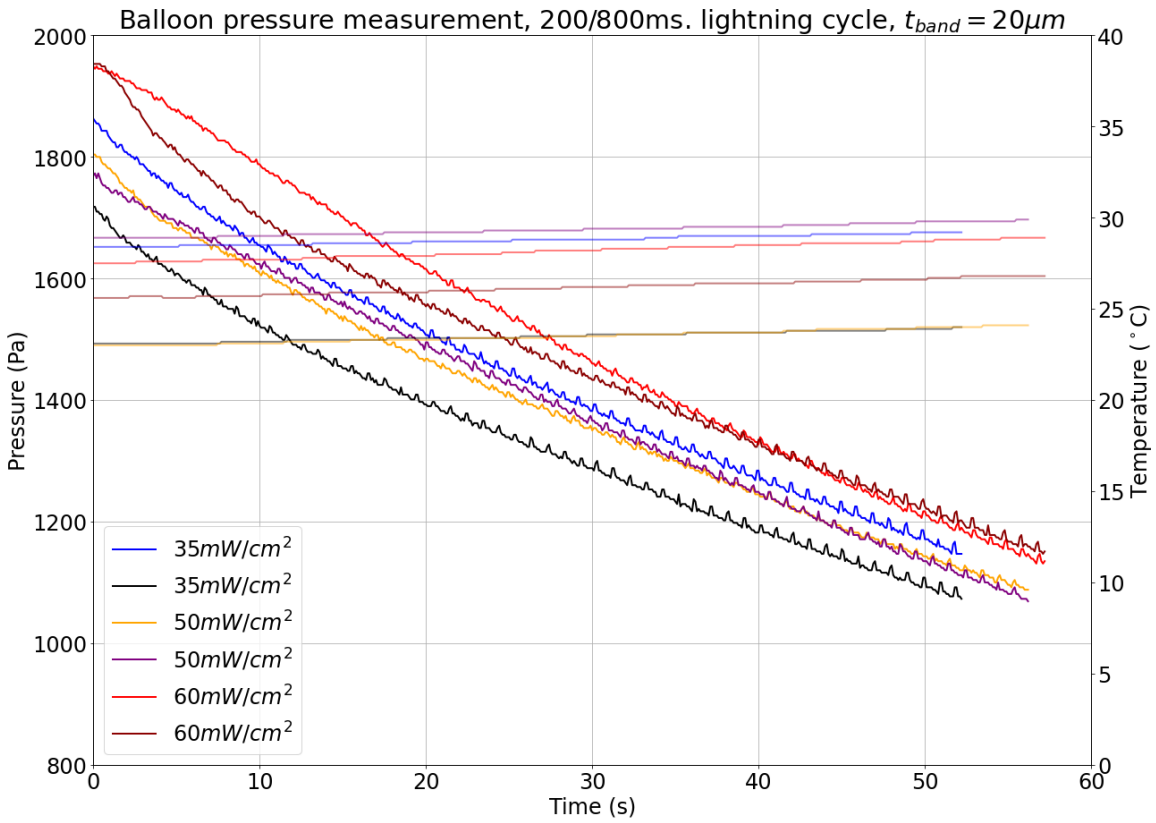

Figure 4.15: Green LED illumination of MM10 band wrapped around a balloon at 200ms pulses at different intensities. Measured pressure in balloon (thick lines). Temperature is measured by a sensor clamped underneath the balloon (translucent lines).

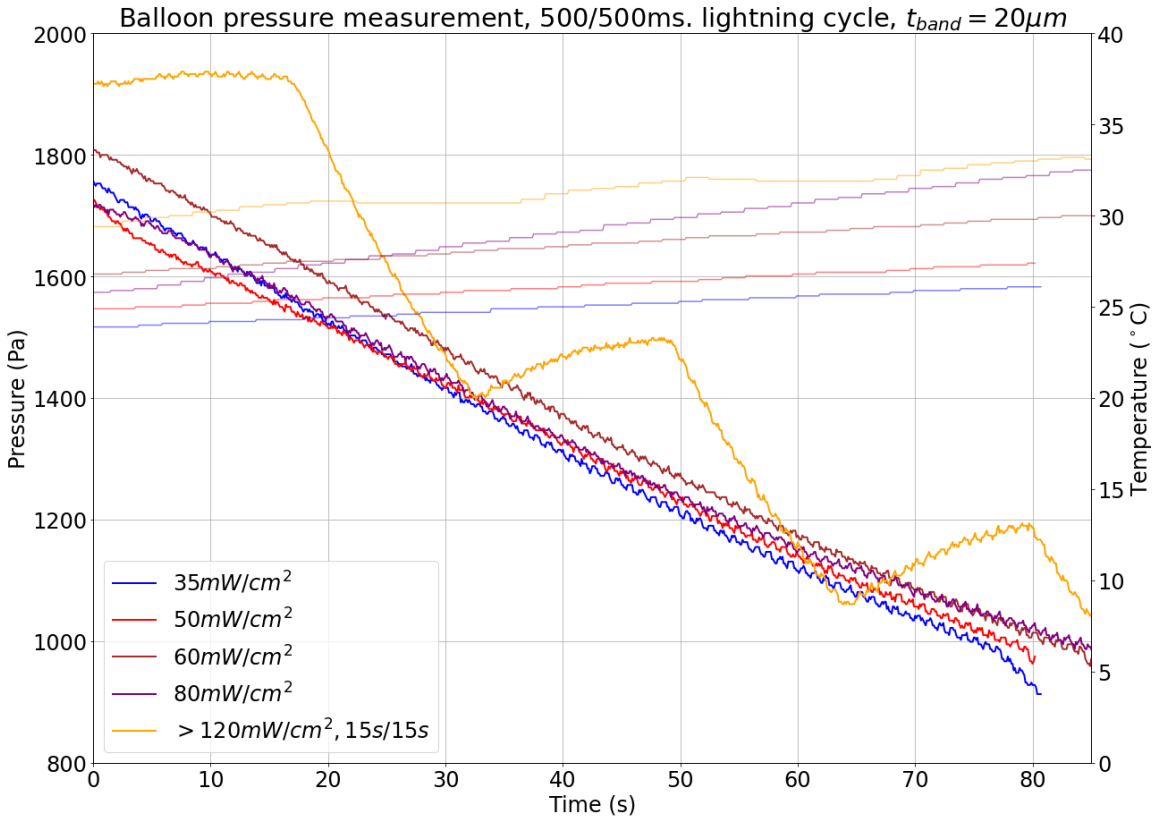

Figure 4.16: Green LED illumination of MM10 band wrapped around a balloon at 500ms pulses at different intensities. Measured pressure in balloon (thick lines).Temperature is measured by a sensor clamped underneath the balloon. 15/15: pulses were given at 15s intervals.

5 Conclusions

1. A hexagonal configuration of $\mu/mini$LEDs provides the most efficient and homogeneous irradiance on a surface perpendicular to the LEDs. (C1.5)
2. MM10 is a birefringent half-wave plate, meaning it rotates the polarization direction of light. This effect can be used to measure the order parameter and the nematic director of MM10, as the effect is the largest when the nematic director makes an angle of 45° with the polarizing direction when between crossed linear polarizers. Birefringence was measured to be between 0.015-0.025. The birefringence effect is wavelength-dependent and is the largest in the 700-800nm range. (C2.1)
3. Reflection and transmission of MM10 within the range of effective stress generation are resp. $5.5 \pm 0.2\%$ and $10.6 \pm 4.6\%$. This indicates that most of the LED light is absorbed, and thus can be converted in mechanical energy (stress-generation). (C2.1)
4. The elastomeric MM10 shows a $> 10x$ higher Young's modulus in the 0.1-2% strain range and a $> 4x$ higher modulus in the 4-6% strain range at $25°C$ compared to $37°C$. (C2.2)
5. A mathematical main-chain LCE model can be used to approximate the passive stress-strain behaviour of MM10 at different temperatures(C2.2): At $25°C$:
$$G(t) = 0.0021\left(\frac{\lambda_t}{1+2Q} - \frac{1}{(1-Q)\lambda_t^2}\right) + 0.0011\dot{\lambda}\left(\lambda_t^2 - \frac{1}{2\lambda_t^4}\right)$$
And at $37°C$:
$$G(t) = 0.0661\left(\frac{\lambda_t}{1+2Q} - \frac{1}{(1-Q)\lambda_t^2}\right) - 0.1247\dot{\lambda}\left(\lambda_t^2 - \frac{1}{2\lambda_t^4}\right)$$
6. Temperature has a much larger influence on MM10 stiffness and damping than frequency of the dynamical load. Because MM10 is tested in the glass-transition temperature range, the elasticity of MM10 is very much influenced by temperature changes. (C2.3)
7. When MM10 is irradiated, storage modulus decreases (up to -90%) and tan delta increases (up to +58%). This effect is bigger if the irradiance is increased and can be explained by MM10 contraction, causing the material to become stiffer. (C2.3)
8. MM10 has an order parameter of around 0.5. (C2.4)
9. MM10 performs best when there is low pre-strain (0.1%) applied. (C2.5)
10. MM10 (reactive to green light) and DR1-MM10 (reactive to blue light) have similar stress-generating capacity. Because blue LED light is more power efficient than green LED light, the (very new) DR1-MM10 has a lot of future potential. (C2.5)
11. MM10 has an absorption coefficient of $a = 0.081 \pm 0.006$ (C3.1)
12. MM10 stress generation ($\sigma, mN/mm^2$)can be precisely estimated by our model, which takes into account irradiance ($I_0, mW/cm^2$), sample thickness ($t, \mu m$), and environmental temperature (Where $A = 4.1$ at $24°C$, C3.2):
$$\sigma = \frac{A \cdot (0.9447 \cdot I_0) \cdot \int_0^t e^{-0.081 \cdot t}\, dt}{t}$$
13. MM10 stress generation is optimal in the 35-40mW/cm^2 irradiance range, producing a stress of up to $80mN/mm^2$ at $25°C$. At higher temperatures, elasticity will rapidly increase, leading to higher irradiance tolerance before break, but lower stress generation at the same irradiance compared to $25°C$. (C2.5)
14. When illuminated for 15s, MM10 reaches a new stable baseline temperature. This temperature increases linearly with the surface irradiance (C2.6)
15. While it is possible to pace MM10 at a rate of 1-3Hz without excessive heat build-up, MM10 has a too slow response to act as an effective contractile unit at light stimulus frequency of 1-3Hz. (C2.6)
16. MM10 surface temperature rises upon illumination, as an indirect result of the incorporated azobenzene molecules, which act as *micro-heaters*. Surface temperature reaches it's maximum after ± 5s. of illumination. Stress generation coincides with this temperature rise, until it reaches a plateau. (C2.6)
17. An MM10 band ($50x5mm, 20\mu m$ thick) can produce up to 170 Pa pressure when wrapped around a balloon and irradiated homogeneously with $60mW/cm^2$ green light. As such, the MM10 band generates a substantial force of $1.29N$. (C4.2)

5.1 Benefits and limitations, recommendations

An LCE-LED implanted patch could theoretically have many benefits compared to current treatments for heart failure. First of all, custom shape and size patches can be produced for individual hearts. LCE properties can be endlessly varied to achieve the perfect muscle-supporting structure. The stimuli (this thesis focuses on light) are controllable in magnitude, timing and direction. Bio-compatibility could allow long-term implants in contrast to LVADs. The patch material does not come into contact with the bloodstream, but is fixed on the outside of the heart, so no additional risk of blood clotting is assumed. External wireless control could be applied to regulate the contractile power of the patch, allowing adjustment to a patients' contractile function. LCE materials have shown to be able to support rat myocytes with a relatively high contractile power per area [1]. An LCE patch could be a long-term solution to enhance the contractile function of the ventricles. Thereby, the quality of life of AF and HF patients is improved while morbidity and mortality are lowered.

All implants, and so a μLED-sensitive LCE patch, pose infection risk. Though, it is shown that LCE has a very good biocompatibility in the human body. Tissue-material interactions have to be studied, because LCE material is shown to possess a scaffolding function for new tissue generation [44]. Also, in vitro cardiomyocyte growth speed on LCE scaffolds was enhanced compared to other regularly used substrates [34]. A possible solution in preventing tissue adhesion would be the covering of the LCE patch with a polymer layer such as PDMS. Bleeding risk will depend on how the device will be connected to the heart. Additional risks are breakage of μLEDs and interconnects, oxidation and release of harmful particles in the body. Damage to the cardiac tissue due to mechanical forces exerted by the patch cannot be excluded. Timing errors between the natural heart rate and the contraction of the patch can lead to opposite contractile movements and, in worst case scenario, a total blockade of heart contraction. These errors can originate in the control mechanism of the patch, the heart rate detection mechanism or somewhere in between. When LED light is used, heat is generated. Improper heat dissipation can damage both the cardiac tissue and the patch itself, but also influences MM10 performance greatly, as shown in this thesis. Stimulation of the LCE patch by present but unwanted stimuli in the body (changes in heat, pH, chemicals, electricity or movement) must be prevented.

We are aware that this thesis only describes very first steps in the characterization of the LCE *MM10* and its interaction with light. Concrete next steps in the research would be light stimulation of MM10 in a temperature controlled environment. The author of this thesis already made a LED panel that can be applied inside the furnace of a DMA machine. Interaction of LEDs very close to the MM10 material has to be studied. Our modeling shows that it is not necessary for μLEDs to touch the MM10 surface to provide high-intensity homogeneous irradiance to it. However, at very close distance ($\pm 20 \mu m$) direct heating of MM10 by LED heat production becomes a factor to account for. It is not clear what to expect: The direct heating of MM10 is not per definition bad for MM10 performance, because contraction is mainly stimulated by heat. As long as flexible LED layers are not flexible or thin enough, these layers have to be separated from MM10 layers to guarantee effective MM10 contraction. Otherwise all produced force will be absorbed by moving the flexible LED layer. As we notice that we are operating here on the edge of current science regarding flexible LED panels, it is assumed that the separation between LED layer and MM10 layer is here to stay for several more years. As such, this thesis and further research using a separate layers will stay relevant. We hold the opinion that it is very well possible to develop useful patient solutions with light source and MM10 separated.

MM10 is an extremely versatile material, and combined with an extremely versatile stimulant (light), possibilities are endless. Medical possibilities lie (in our opinion) in assisting arterial/venous contraction, bladder contraction (urine incontinence) and *micropumps* (for implantable drugs dosing systems or cerebral fluid regulation). The birefringence effect in MM10 could be used as light or strain sensors. The heart is an complex organ, with a fast, variable pace and contraction power, and a complex 3D-structure. As such, it is one of the more challenging organs to be assisted by MM10-based systems. However, looking at the large population of heart patients who would benefit from such assistance, this is a goal worth aiming for.

Bibliography

[1] Cecilia Ferrantini et al. "Development of Light-Responsive Liquid Crystalline Elastomers to Assist Cardiac Contraction". In: *Circulation research* 124.8 (2019), e44–e54. ISSN: 15244571. DOI: 10.1161/CIRCRESAHA.118.313889.

[2] https://igcsebiologynotes.weebly.com/the-structure-and-function-of-the-human-heart.html. *Heart Anatomy*.

[3] A Level Biology. *A Level Biology*. URL: https://alevelbiology.co.uk/wp-content/uploads/2019/11/The-Cardiac-cycle_2a-1024x787.png.

[4] https://www.brainkart.com/media/extra/8MEcy4a.jpg. *Cardiac Cycle 2*.

[5] Véronique L. Roger. "Epidemiology of heart failure". In: *Circulation Research* 113.6 (2013), pp. 646–659. ISSN: 00097330. DOI: 10.1161/CIRCRESAHA.113.300268.

[6] https://en.wikipedia.org/wiki/Heart_failure#/media/File:Right_side_heart_failure.jpg. *Heart Failure Image*.

[7] Emile C.A. Nyns et al. "An automated hybrid bioelectronic system for autogenous restoration of sinus rhythm in atrial fibrillation". In: *Science Translational Medicine* 11.481 (2019), pp. 1–12. ISSN: 19466242. DOI: 10.1126/scitranslmed.aau6447.

[8] https://rebelem.com/left-ventricular-assist-dev. *LVADS image*.

[9] Tianyi Jin. *EU REPAIR Consortium*. URL: repairheart.eu.

[10] Gigahertz-Optik. "Tutorial on Light Measurement Techniques". In: *Vacuum* (2002), pp. 157–198.

[11] Alex. Ryer. *Light measurement handbook*. International Light, 1997, p. 60. ISBN: 0965835693.

[12] https://imagine.gsfc.nasa.gov/science/toolbox/emspectrum1.html. *NASA: light spectrum and light waves Introduction*.

[13] C.I.E. "1988 CIE Luminous Efficiency Function". In: ().

[14] https://onlinelibrary.wiley.com/doi/pdf/10.1002/0470024275.app7. *Spectral luminous efficiency function*.

[15] Bok Y. Ahn et al. "Omnidirectional printing of flexible, stretchable, and spanning silver microelectrodes". In: *Science* 323.5921 (2009), pp. 1590–1593. ISSN: 00368075. DOI: 10.1126/science.1168375.

[16] Jiangxin Wang and Pooi See Lee. "Progress and Prospects in Stretchable Electroluminescent Devices". In: *Nanophotonics* 6.2 (2017), pp. 435–451. ISSN: 21928614. DOI: 10.1515/nanoph-2016-0002.

[17] Chul Ho Lee et al. "Flexible inorganic nanostructure light-emitting diodes fabricated on graphene films". In: *Advanced Materials* 23.40 (2011), pp. 4614–4619. ISSN: 09359648. DOI: 10.1002/adma.201102407.

[18] Hao Zhang and John A. Rogers. "Recent Advances in Flexible Inorganic Light Emitting Diodes: From Materials Design to Integrated Optoelectronic Platforms". In: *Advanced Optical Materials* 7.2 (2019), pp. 1–27. ISSN: 21951071. DOI: 10.1002/adom.201800936.

[19] Matthew S. White et al. "Ultrathin, highly flexible and stretchable PLEDs". In: *Nature Photonics* 7.10 (2013), pp. 811–816. ISSN: 17494885. DOI: 10.1038/nphoton.2013.188.

[20] "HBLEDs". In: *$https://www.electronics-notes.com/articles/electronic_components/diode/light-emitting-diode-led-high-brightness-power-hbled.php$* ().

[21] Jeffrey M. Pietryga et al. "Spectroscopic and device aspects of nanocrystal quantum dots". In: *Chemical Reviews* 116.18 (2016), pp. 10513–10622. ISSN: 15206890. DOI: 10.1021/acs.chemrev.6b00169.

[22] Instrument Systems. "Handbook of LED Metrology". In: *Instrument Systems GmbH* (2000). URL: http://www.instrumentsystems.com/fileadmin/editors/downloads/Products/LED_Handbook_e.pdf%5Cnhttp://scholar.google.com/scholar?hl=en&btnG=Search&q=intitle:Handbook+of+LED+Metrology#0.

[23] E. Fred Schubert and Jong Kyu Kim. "Solid-state light sources getting smart". In: *Science* 308.5726 (2005), pp. 1274–1278. ISSN: 00368075. DOI: 10.1126/science.1108712.

[24] Haicheng Li et al. "Flexible and stretchable inorganic optoelectronics". In: *Optical Materials Express* 9.10 (2019), p. 4023. ISSN: 2159-3930. DOI: 10.1364/ome.9.004023.

[25] John A. Rogers, Takao Someya, and Yonggang Huang. "Materials and mechanics for stretchable electronics". In: *Science* 327.5973 (2010), pp. 1603–1607. ISSN: 00368075. DOI: 10.1126/science.1182383.

[26] Ivan Moreno. "LED irradiance pattern at short distances". In: *Applied Optics* 59.1 (2020), p. 190. ISSN: 1559-128X. DOI: 10.1364/ao.59.000190.

[27] https://www.rp-photonics.com/lambertian_emitters_and_scatterers.html. *Lambertian Emitters, RP Photonics*.

[28] https://www.researchgate.net/figure/Four-examples-of-surface-reflectance-a-Lambertian-reflectance-b-non-Lambertian_fig1_265157303. *Lambertian Emitter examples, RP Photonics*.

[29] Meie Li, Shan Lv, and Jinxiong Zhou. "Photo-thermo-mechanically actuated bending and snapping kinetics of liquid crystal elastomer cantilever". In: *Smart Materials and Structures* 23.12 (2014). ISSN: 1361665X. DOI: 10.1088/0964-1726/23/12/125012.

[30] N. Torras et al. "Bending kinetics of a photo-actuating nematic elastomer cantilever". In: *Applied Physics Letters* 99.25 (2011), pp. 1–4. ISSN: 00036951. DOI: 10.1063/1.3670502.

[31] Pierre-Gilles de GENNES. "Un muscle artificiel semi-rapide". In: *C. R. Acad. Sci. Paris* II.6 (1997), pp. 343–348.

[32] Daniele Martella et al. "Photonic Microhand with Autonomous Action". In: *Advanced Materials* 29.42 (2017), pp. 1–8. ISSN: 15214095. DOI: 10.1002/adma.201704047.

[33] Daniele Martella et al. "Self-Regulating Capabilities in Photonic Robotics". In: *Advanced Materials Technologies* 4.2 (2019), pp. 1–12. ISSN: 2365709X. DOI: 10.1002/admt.201800571.

[34] Daniele Martella et al. "Liquid Crystalline Networks toward Regenerative Medicine and Tissue Repair". In: *Small* 13.46 (2017), pp. 1–8. ISSN: 16136829. DOI: 10.1002/smll.201702677.

[35] Daniele Martella et al. "Opposite self-folding behavior of polymeric photoresponsive actuators enabled by a molecular approach". In: *Polymers* 11.10 (2019), pp. 1–13. ISSN: 20734360. DOI: 10.3390/polym11101644.

[36] S. Nocentini et al. "Beam steering by liquid crystal elastomer fibres". In: *Soft Matter* 13.45 (2017), pp. 8590–8596. ISSN: 17446848. DOI: 10.1039/c7sm02063e. URL: http://dx.doi.org/10.1039/C7SM02063E.

[37] Eric M.M. Tan et al. "Fast photodynamics of azobenzene probed by scanning excited-state potential energy surfaces using slow spectroscopy". In: *Nature Communications* 6 (2015). ISSN: 20411723. DOI: 10.1038/ncomms6860.

[38] Murilo L. Tiago, Sohrab Ismail-Beigi, and Steven G. Louie. "Photoisomerization of azobenzene from first-principles constrained density-functional calculations". In: *Journal of Chemical Physics* 122.9 (2005). ISSN: 00219606. DOI: 10.1063/1.1861873.

[39] S. S. Petrova, N. M. Chichinadze, and V. G. Shaverdova. "Kinetics of the weigert effect in azo dyes embedded in polymeric matrices with different activities". In: *Technical Physics* 50.2 (2005), pp. 227–231. ISSN: 10637842. DOI: 10.1134/1.1866440.

[40] D. Martella et al. "Light activated non-reciprocal motion in liquid crystalline networks by designed microactuator architecture". In: *RSC Advances* 7.32 (2017), pp. 19940–19947. ISSN: 20462069. DOI: 10.1039/c7ra03224b.

[41] Xinlei Pang et al. "Ultralarge Contraction Directed by Light-Driven Unlocking of Prestored Strain Energy in Linear Liquid Crystal Polymer Fibers". In: *Advanced Functional Materials* 30.32 (2020), pp. 1–8. ISSN: 16163028. DOI: 10.1002/adfm.202002451.

[42] Jaume Garcia-Amorós et al. "Fastest non-ionic azo dyes and transfer of their thermal isomerisation kinetics into liquid-crystalline materials". In: *Chemical Communications* 52.29 (2016), pp. 5132–5135. ISSN: 1364548X. DOI: 10.1039/c6cc00403b.

[43] Hao Zeng et al. "Self-Regulating Iris Based on Light-Actuated Liquid Crystal Elastomer". In: *Advanced Materials* 29.30 (2017), pp. 1–7. ISSN: 15214095. DOI: 10.1002/adma.201701814.

[44] Daniele Martella et al. "Liquid Crystal-Induced Myoblast Alignment". In: *Advanced Healthcare Materials* 8.3 (2019), pp. 1–10. ISSN: 21922659. DOI: 10.1002/adhm.201801489.

[45] Rob Verpaalen. *Stimuli-Responsive Commodity Polymers*. september. 2020, p. 2020. ISBN: 9789038650470.

[46] Jean E. Marshall and Eugene M. Terentjev. "Photo-sensitivity of dye-doped liquid crystal elastomers". In: *Soft Matter* 9.35 (2013), pp. 8547–8551. ISSN: 1744683X. DOI: 10.1039/c3sm51091c.

[47] Rob C.P. Verpaalen et al. "Fast, Light-Responsive, Metal-Like Polymer Actuators Generating High Stresses at Low Strain". In: *Matter* 2.6 (2020), pp. 1522–1534. ISSN: 25902385. DOI: 10.1016/j.matt.2020.03.001. URL: https://doi.org/10.1016/j.matt.2020.03.001.

[48] Xinlei Pang et al. "Ultralarge Contraction Directed by Light-Driven Unlocking of Prestored Strain Energy in Linear Liquid Crystal Polymer Fibers". In: *Advanced Functional Materials* 30.32 (Aug. 2020). ISSN: 16163028. DOI: 10.1002/adfm.202002451.

[49] Chongyu Zhu et al. “Dynamic Interfacial Regulation by Photodeformable Azobenzene-Containing Liquid Crystal Polymer Micro/Nanostructures”. In: *Langmuir* 36.24 (2020), pp. 6611–6625. ISSN: 15205827. DOI: 10.1021/acs.langmuir.0c00582.

[50] Tariel D. Ebralidze, Nadia A. Ebralidze, and Murad A. Bazadze. “Weigert’s effect mechanism observed in dyes”. In: *Applied Optics* 41.1 (2002), p. 78. ISSN: 0003-6935. DOI: 10.1364/ao.41.000078.

[51] Daniele Martella et al. “Polarization-dependent deformation in light responsive polymers doped by dichroic dyes”. In: *Soft Matter* 15.6 (2019), pp. 1312–1318. ISSN: 17446848. DOI: 10.1039/c8sm01954a.

[52] Stefano Palagi et al. “Structured light enables biomimetic swimming and versatile locomotion of photoresponsive soft microrobots”. In: *Nature Materials* 15.6 (2016), pp. 647–653. ISSN: 14764660. DOI: 10.1038/nmat4569.

[53] D. Martella et al. “Light activated non-reciprocal motion in liquid crystalline networks by designed microactuator architecture”. In: *RSC Advances* 7.32 (2017), pp. 19940–19947. ISSN: 20462069. DOI: 10.1039/c7ra03224b. URL: http://dx.doi.org/10.1039/C7RA03224B.

[54] Hao Zeng et al. “High-resolution 3d direct laser writing for liquid-crystalline elastomer microstructures”. In: *Advanced Materials* 26.15 (2014), pp. 2319–2322. ISSN: 15214095. DOI: 10.1002/adma.201305008.

[55] Cecilia Ferrantini et al. *SUPPLEMENTAL MATERIAL Development of light-responsive liquid crystalline elastomers to assist cardiac contraction*. Tech. rep.

[56] Devesh Mistry et al. “Isotropic Liquid Crystal Elastomers as Exceptional Photoelastic Strain Sensors”. In: *Macromolecules* 53.10 (2020), pp. 3709–3718. ISSN: 15205835. DOI: 10.1021/acs.macromol.9b02456.

[57] Paul Tipler and Gene Mosca. *Physics for Scientists and Engineers*. 6th ed.

[58] Nikon. “Principles of Birefringence”. In: *MicroscopyU - Introduction to Optical Birefringence* (2018), pp. 1–11.

[59] GlobalSpec.com. *Polymer Behaviour*. URL: https://insights.globalspec.com/article/7810/how-to-perform-tensile-testing-on-polymers.

[60] ASTM International. *Standard Test Methods for Vulcanized Rubber and Thermoplastic Elastomers — ASTM412-16*. Tech. rep. 2009, pp. 1–14. DOI: 10.1520/D0412-16.2.

[61] Atsushi Fukunaga et al. “Dynamics of electro-opto-mechanical effects in swollen nematic elastomers”. In: *Macromolecules* 41.23 (2008), pp. 9389–9396. ISSN: 00249297. DOI: 10.1021/ma801639j.

[62] ERP Power. “ESS / ESST Series 6 to 40 W Constant Current LED Drivers Datasheet”. In: ().

[63] Luxdrive. “F019 Low Voltage Dimming Control Datasheet”. In: ().

[64] Velleman. “4-Channel Relay Module User Manual”. In: ().

[65] How2electronics.com. *AD8232 ECG Sensor & Arduino Interfacing with ECG Graph Manual*. 2020. URL: https://how2electronics.com/ecg-monitoring-with-ad8232-ecg-sensor-arduino/.

[66] Freescale Semiconductor. *MPXV7002 Datasheet*. 2009.

[67] Joy-IT. *SEN-DHT22 Temperature and humidity sensor Datasheet*. Tech. rep.

[68] LumiLeds. *LUXEON Z Color Line Datasheet*.

[69] Wurth Elektronik. *61000421121 SMT 4-way connector Datasheet*.

Appendix

A.1 μLED modelling

A.1.1 Spacing between μLEDs

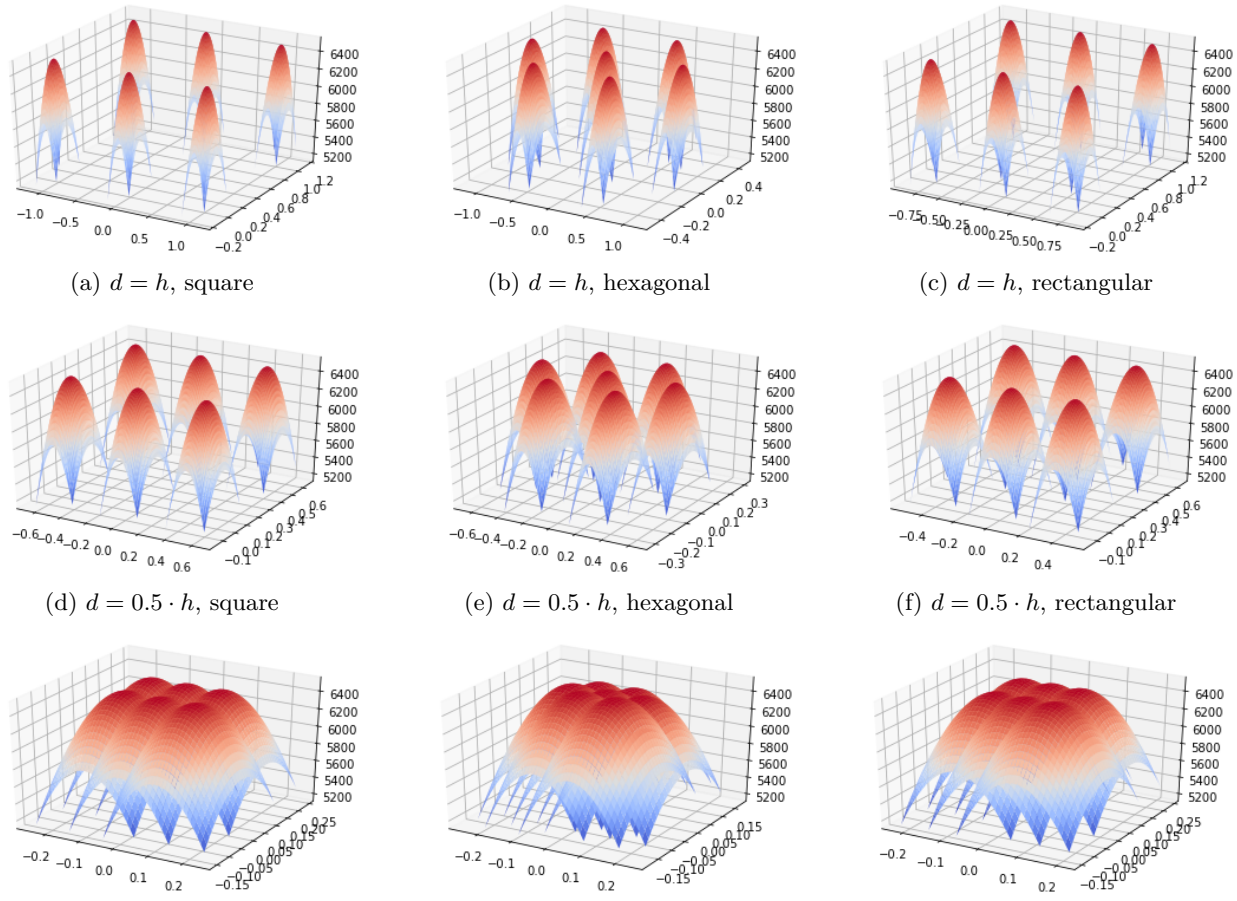

(a) $d = h$, square (b) $d = h$, hexagonal (c) $d = h$, rectangular

(d) $d = 0.5 \cdot h$, square (e) $d = 0.5 \cdot h$, hexagonal (f) $d = 0.5 \cdot h$, rectangular

(g) $d = 0.1 \cdot h$, square (h) $d = 0.1 \cdot h$, hexagonal (i) $d = 0.1 \cdot h$, rectangular

Figure A.1: 3D-Modelling of irradiance patterns of μLEDs in a square, rectangular and hexagonal formation. Square and rectangular formations contain 6 LEDs each, hexagonal formation contains 7 LEDs. Irradiance pattern is shown for a flat surface $h = 1mm$ above the LED surface and varying distances d between the LEDs. The model at $d = 0.1 \cdot h$ is practically not possible because the distance is then smaller than the individual LED dimension.

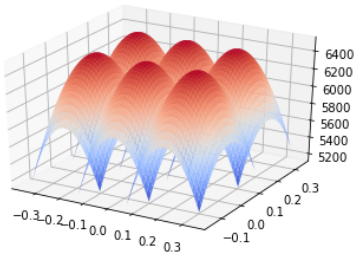

(a) $d = h$, square

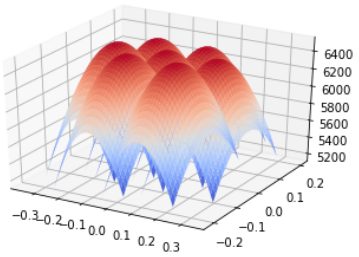

(b) $d = h$, hexagonal

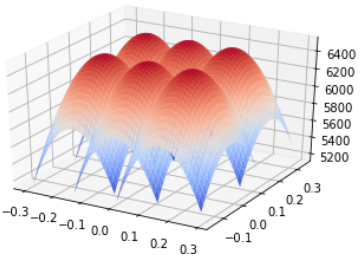

(c) $d = h$, rectangular

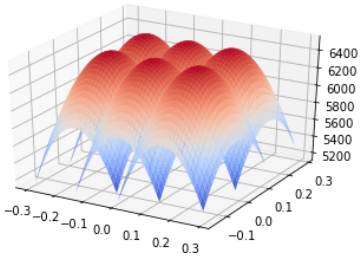

(d) $d = 0.735 \cdot h$, square

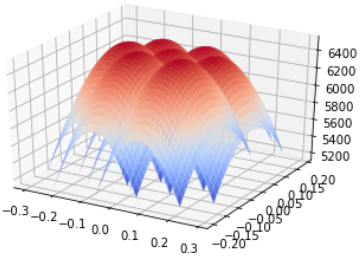

(e) $d = 0.735 \cdot h$, hexagonal

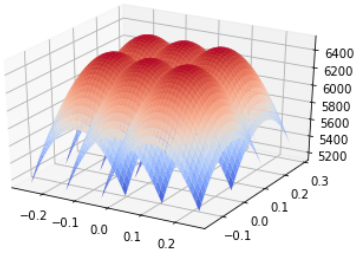

(f) $d = 0.735 \cdot h$, hexagonal

Figure A.2: 3D-Modelling of μLEDs in a square, rectangular and hexagonal formation. Square and rectangular formations contain 6 LEDs each, hexagonal formation contains 7 LEDs. Irradiance pattern is shown for a flat surface $h = 200\mu m$ above the LED surface, varying distances between the LEDs.

A.1.2 2D μLED modelling: sum of irradiation

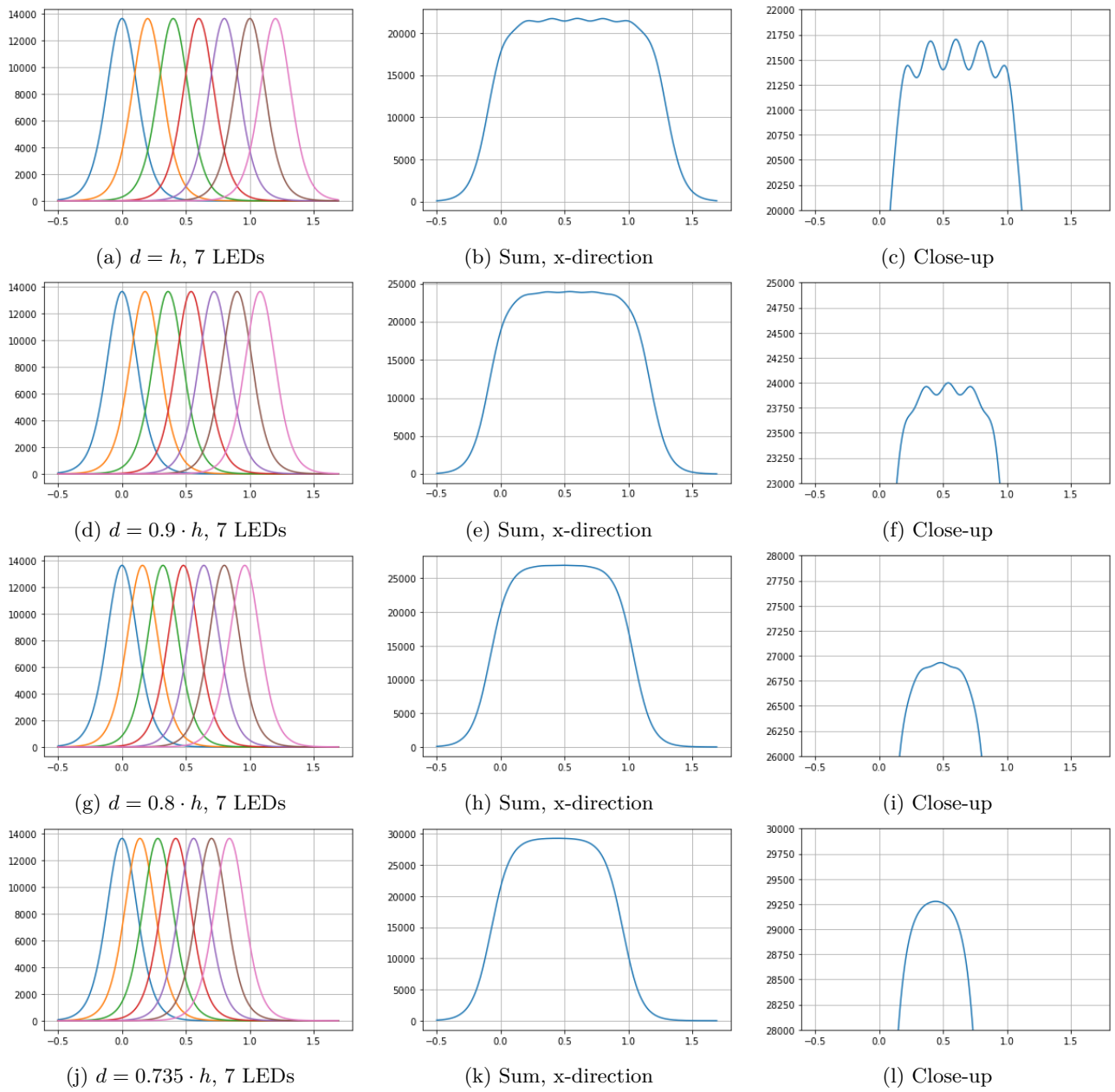

(a) $d = h$, 7 LEDs (b) Sum, x-direction (c) Close-up

(d) $d = 0.9 \cdot h$, 7 LEDs (e) Sum, x-direction (f) Close-up

(g) $d = 0.8 \cdot h$, 7 LEDs (h) Sum, x-direction (i) Close-up

(j) $d = 0.735 \cdot h$, 7 LEDs (k) Sum, x-direction (l) Close-up

Figure A.3: 2D- Modelling in the x-direction of 7 μLEDs irradiating a flat surface at $h = 200\mu m$ above the LED's surface. Total irradiance is measured at varying distances d between the individual LEDs. A close-up of the irradiance at the surface is given in the most right images.

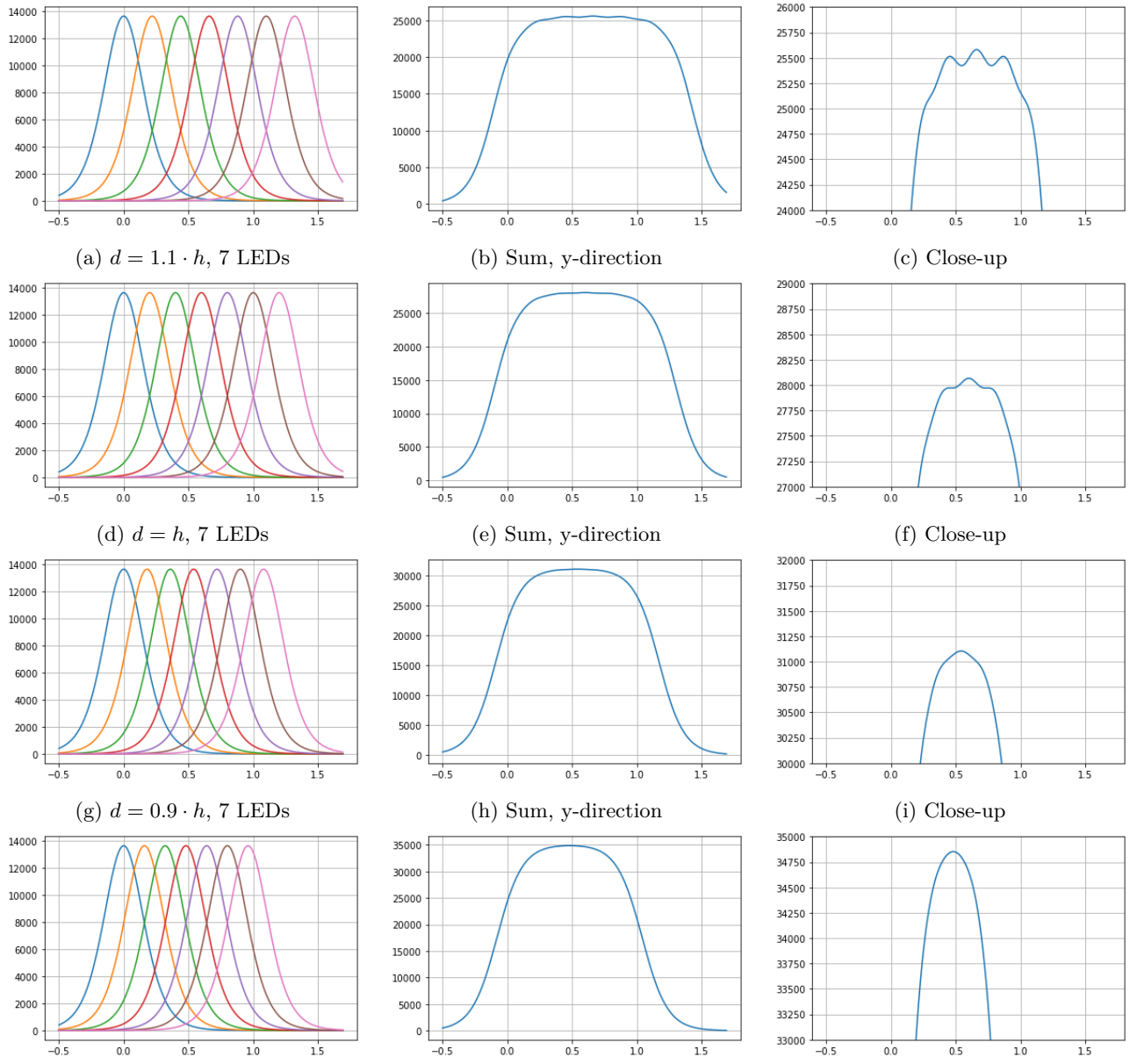

(a) $d = 1.1 \cdot h$, 7 LEDs (b) Sum, y-direction (c) Close-up

(d) $d = h$, 7 LEDs (e) Sum, y-direction (f) Close-up

(g) $d = 0.9 \cdot h$, 7 LEDs (h) Sum, y-direction (i) Close-up

(j) $d = 0.8 \cdot h$, 7 LEDs (k) Sum, y-direction (l) Close-up

Figure A.4: 2D- Modelling in the y-direction of 7 μLEDs irradiating a flat surface at $h = 200\mu m$ above the LED's surface. Total irradiance is measured at varying distances d between the individual LEDs. A close-up of the irradiance at the surface is given in the most right images.

A.1.3 3D modelling μLED sum of irradiation

We start simulating the square formation (A.5):

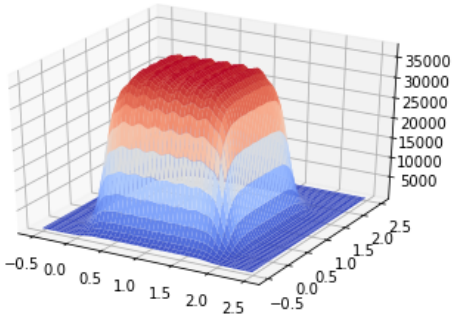

(a) $d = 1.1h$, square

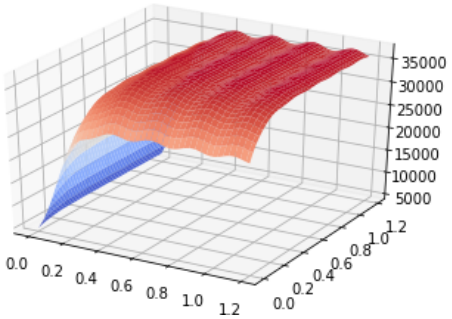

(b) Close-up

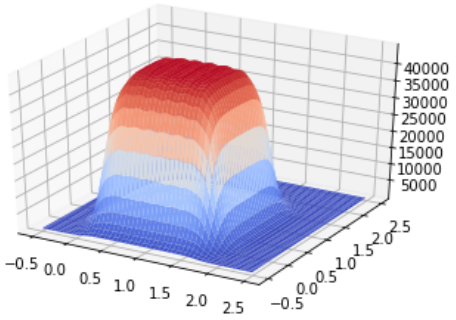

(c) $d = h$, square

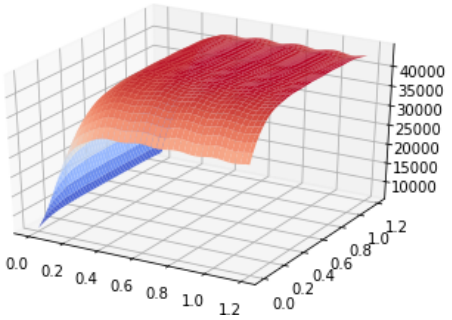

(d) Close-up

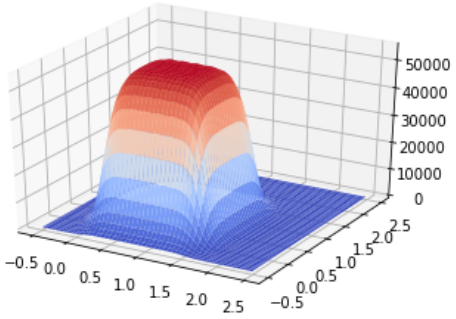

(e) $d = 0.9h$, square

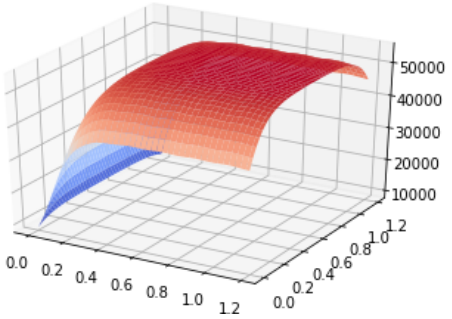

(f) Close-up

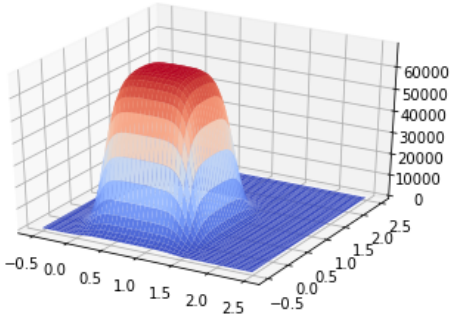

(g) $d = 0.8h$, square

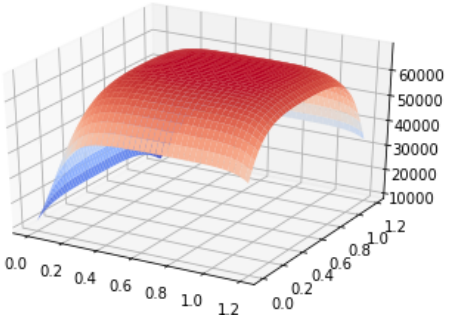

(h) Close-up

Figure A.5: 3D-Modelling of μLEDs 8x8 array in a square formation. Total irradiance pattern is shown for a flat surface $h = 200\mu m$ above the LED surface at varying distances between the LEDs. A close-up of the irradiance at the surface is given on the right images.

Likewise, we simulate the rectangular formation:

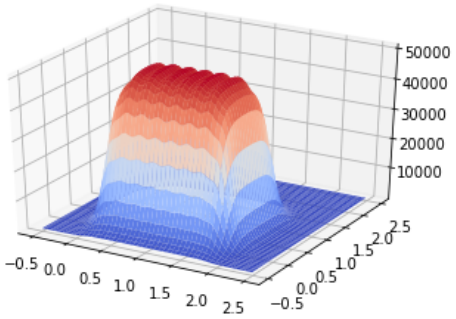

(a) $d = 1.1h$, rectangular

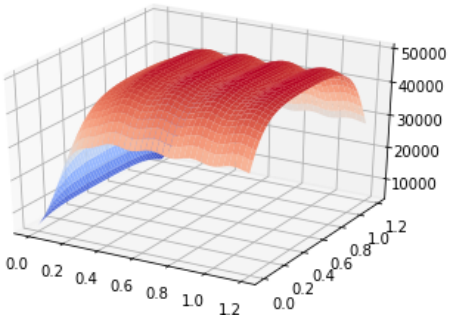

(b) Close-up

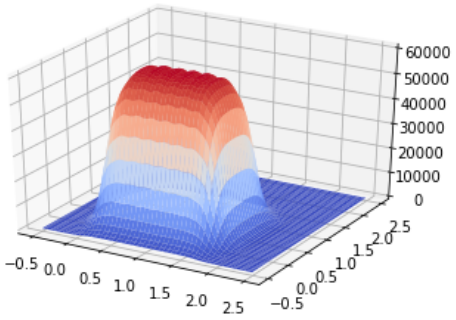

(c) $d = h$, rectangular

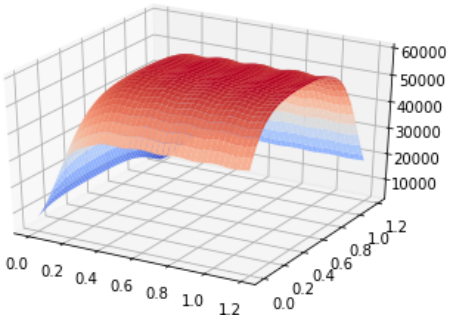

(d) Close-up

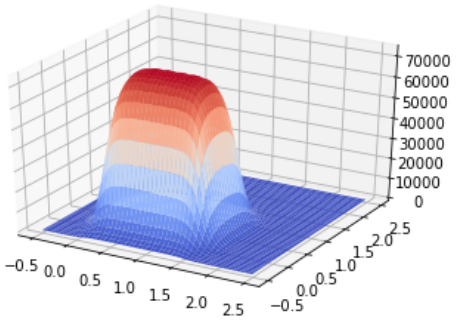

(e) $d = 0.9h$, rectangular

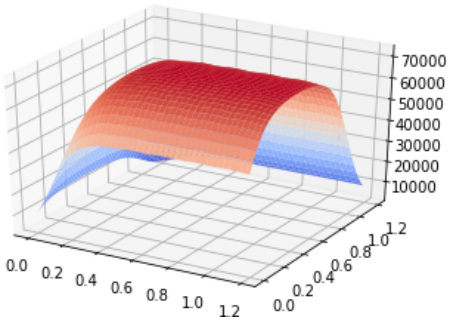

(f) Close-up

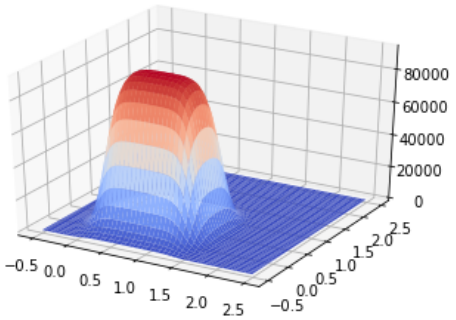

(g) $d = 0.8h$, rectangular

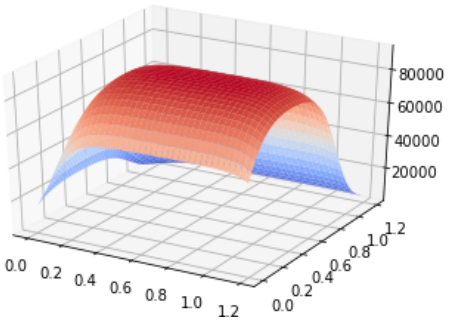

(h) Close-up

Figure A.6: 3D-Modelling of μLEDs 8x8 array in a rectangular formation. Total irradiance pattern is shown for a flat surface $h = 200\mu m$ above the LED surface at varying distances between the LEDs. A close-up of the irradiance at the surface is given on the right images.

Finally, the hexagonal formation was simulated. It can be seen that this pattern produces a more homogeneous irradiance than square and rectangular formations at the same distance d. While a homogeneous irradiance pattern is already observed at $d = h$, more simulations are done with $d > h$. This homogeneous irradiance seems to hold up till $d \approx 1.2h$.

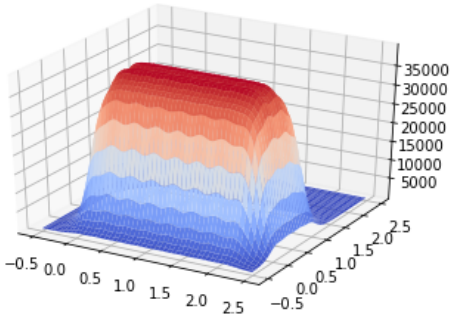

(a) $d = 1.5h$, hexagonal

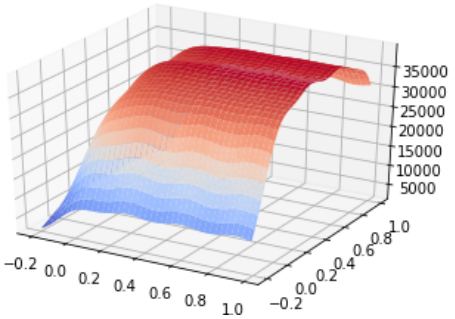

(b) Close-up

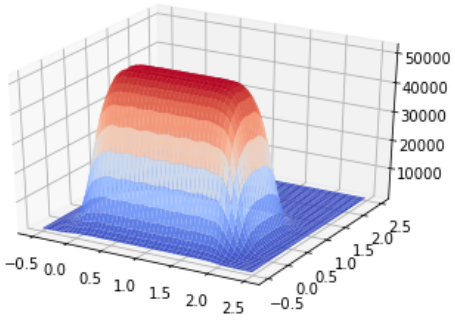

(c) $d = 1.3h$, hexagonal

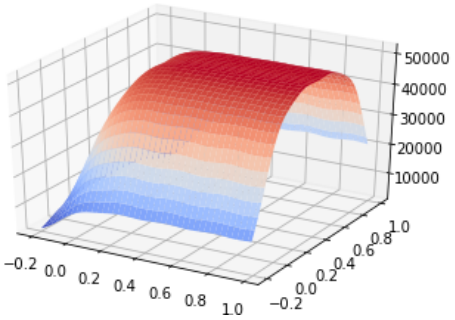

(d) Close-up

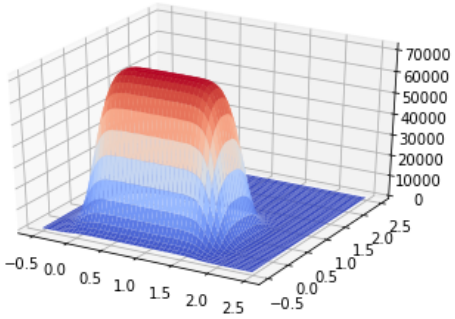

(e) $d = 1.1h$, hexagonal

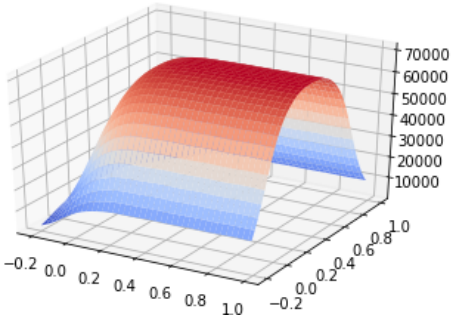

(f) Close-up

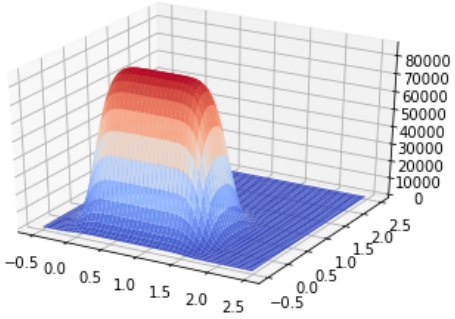

(g) $d = h$, hexagonal

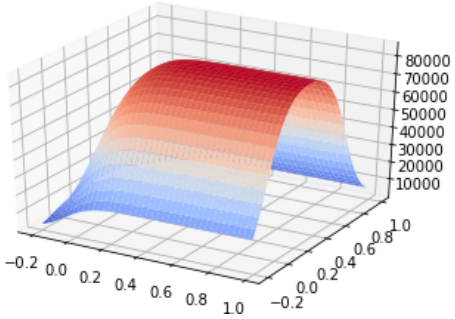

(h) Close-up

Figure A.7: 3D-Modelling of μLEDs 8x8 array in a hexagonal formation,$h = 200\mu m$.

A.1.4 Hexagonal μLED formation: Very nearby irradiance

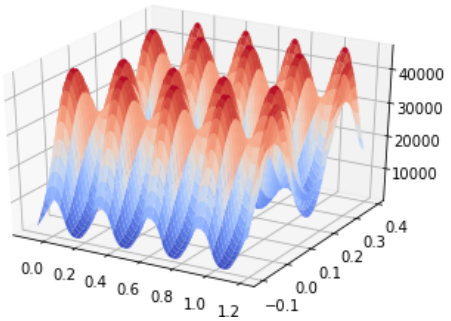

(a) $d = 15h$, hexagonal

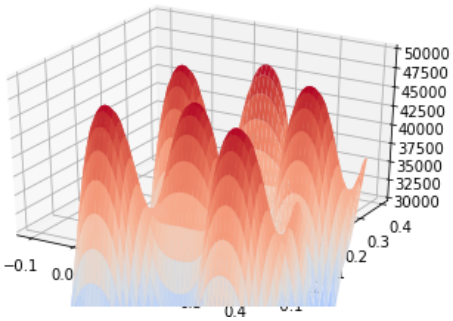

(b) Close-up

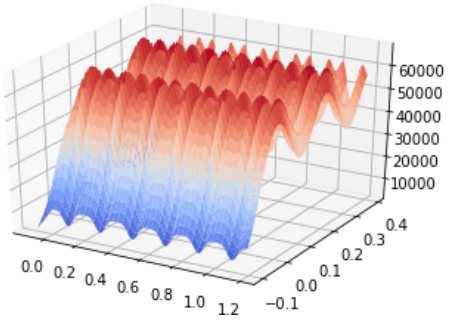

(c) $d = 10h$, hexagonal

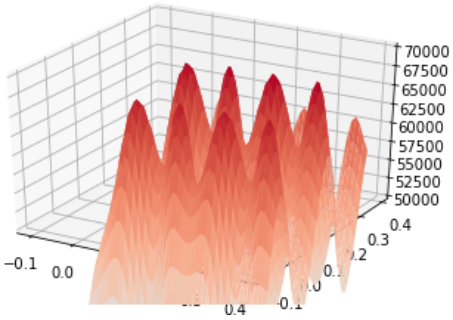

(d) Close-up

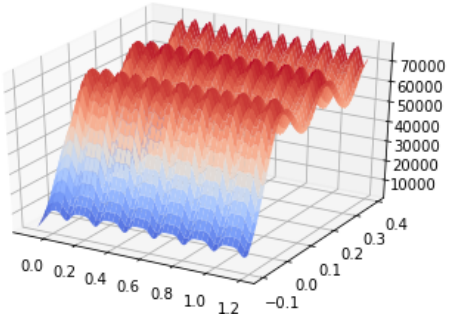

(e) $d = 9h$, hexagonal

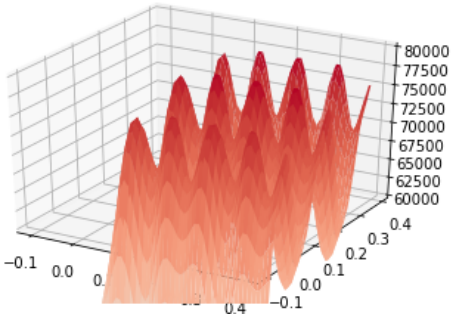

(f) Close-up

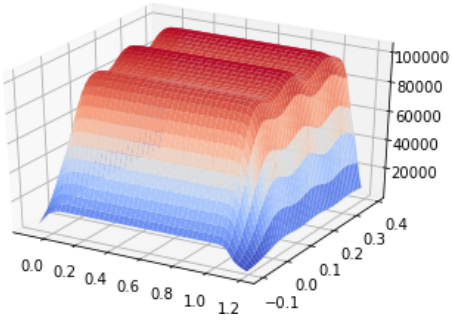

(g) $d = 7.25h$, hexagonal

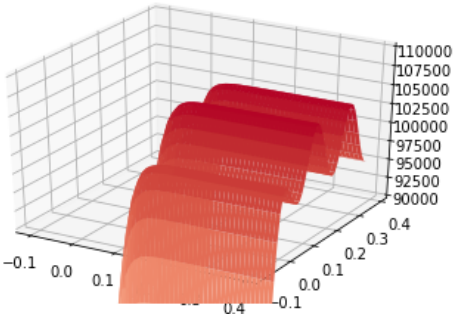

(h) Close-up

Figure A.8: 3D-Modelling of μLEDs 8x8 array in a hexagonal formation,$h = 20\mu m$.

A.2 Arduino code

```
// GOAL: Read out ECG signal, pressure, temperature and humidity
// GOAL 2: Put LED panel on/off at chosen time interval (i.e. 200/800ms) or at ECG triggering, or both
// L.F.A. Wymenga, last update: 18-10-2021

#define RELAY1 2   // Set relay ports
#define RELAY2 3
#define RELAY3 4
#define RELAY4 5

#include "DHT.h"   // Include temp/hum sensor
#define DHTPIN 8
#define DHTTYPE DHT22
DHT dht(DHTPIN, DHTTYPE);

int sensorPin = A4;   // Include pressure sensor
int sensorValue = 0;
float Vout = 0;
float P = 0;
float outputValue = 0;

const int blinkDuration = 200;  // ON time of LED panel (ms)
const int RELAY1_Interval = 800; // OFF time of LED panel (ms)

byte RELAY1_State = LOW; // Set initial relay states to off
byte RELAY2_State = LOW;
byte RELAY3_State = LOW;
byte RELAY4_State = LOW;

unsigned long currentMillis = 0;    // Stores the value of millis() in each iteration of loop()
unsigned long previousRELAY1_Millis = 0;



//========

void setup() {

  Serial.begin(9600);
  dht.begin();

  pinMode(RELAY1, OUTPUT); // Relay ports as output
  pinMode(RELAY2, OUTPUT);
  pinMode(RELAY3, OUTPUT);
  pinMode(RELAY4, OUTPUT);
  pinMode(10, INPUT); // Setup ECG detection LO +
  pinMode(11, INPUT); // Setup LO -

  pinMode(sensorPin, INPUT);  // Pressure sensor is on Analogue pin 4
}

//=======

void loop() {

  // Loop 6 different programs 10 times per second
  currentMillis = millis();  // Count time in ms
  updateRELAY1_State();      // Update relay states
  switchLeds();              // Switch relays on/off
  readTempHum();             // Measure temp/hum
  readECG();                 // Read out ECG signal
  readPres();                // Measure pressure
  delay(100);
}


void readTempHum() {

  float t = dht.readTemperature();
  float h = dht.readHumidity();
  Serial.print("Temperature ");
  Serial.print(t);
  Serial.print(" Humidity ");
```

```
  Serial.print(h);
}


void readECG() {

  Serial.print(" ECG ");
  Serial.print(analogRead(A3));
}

void readPres() {

  sensorValue = analogRead(sensorPin);
  outputValue = map(sensorValue, 0, 1023, -2000, 2000);
  Serial.print("Pressure ");
  Serial.println(outputValue);
}

void updateRELAY1_State() {

  // Choose to trigger LEDs per time interval, ECG signal or both
  if ((RELAY1_State == LOW) ||(analogRead(A3) >600) ) {
    if (currentMillis - previousRELAY1_Millis >= RELAY1_Interval) {
      RELAY1_State = HIGH;
      RELAY2_State = HIGH;
      RELAY3_State = HIGH;
      RELAY4_State = HIGH;
      previousRELAY1_Millis += RELAY1_Interval;
    }
  }
  else {
    if (currentMillis - previousRELAY1_Millis >= blinkDuration) {
      RELAY1_State = LOW;
      RELAY2_State = LOW;
      RELAY3_State = LOW;
      RELAY4_State = LOW;
      previousRELAY1_Millis += blinkDuration;
    }
  }
}

void switchLeds() {
  digitalWrite(RELAY1, RELAY1_State);
  digitalWrite(RELAY2, RELAY2_State);
  digitalWrite(RELAY3, RELAY3_State);
  digitalWrite(RELAY4, RELAY4_State);
}

//=====END
```

Listing A.1: Arduino program *Measure Data.ino*

A.3 Movies

Supplementary movies of the demonstrator in use, DMA testing, IR measurement and ECG recording can be found at: `https://delftao.wixsite.com/lces`.

Thank you

Many thanks go out to: prof. Kouchi Zhang and prof. Willem van Driel for giving me the opportunity and support to work on this topic. Thanks go out to prof. Kaspar Jansen for allowing me to use the DMA machine. I thank Tianji Jin a lot for his major support and practical help with this thesis. Thanks to Zichuan Li and Shanliang Deng, Shriya Rangaswamy for support on specific topics. Hans de Vries and Johan van den Boorn at the Signify company are thanks for their contribution to optical measurements. Also I would like to thank the people helping me with 3D-printing the setup: Reinier van Antwerpen, Jan van Frankenhuyzen, and the people helping with IR measurements (Aravind Babu, Dong Hu). A lot of thanks to the Florence group in providing information, MM10 samples, and support: Cecilia Ferrantini, Camilla Parmeggiani, Simone Donato and the rest. Lastly, I thank my family, friends and girlfriend for bringing joy and supporting me throughout the year.

Luutzen Wymenga, Delft, 22 November 2021